Title

Development of High Performance, Next-Generation Li-ion Battery Electrode Materials: Sulfur, Carbon and Silicon

Author

Campbell, Brennan James

Publication Date

2016

UNIVERSITY OF CALIFORNIA
RIVERSIDE

Development of High Performance, Next-Generation Li-ion Battery Electrode Materials: Sulfur, Carbon and Silicon

A Dissertation submitted in partial satisfaction
of the requirements for the degree of

Doctor of Philosophy

in

Materials Science and Engineering

by

Brennan James Campbell

December 2016

Dissertation Committee:
  Dr. Mihrimah Ozkan, Chairperson
  Dr. Cengiz S. Ozkan
  Dr. Marko Princevac
  Dr. Sandeep Kumar

The Dissertation of Brennan James Campbell is approved:

Committee Chairperson

University of California, Riverside

Acknowledgements

The text of this dissertation (or thesis), in part or in full, is a reprint of the material as it appears in: SiO_2-Coated Sulfur Particles with Mildly Reduced Graphene Oxide as a Cathode Material for Lithium-Sulfur Batteries [Brennan Campbell, Jeffrey Bell, Hamed H. Bay, Zachary Favors, Robert Ionescu, Cengiz S. Ozkan and Mihrimah Ozkan, February 18th, 2015], Bio-Derived, Binderless, Hierarchically Porous Carbon Anodes for Li-ion Batteries [Brennan Campbell, Robert Ionescu, Zachary Favors, Cengiz S. Ozkan and Mihrimah Ozkan, September 29th, 2015], Structural and Compositional Characterization of Fungus-Derived Pyrolytic Carbon Architectures [Brennan Campbell, Robert Ionescu, Cengiz S. Ozkan and Mihrimah Ozkan, June 14th, 2016], and Carbon-Coated, Diatomite-Derived Nanosilicon as a High Rate Capable Li-ion Battery Anode [Brennan Campbell, Robert Ionescu, Maxwell Tolchin, Kazi Ahmed, Zachary Favors, Cengiz S. Ozkan and Mihrimah Ozkan, October 7th, 2016]. The co-authors, Cengiz S. Ozkan and Mihrimah Ozkan, listed in these publications, directed and supervised the research which forms the basis for this dissertation.

The following co-authors contributed to SiO_2-Coated Sulfur Particles with Mildly Reduced Graphene Oxide as a Cathode Material for Lithium-Sulfur Batteries in the following ways: Jeffrey Bell helped carry out synthesis and characterization experiments, Hamed H. Bay assisted with TEM characterization, and both Zachary Favors and Robert Ionescu contributed to data analysis and manuscript development. The following co-authors contributed to Bio-Derived, Binderless, Hierarchically Porous Carbon Anodes for

Li-ion Batteries in the following ways: Robert Ionescu carried out synthesis and characterization and Zachary Favors contributed to data analysis and analytical characterization.

The following co-authors contributed to Structural and Compositional Characterization of Fungus-Derived Pyrolytic Carbon Architectures in the following ways: Robert Ionescu assisted with material characterization and manuscript development.

The following co-authors contributed to Carbon-Coated, Diatomite-Derived Nanosilicon as a High Rate Capable Li-ion Battery Anode in the following ways: Robert Ionescu contributed to materials synthesis and characterization, and assisted in manuscript writing, Maxwell Tolchin carried out material synthesis and data analysis, Kazi Ahmed performed EIS analysis, and Zachary Favors contributed to analysis and manuscript development.

My deepest and most sincere thanks go out to all who made the completion of my Ph.D. possible. I would like to extend my thanks all the way back to my undergraduate research advisor at Cal State Bakersfield, Dr. Danielle Solano, for accepting me into her newly formed research group and inspiring me to pursue research and graduate school. I would also like to acknowledge my Ph.D. co-advisors, Dr. Mihri Ozkan and Dr. Cengiz Ozkan, for accepting me into their group and believing in my abilities as a researcher. They provided an exceptional environment that was conducive to creativity and exploration, and which allowed me to grow intellectually and mature as a researcher. Of course, I am deeply grateful for my committee members, Dr. Sandeep Kumar and Dr. Marko Princevac.

I would like to also thank my peers and lab mates at UC Riverside, who challenged me, inspired me, and were, in general, good company. Precisely, I want to thank Robert Ionescu for his fruitful partnerships in research, Dr. Zachary Favors for his extensive mentorship, and Mathias Rommelfanger for his friendship and microscopy assistance.

My biggest thanks go to my family, my broadest support base. Whether present or away, Lisa Campbell and Robert Campbell, my mother and father, are my two biggest role models. Thank you for encouraging my self-discovery, intellectual pursuits and growth as a good human being since day one. Thank you, Bill Matthes, for bringing more support to the whole family. Thank you, Scotty and Erin Campbell, for reminding me why I want to build another family someday. Thank you, Mama2 and Grandpa, for providing a home away from home. Thank you, Chris Wood and Glenn Wood, for continued guidance and mentorship. Thank you, Abigail Feceu, for coming into my life.

Copyright Acknowledgments

SiO_2-Coated Sulfur Particles with Mildly Reduced Graphene Oxide as a Cathode Material for Lithium-Sulfur Batteries was reproduced, in Chapter 1, by permission of The Royal Society of Chemistry (http://pubs.rsc.org/en/content/articlelanding/2015/nr/c4nr07663j#!divAbstract).

The text and figures in Chapter 2, in part or in full, are a reprint of material as-printed in *Adv. Mater. Sci. Eng.* **2016**, 9843875 with full permission from Hindawi Publishing Corporation. The work was published as open access with a Creative Commons Attribution, which permits its unrestricted use, distribution, and reproduction, and is copyrighted by Brennan Campbell.

The text and figures in Chapter 3, in part or in full, are a reprint of material as-printed in *Scientific Reports* **5**, 14575 with full permission from Nature Publishing Group. The work was published as open access with a Creative Commons Attribution 4.0 International License, which gives the authors copyright over the printed material.

The text and figures in Chapter 4, in part or in full, are a reprint of material as-printed in *Scientific Reports* **6**, 33050 with full permission from Nature Publishing Group. The work was published as open access with a Creative Commons Attribution 4.0 International License, which gives the authors copyright over the printed material.

Dedication

My cumulative dissertation work is dedicated to my mother, Lisa Gayle Campbell.

Nowhere is perseverance better represented than by this woman.

ABSTRACT OF THE DISSERTATION

Development of High Performance, Next-Generation Li-ion Battery Electrode Materials: Sulfur, Carbon and Silicon

by

Brennan James Campbell

Doctor of Philosophy, Graduate Program in Materials Science and Engineering
University of California, Riverside, December 2016
Dr. Mihrimah Ozkan, Chairperson

As of late, there has been an increasing interest in research to characterize and develop a new generation of Li-ion electrode materials that exhibit Li storage performance that goes beyond the incumbent Li-ion chemistries, such as graphite and lithium cobalt oxide, or LCO. LCO, pioneered by Dr. John B. Goodenough in the 1980s, has prevailed as the most common Li-ion cathode for decades, serving as a relatively stable, energy dense intercalation material with a high operating voltage and specific energy of 3.6V (nominal) and 240 Wh/kg, respectively. As well, graphite has served as the most ubiquitous secondary battery anode for an even longer period of time. As a light, cheap and reliable material, the stacks of carbon sheets within graphite have acted as a robust host for lithium, allowing the Li ions to be inserted and removed for hundreds and thousands of cycles at a low voltage. The principle method of preparing these electrode materials has been though

large-scale slurry-casting on to metal foils, calendaring, and winding into various form factors, such as cylindrical or pouch. The slurry is the term used for the suspension of active electrode material (powderized), conductive additive (nano-sized carbon), and a dissolved binder, which acts as an adhesive and/or thickening agent. While LCO and graphite have provided the energy density and power density needed to realized various technologies up until today, there is a need to push the boundaries of rechargeable chemistries in terms of energy density, rate capability (related to power density), and more sensible battery “sandwich” configurations and architectures. Three promising electrode systems for future Li-ion batteries that will improve these characteristics are sulfur cathodes, altered carbon anodes, and silicon-based anodes.

Table of Contents

Chapter 1 SiO2-Coated Sulfur Particles with Mildly Reduced Graphene Oxide as a Cathode Material for Lithium–Sulfur Batteries

Chapter 2 Structural and Compositional Characterization of Fungus-Derived Pyrolytic Carbon Architectures

Chapter 3 Bio-derived, Binderless, Hierarchically Porous Carbon Anodes for Li-ion Batteries

Chapter 4 Carbon-Coated, Diatomite-Derived Nanosilicon as a High Rate Capable Li-ion Battery Anode

Chapter 5 Towards Organosulfur Copolymers for Li-S Cathodes

List of Figures

Introduction

The advent of lithium-ion batteries, and their commercialization since the 1990s, has revolutionized the way humans interact with their technology by supplying a high energy density, ~220 Wh kg^{-1}, compared to previous rechargeable chemistries (~60 Wh kg^{-1} for nickel-metal hydride (Ni-MH))[1]. As high-powered electronics and electric vehicles (EVs) become the new paradigms of technology in society, there is a new commensurate demand in energy density in terms of rechargeable energy storage devices. Going beyond Li-ion technology, it is crucial to develop novel electrode materials that are capable of storing more Li per kg or L. This shift is technically possible, as evidenced by numerous publications reporting on the tremendous Li storage capacity of anode materials such as silicon (Si), tin (Sn), and even pure lithium metal. On the cathode end, materials such as sulfur (S, S_8) have been studied extensively and theoretically have a specific capacity of over 1675 mAh g^{-1} [2], compared to 160-200 mAh g^{-1} supplied by legacy Li-ion cathodes such as LCO NMC or NCA[3].

The typical battery configuration of a lithium-sulfur (Li-S) battery is an elemental sulfur cathode paired with an elemental lithium anode. This configuration theoretically yields a gravimetric energy density of 2600 Wh kg^{-1}, over 10x the practical energy density of Li-ion batteries today[4]. Unfortunately, there are physiochemical challenges preventing Li-S from realizing its full potential, both in terms of energy density and cycle stability. Typical Li-ion batteries can be cycled for hundreds, and even thousands of cycles without significant degradation (>80% maximum capacity). The main problems with Li-S are: the poor transport properties (low electrical and ionic conductivities) of S_8, the practical volumetric expansion (swelling) of S_8 during lithiation (~80%), and dissolution of polysulfides in typical Li-S electrolytes, the product of lithium-added sulfur[5]. As the Li-S cell is cycled, dissolved polysulfide species Li_2S_8, Li_2S_7, Li_2S_6, Li_2S_5, and Li_2S_4 migrate to various surfaces within the cell, including inactive can and separator material, and even the anode material[6]. Of course, this leads to rapid irreversible capacity loss, lower rate capability and cycle capacity degradation.

Next-generation high capacity anodes suffer from similar intrinsic properties; elemental Si, although theoretically having an ultra-high specific capacity (>3600 mAh g^{-1})[7], also has very low electrical conductivity (1.1 eV band gap)[8], and has a more severe swelling problem than S_8; its volumetric expansion from lithiation is on the order of nearly 400% (under typical cycling conditions, ~280%)[9]. In addition to next-generation electrode materials, various form of carbonaceous materials have been researched over the past several years in the interest of improving kinetics and/or specific capacity, improving upon the standard graphite anode. Alterations to the anode carbon include heteroatom doping, functionalization, pore engineering, and experimentation with various carbon precursors[10]. Examples of altered carbons as high-performance anodes include activated carbon, biomass-derived carbons, N-doped carbon (nitrogen-doped, not to be confused with semiconductor “n-doping”), and a range of hard carbons, soft carbon and graphitic materials[11].

In this presented work, 3 separate electrode systems are developed and explored vs. lithium in the half-cell, CR2032 coin cell format. The nanoscaled electrodes exhibit various properties and would, in real-world terms, have different applications. The first is a novel architecture for nano-sized elemental sulfur as a cathode material for Li-ion batteries, to use in what is known as a lithium-sulfur (Li-S) battery. The architecture is comprised of an active material nanoparticle core (sulfur), a thin-layer of silica (SiO_2), and an external coating of mildly-reduced graphene oxide (mrGO). This rational design of a sulfur nanoparticle cathode showed good sulfur utilization compared to a standard sulfur cathode, improved specific capacity and respectable cycle stability (along with improved Coulombic efficiency) over 50 cycles. The second system is a carbon anode derived from fungal tissue- specifically the cap skin of mature *Agaricus bisporus*, or the Portobello mushroom. The Portobello served as an ideal model system to explore the efficacy of a mushroom's various tissues as biological (biomass) precursors to carbon anodes. In this particular work, the mushroom-based anodes were tested as freestanding electrodes vs. lithium to study their properties without the presence of potentially data-confounding slurry additives. Lastly, nanosilicon anode work will be discussed, specifically on a biosilica-derived, mesoporous nanosilicon anode. The nanosilicon anodes were prepared via a relatively green and low-energy demanding process called magnesiothermic reduction (Mg-reduction) of the SiO_2-based frustules of diatomaceous earth (DE). This project is motivated by the ambition of producing high-capacity silicon-based anodes which are stable, but also have high Si loading as well as good rate capability.

<u>References</u>

1. Ikeya, T. et al. Multi-step constant-current charging method for an electric vehicle nickel/metal hydride battery with high-energy efficiency and long cycle life. J. Power Sources **105**, 6-12 (2002).

2. Campbell, B. et al. SiO_2-coated sulfur particles with mildly reduced graphene oxide as a cathode material for lithium-sulfur batteries. Nanoscale **7**, 7051–7055 (2015).

3. Chikkannanavar, S. B., Bernardi, D. M. and Liu, L. A review of blended cathode materials for use in Li-ion batteries. J. Power Sources **248**, 91-100 (2014).

4. Wang, J., He, Y. and Yang, J. Sulfur-Based Composite Cathode Materials for High-Energy Rechargeable Lithium Batteries. Adv. Mater. **27**, 569-575 (2015).

5. Yang, Y, Zheng, G. and Cui, Y. Nanostructured sulfur cathodes. Chem. Soc. Rev. **42**, 3018-3032 (2013).

6. Bauer, I. et al. Reduced polysulfide shuttle in lithium-sulfur batteries using Nafion-based separators. J. Power Sources **251**, 417-422 (2014).

7. Campbell, B. et al. Carbon-Coated, Diatomite-Derived Nanosilicon as a High Rate Capable Li-ion Battery Anode. Sci. Rep. **6**, 33050 (2016).

8. Holmes, J. D., Johnston, K. P, Doty, R. C. and Korgel, B. A. Control of Thickness and Orientation of Solution-Grown Silicon Nanowires. Science **287**, 1471-1473 (2000).

9. Zhao, Y. et al. Hierarchical micro/nano porous silicon Li-ion battery anodes. Chem. Commun. **48**, 5079-5081 (2012).

10. Roberts, A. D., Li, X and Zhang, H. Porous carbon spheres and monoliths: morphology control, pore size tuning and their applications as Li-ion battery anode materials. Chem. Soc. Rev. **43**, 4341-4356 (2014).

11. Wu, Z. et al. Doped Graphene Sheets As Anode Materials with Superhigh Rate and Large Capacity for Lithium Ion Batteries. ACS Nano **5**, 5463-5471 (2011).

Chapter 1

SiO2-Coated Sulfur Particles with Mildly Reduced Graphene Oxide as a Cathode Material for Lithium–Sulfur Batteries

1.1 Introduction

For the first time, SiO_2-coated sulfur particles (SCSPs) were fabricated via a facile two-step wet chemical process for application as a novel lithium–sulfur cathode material. With the addition of mildly reduced graphene oxide (mrGO), SCSPs demonstrate even greater cycling stability, maintaining over 700 mAh g^{-1} after the 50th cycle.

The invention of rechargeable lithium-ion (Li-ion) battery technology has set the newest paradigm in energy storage over the last several decades. These batteries are becoming well-developed, and have been responsible for powering portable phones, computers, and electric vehicles.[1] While Li-ion battery cathodes presently have a capacity range of ∼150–200 mAh g^{-1} , the theoretical capacity of lithium–sulfur (Li–S) cathodes is 1675 mAh g^{-1}, and recent research shows that hundreds of cycles at specific capacities of over 700 mAh g^{-1} is possible.[2,3] Li–S batteries show great promise in meeting the critical need for EV batteries with high specific capacity, both volumetric and gravimetric. The Li–S system offers other advantages as well; the elements lithium and sulfur offer a

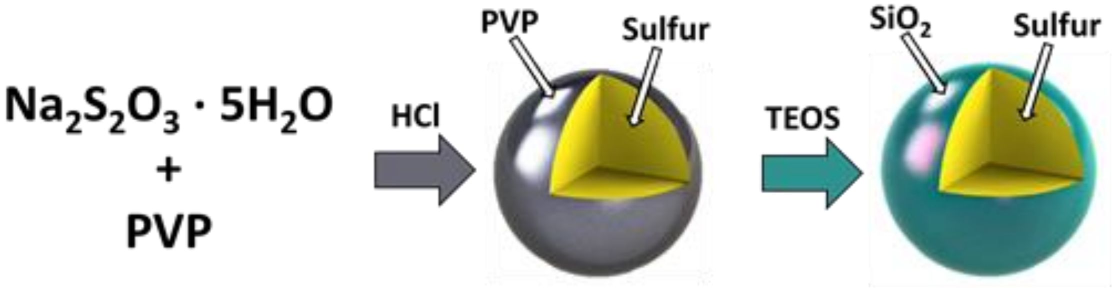

Figure 1.1: A schematic illustration of the two-step wet chemical synthesis of SCSPs, showing the starting materials sodium thiosulfate pentahydrate and PVP (a), the formation of PVPCSPs after HCl addition (b) and finally the SCSPs after addition of TEOS solution (c).

relatively low-cost battery due to their light weight and relatively high abundance.[4,5]

The number of new Li–S battery publications in recent years is growing exponentially, showing the increased interest in addressing the problems with Li–S batteries. However, challenges with the Li–S battery include the low electronic conductivity of sulfur (5×10^{-30} S cm^{-1} at 25 °C), poor ionic diffusivity, volumetric expansion during lithiation (~80%), and the polysulfide "shuttle" effect, in which the intermediate lithium polysulfides (Li_2S_n, $4 \leq n \leq 8$) dissolve into the electrolyte.[6–8] Recently, other materials have been introduced into sulfur cathodes, many of which have properties that enhance cathode performance in ways that carbon cannot. For instance, TiO_2 and several other oxide nanostructures have been demonstrated as beneficial additions to sulfur cathodes, due to their inertness to redox reactions and extraordinary polysulfide adsorbing properties.[9,10] In many cases SiO_2 is termed a "polysulfide reservoir," as in the work done by Ji et al., wherein SBA-15 mesoporous silica was used as an additive in a mesoporous carbon/sulfur composite for a lithium–sulfur cathode structure. In this work it was demonstrated that the small amount of SiO_2 additive was necessary for trapping polysulfides and then readily desorbing them during electrochemical reduction/oxidation.[11] In addition, the increased stability shown in the cycling of this cathode composite was attributed to the mesoporous structure of the SiO_2, inhibiting diffusion of the polysulfide anions. Besides SiO_2, other oxides have been shown to stabilize soluble polysulfide species, including Al_2O_3 and La_2O_3, often incorporated into nanocomposites with graphene or graphene oxide (GO).[23,24] The battery performance of a sulfur-silica core–shell structure has, until now, yet to be explored.

1.2 Experimental Methods and Materials

Herein, we report the facile wet synthesis of SiO_2-coated sulfur particles (SCSPs), and assess this novel material as a possible Li–S battery cathode. The general synthesis of SCSPs is outlined in Fig. 1.1, and the synthesis was performed as follows: A 100 mL aqueous solution of $Na_2S_2O_3 \cdot 5H_2O$ (1 g) and polyvinylpyrrolidone (PVP) (20 mg, 55,000 MW), an amphiphilic surfactant polymer, was prepared. While mildly stirring the solution, 0.80 mL concentrated HCl was added dropwise. The reaction requires two hours for completion, although a white cloudy precipitate can be observed almost instantly. During this time, thiosulfate ions decompose into elemental sulfur (S_8), which forms particles that are coated with PVP. After two hours, the contents of the reaction vessel were centrifuged for 10 minutes at 3.6 krpm, and resuspended in a 0.05 wt.% solution of PVP.[12] The suspension was again centrifuged for 10 minutes at 3.6 krpm, and this wash/centrifuge process was done two more times using deionized water (DI H_2O). The washed PVP-coated sulfur particles (PVPCSPs) were suspended in 20 mL DI H_2O and set aside. Next, a modified Stöber process was used to coat the sulfur particles with silica (SiO_2).[13–15] In this process, a solution of tetraethyl orthosilicate (TEOS) was first prepared by adding 20 μL TEOS to 20 mL methanol (MeOH). In a flask, 80 mL MeOH and 2 mL 30% ammonia (NH_3) were combined and stirred vigorously. While stirring, the 20 mL PVPCSP suspension was transferred dropwise to the NH_3 solution. The TEOS solution was then added to the reaction vessel dropwise, adding 5 mL every 30 minutes until there was no remaining TEOS solution. The reaction was stirred for 17 hours, then centrifuged and washed several times with DI H_2O and isopropyl alcohol (IPA). The reaction was optimized to these conditions by varying ageing time for the Stöber process (12–24 hours), and the amount of TEOS added (10–30 μL).

For addition of mildly reduced graphene oxide (mrGO), Hummer's method was first used to prepare graphene-oxide (GO).[16] Next, 20 mg SCSPs were suspended in 10 mL ethanol (EtOH), and was kept stirring. A separate suspension of 6 mg GO in 3 mL DI H_2O was also prepared, and then slowly added to the SCSP suspension while stirring. The reaction vessel was then placed in an ice bath, and 16 μL hydrazine was added for the partial reduction. This reaction was allowed to stir at 0 °C for 24 hours, after which the product was washed repeatedly with DI H_2O and dried under vacuum for 24 hours at 60 °C.

1.3 Electron Microscopy and X-ray Analysis

Morphologies of the PVPCSPs and SCSPs were studied using scanning electron microscopy (SEM), and are seen in Fig. 1.2a and 1.2b, respectively. In Fig. 1.2a, PVPCSPs are shown to have a spherical shape, with a diameter of about 700–800 nm. Some smaller particles also tend to form during the synthesis is most likely due to small changes in reaction conditions. Under the SEM beam, the PVP coatings distort, revealing their core–shell type structure. Fig. 1.2b exhibits the SCSPs on an aluminum substrate. The diameter of the SCSPs are generally greater than the PVPCSPs, while the SiO_2 coatings appear bumpy and somewhat uneven at the surface. This uneven surface is possibly attributed to a degree of compositional inhomogeneity in the deposited silica coatings.[17] As a consequence, many SCSPs tend to assume a potato-like morphology rather than a perfect spherical morphology, although most tend to remain relatively spherical. Besides the bumps on the surface, we see from TEM analysis in Fig. 1.2 that the SiO_2 renders as a thin film on the surface of the sulfur particles. Fig. 1.2c captures a smaller potato-shaped SCSP, differentiating the sulfur core from the SiO2 shell. The particle is resting on top of a SiO2 nanotube, which tend to form when there is excess PVP that carries over from the PVPCSP synthesis. TEM of the silica shell is shown in Fig. 1.2d, allowing a view of the continuous coating without sulfur.

This image is the results of the electron beam causing the sulfur to react and escape the structure, giving valuable information about the shell alone. HRTEM on the silica shell (Fig. 1.2e) confirms that the silica is amorphous. On average, the thickness of the SiO_2 shell is about 20 nm, although the thickness increases near the bumps. The amorphous nature of the SiO_2 coating was also confirmed with HRTEM in Fig. 1.2e. Evidently, there is a relatively high degree of control over the size and morphology of the novel SCSP material, making it an ideal system to electrochemically characterize as a Li–S cathode material. Furthermore, point ID energy dispersive X-ray spectroscopy (EDS) confirmed the presence of both elemental sulfur and silica in SCSPs, while the prevailing presence of sulfur with respect to silica in the SC

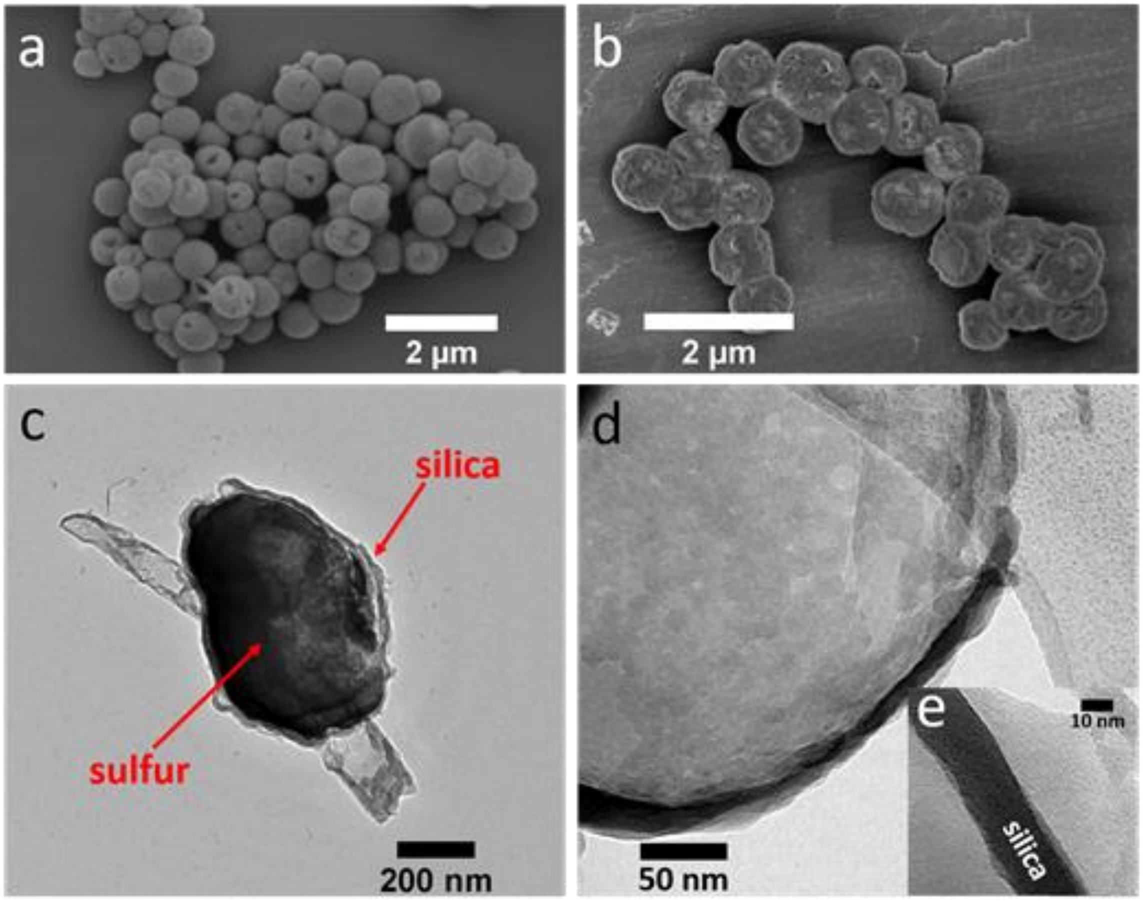

Figure 1.2: SEM images of PVP-coated sulfur particles (a), SCSPs (b), and TEM images of an isolated SCSP, still containing sulfur (c), the remaining silica shell after sulfur escape (d), and HRTEM of the silica shell showing its amorphous nature (e).

SP cathode is evidenced by the XRD spectrum of SCSPs in comparison to amorphous SiO_2 and sulfur, seen in Fig. 1.3a. The Al peak in EDS results from the aluminum substrate used to prevent skewing of the presence of Si. The amorphous thin-layer SiO_2 shell surrounding the sulfur cores inhibits the polysulfide shuttle effect, acting as an adsorbent barrier and polysulfide reservoir. The polysulfide shuttle effect tends to hinder typical carbon–sulfur cathode structures and they may experience active material loss. SiO_2 has the inherent ability to surface-adsorb polysulfide species that are soluble in the electrolyte, which deters the loss of electrochemically active sulfur over numerous cycles.[11] In this design, the SiO_2 shell carries out this task, while allowing Li^+ diffusion. During battery fabrication we have found that, rather than solely including carbon black (CB) as a conductive additive, the addition of mildly reduced graphene oxide (mrGO) significantly improves the cyclability of the cathode, boosting its discharge capacity by over 300 mAh g^{-1} after 50 cycles. mrGO was chosen as a necessary ingredient for the cathode composite due to its ability to wrap its sheets around particles and form a more interconnected conductive network. Thus, it is an equally essential part of the design of this cathode, due to its SiO_2-harnessing action. CB alone would not have provided this conductive sink, which poses a problem for this cathode material composed of one insulator (sulfur) coated with another insulator (SiO_2). As the structure becomes damaged over time, the mrGO acts as a conductive net, contains the structures, and also has polysulfide-trapping properties. Thus, there are several modes of action by which the addition of mrGO helps to improve the cycle stability of SCSPs.

1.4 Electrochemical Characterization and Cell Fabrication

The sulfur content of as-synthesized SCSPs was about 90 wt.% based on EDS data from several syntheses (Fig. 1.3b). For all cyclability plots, the first cycle was run at a C/50 rate, based on the theoretical capacity of 1675 mAh g^{-1}, while each subsequent cycle was run at a C/10 rate. This slow current cycling was necessary due to the highly insulating nature of the SCSP structure. Cyclic voltammetry (CV) curves were obtained using a scan rate of 0.1 mV s^{-1}. After 50 cycles, the SCSPs maintain a respectable specific discharge capacity of 444.4 mAh g^{-1} (Fig. 1.4a), which is still significantly higher than that of materials used in industry today. The conversion $S_8 \rightarrow Li_2S$ is repeatedly allowed to proceed reversibly for several cycles, indicated by the Coulombic efficiency stabilizing at ~99%. However, the capacity decay over the first 50 cycles is still substantial, with an average specific capacity loss of 12.2 mAh g^{-1} per cycle from cycle 2 to 50. The CV curve for SCSPs, shown in Fig. 1.5a, highlights typical lithiation and delithiation peaks for Li–S cathodes, where as expected, lithiation decreases slightly and then stabilizes after cycle 2. This is owed to the ultra-low current density for cycle 1 and the thin SiO_2 coating, which are both thought to encourage the formation of a stable SEI layer.[18,19] As evidenced from the cycling data for SCSPs, capacity fading was still fairly significant for the SCSP cathode, and is most likely due to the encapsulation of an extremely electronically insulating material (S_8) with another insulating material (SiO_2, band gap ~9 eV).[20] The capacity loss experienced with SCSPs alone was the impetus for the addition of mrGO to the cathode mixture, and study thereof. According to Fig. 1.4b, the capacity decay

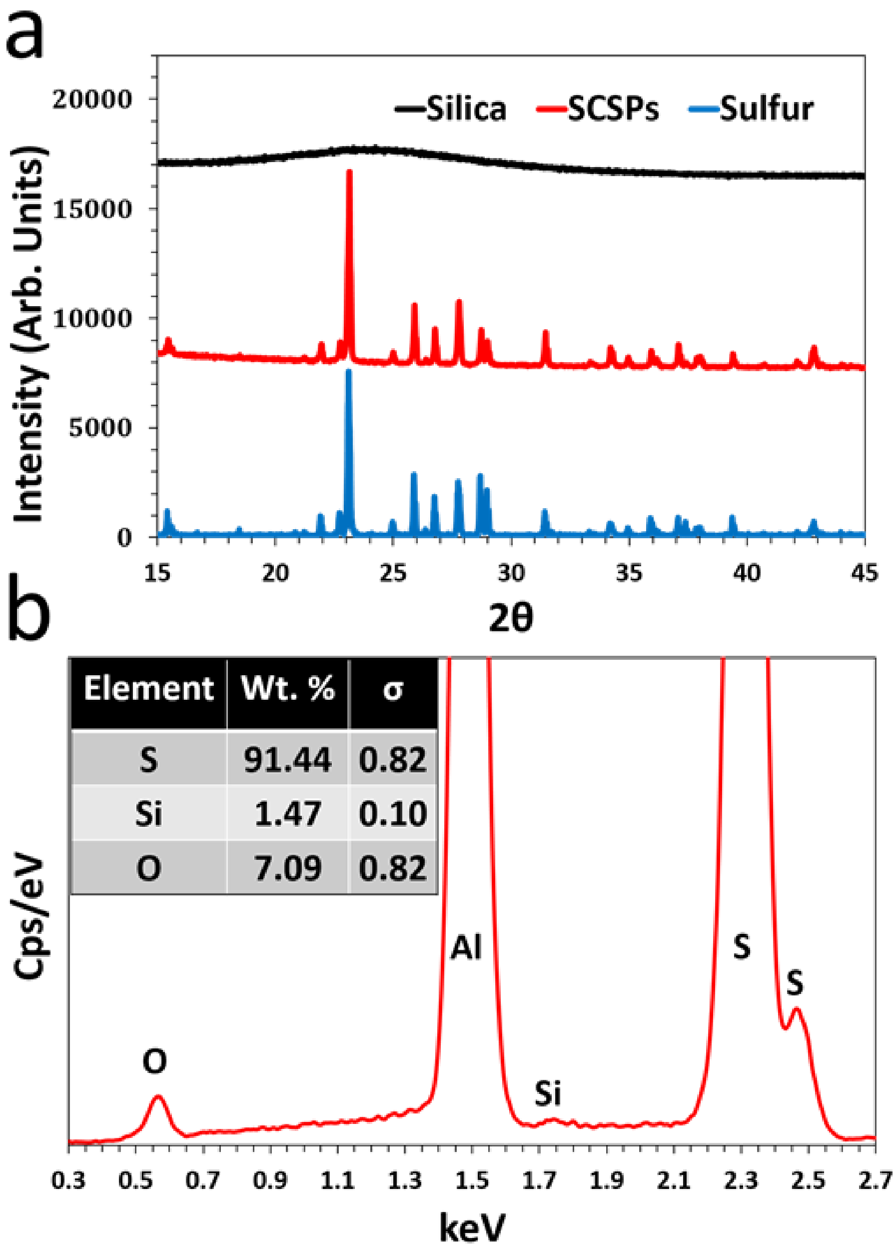

Element	Wt. %	σ
S	91.44	0.82
Si	1.47	0.10
O	7.09	0.82

Figure 1.3: Spectral data including XRD of amorphous silica, SCSPs, and elemental sulfur (a) and EDS of SCSPs, including corresponding relative weight percentages (b).

of SCSPs is markedly improved with the addition of mrGO. From cycles 2 through 50, an average capacity loss per cycle was only 8.6 mAh g^{-1} was experienced, with an improved

Coulombic efficiency of ~99.3%. The CV curve also shows excellent stability of the mrGO-enhanced cathode, exhibiting a more diverse range of redox peaks compared to that of SCSPs alone (Fig. 1.5b). While the lithiation and delithiation peaks stabilize after the first few cycles, there is also a slight up-field shift in their redox potentials after cycle 1; this shift and subsequent stabilization is likely due to the entrapment of SiO_2 and polysulfides between mrGO sheets. With mrGO as an additive, the 50th discharge of SCSPs showed a specific capacity of 763.2 mAh g^{-1}. Thus, as depicted in the comparison in discharge capacities in Fig. 1.4c, a result of mrGO and CB as combined conductive additives rather than CB alone was a 318.8 mAh g^{-1} boost, an enormous benefit. It is hypothesized that these benefits come from the partial wrapping of the SCSP particles, which allows for intimate contact of conductive medium, rather than small CB particles being randomly dispersed throughout the mixture. An added benefit is the polysulfide shuttle-inhibiting properties of the mrGO; this becomes crucial as the SCSP structure breaks down over a number of cycles.

Notably, sulfur is demonstrating its 3 major voltage plateaus in the charge–discharge plots; the 1st and smallest plateau is derived from the solid Li_2S_8 species (2.4–2.3 V), the 2nd and sharpest plateau from the conversion of Li_2S_8 to the soluble Li_2S_6 species (2.3–2.1 V), and finally the longest plateau from the soluble species $Li_2S_{6\geq x>2}$ (2.1–2.0 V).[21,22] The discharge/charge voltage profiles of SCSPs and SCSPs with mrGO were obtained for analyzing the voltage plateau regions. The plateaus of the 1st cycle of SCSP cathode are in good agreement with the charge and discharge peak of its respective CV

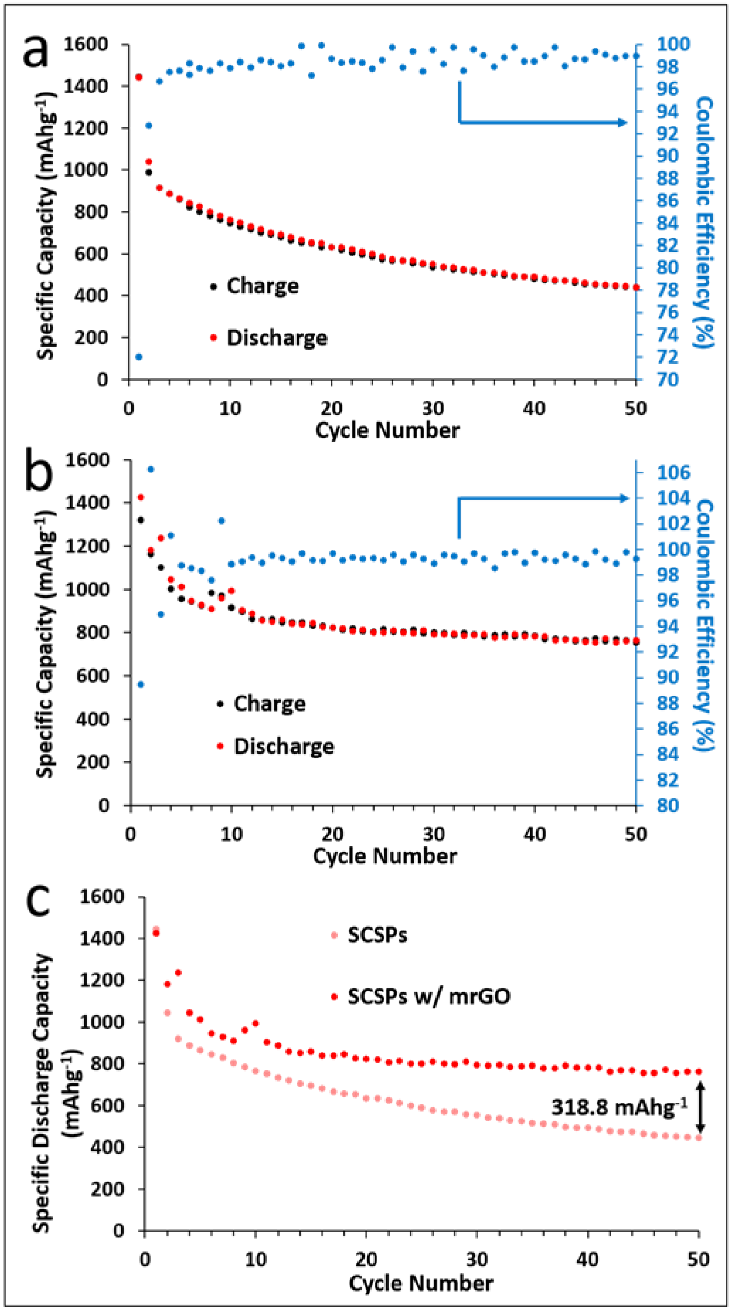

Figure 1.4: Cyclability plots for SCSPs (a) and for SCSPs with mrGO as an additive (b), and the discharge cycle capacity comparison of SCSPs with and without mrGO to 50 cycles (c).

curve (shown in Fig. 1.5c), with the primary operating region between 2.3 and 2.4 V for charging and 2.0 and 2.3 V for discharging. The later charges, however, begin experiencing a broader voltage window. For example, the 5th, 25th and 50th charges operate between 2.2 and 2.4 V, while the discharges remain in the same operating window. As illustrated in Fig. 1.5d, when mrGO is added, an extended voltage plateau is gained for later cycles, with the discharge/charge capacity stabilizing at about 700 mAh g^{-1} for the 50th cycle, in contrast to about 400 mAh g^{-1} for SCSPs alone. The voltage plateaus for the mrGO-enhanced SCSPs also agree with its respective CV curve, and there is also a greater curvature to the plateaus, lending additional capacity to higher voltages. An auxiliary effect of the mrGO additive is the absence of operational voltage reduction, as is seen in the solely SCSP cathode. The assembly of the SCSP-based coin cell batteries involved mixing a 6:3:1 weight ratio of SCSPs, CB, and polyvinylidene fluoride (PVdF) using a mortar and pestle. A slurry was made with N-methyl-2-pyrrolidone (NMP), which was cast onto high purity aluminum foil current collectors and placed in a vacuum oven at 60 °C overnight to dry. CR2032-type coin cells were then fabricated with the SCSPs/CB/PVdF composite as the working electrode, microporous polypropylene as the separator (Celgard 2300), and lithium metal foil as the counter electrode. The electrolyte used was 1 M lithium bis(trifluoromethanesulfonyl)imide (LiTFSI) in a 1:1 vol. ratio of 1,3- dioxolane (DOL) and 1,2-dimethoxyethane (DME), and lithium nitrate ($LiNO_3$) as a lithium-passivating additive at a concentration of 0.5 wt.%. Cells were prepared in an Ar-filled VAC Omni-lab

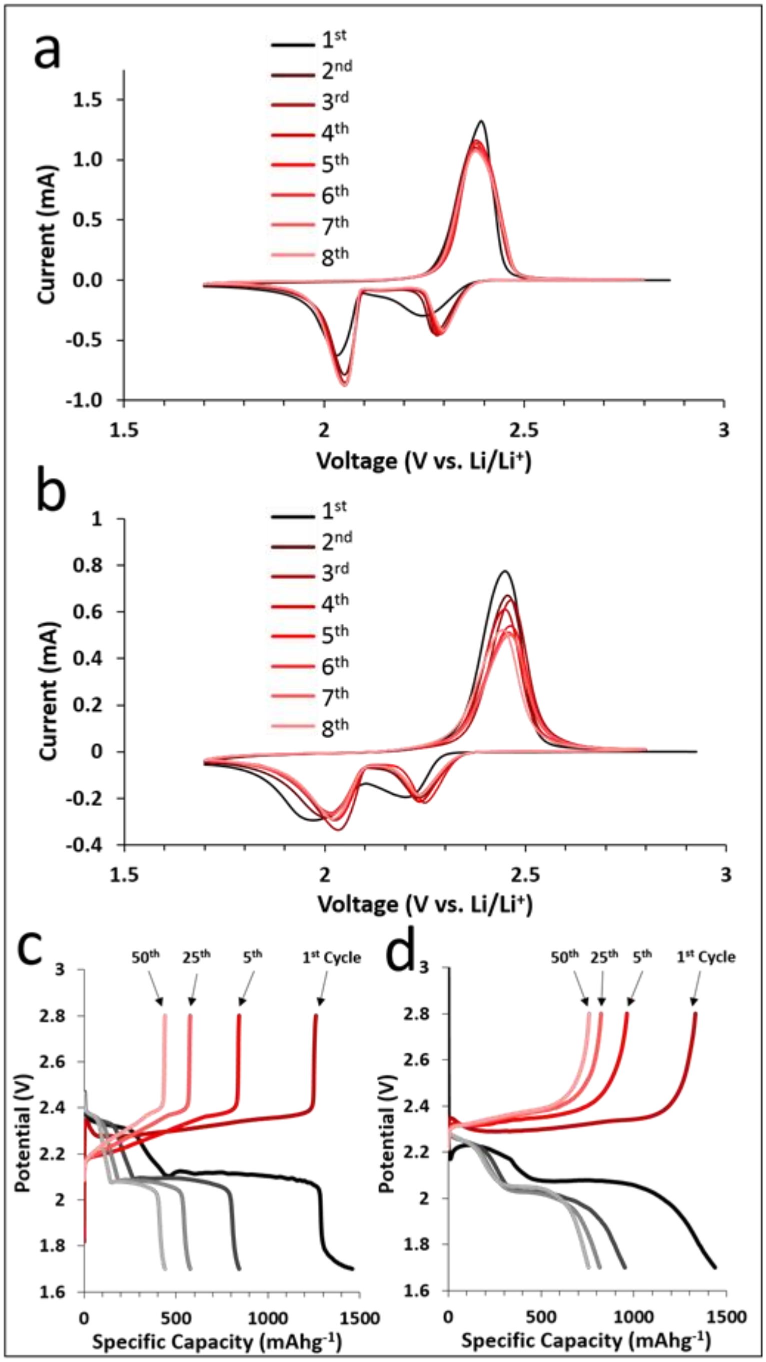

Figure 1.5: Cyclic voltammetry for SCSPs (a) and for SCSPs with mrGO as an additive (b), and voltage profiles of SCSPs (c) and SCSPs with mrGO (d).

glovebox, and were tested vs. lithium from 1.7 to 2.8 V on an Arbin BT2000. CV data was collected using a Biologic VMP3 with a scan rate of 0.1 mV s^{-1}. Scanning electron microscopy characterization was performed using an FEI Nova Nano450SEM, an FEI XL30 SEM, and transmission electron microscopy was carried out using a Philips CM300 TEM.

1.5 Conclusion

In this study, silica-coated sulfur particles (SCSPs) were synthesized and characterized as a cathode material for Li–S batteries. This novel core–shell structure was fabricated in a facile 2-step wet chemical synthesis. The SCSP cathode showed superior cycling stability when coupled with mrGO as an additive, improving the capacity retention after 50 cycles from 440.8 mAh g^{-1} without mrGO to 763.2 mAh g^{-1} with mrGO. The electrochemical data also shows reduced capacity fading over 50 cycles, from 12.2 mAh g^{-1} per cycle without mrGO to 8.6 mAh g^{-1} per cycle with mrGO. During cycling, SCSPs are understood to fracture and release active material (S_8), and mrGO helps to contain the ruptured particles, thereby improving cycling stability. By the 50th cycle, SCSPs experienced a 318.8 mAh g^{-1} boost in specific discharge capacity with the addition of mrGO. These improvements are attributed to the polysulfide inhibiting effects of SiO_2 as well as the host of benefits provided by mrGO, similar to other work.[23,24] Thus, SCSPs with the addition of mrGO show great promise in the application of low-cost, high energy density battery systems for portable electronics and EVs. Further investigation is needed on the SCSP cathode system, expressly into the silica shell pulverization during cycling.

The authors thank Winston Global Energy Center for partially supporting this work, Krassimir Bozhilov and Mathias Rommelfanger in the Central Facility for Advanced Microscopy and Microanalysis (CFAMM) at UC Riverside, for their guidance with TEM. They also acknowledge Lauro Zavala for artistic contributions.

References

1. Y. Su and A. Manthiram. A new approach to improve cycle performance of rechargeable lithium-sulfur batteries by inserting a free-standing MWCNT interlayer. Chem. Commun., **48**, 8817–8819 (2012).

2. G. Ma, Z. Wen, J. Jin, Y. Lu, X. Wu, M. Wu and C. Chen. Hollow polyaniline sphere@sulfur composites for prolonged cycling stability of lithium–sulfur batteries. J. Mater. Chem., **2**, 10350–10354 (2014).

3. J. Wang, L. Yin, H. Jia, H. Yu, Y. He, J. Yang and C. W. Monroe. Hierarchical Sulfur-Based Cathode Materials with Long Cycle Life for Rechargeable Lithium Batteries. ChemSusChem, **7**, 563–569, 2014.

4. C. Liang, N. Dudney and J. Howe. Hierarchically Structured Sulfur/Carbon Nanocomposite Material for High-Energy Lithium Battery. Chem. Mater., **21**, 4724–4730 (2009).

5. B. Zhang, X. Qin, G. R. Li and X. P. Gao. Enhancement of long stability of sulfur cathode by encapsulating sulfur into micropores of carbon spheres. Energy Environ. Sci., **3**, 1531–1537 (2010).

6. Y. Yang, G. Zheng and Y. Cui. Nanostructured sulfur cathodes. Chem. Soc. Rev., **42**, 3018–3032 (2013).

7. A. Fedorkova, R. Orinakova, O. Cech and M. Sedlarikova. New composite cathode materials for Li/S batteries: A review. Int. J. Electrochem. Sci., **8**, 10308–10319 (2013).

8. W. Li, Q. Zhang, G. Zheng, Z. Seh, H. Yao and Y. Cui. Understanding the role of different conductive polymers in improving the nanostructured sulfur cathode performance. Nano Lett., **13**, 5534–5540 (2013).

9. Q. Li, Z. Zhang, K. Zhang, L. Xu, J. Fang, Y. Lai and J. Li. Synthesis and electrochemical performance of TiO2–sulfur composite cathode materials for lithium–sulfur batteries. J. Solid State Electrochem., **17**, 2959–2965 (2013).

10. B. Ding, L. Shen, G. Xu, P. Nie and X. Zhang. Encapsulating sulfur into mesoporous TiO 2 host as a high performance cathode for lithium–sulfur battery Electrochim. Acta, **107**, 78–84 (2013).

11. X. Ji, S. Evers, R. Black and L. Nazar. Stabilizing lithium–sulphur cathodes using polysulphide reservoirs Nat. Commun., **2**, 1–7 (2011).

12. H. Wang, Y. Yang, Y. Liang, J. T. Robinson, Y. Li, A. Jackson, Y. Cui and H. Dai. Graphene-wrapped sulfur particles as a rechargeable lithium–sulfur battery cathode material with high capacity and cycling stability. Nano Lett., **11**, 2644–2647 (2011).

13. W. Rho, H. Kim, S. Kyeong, Y. Kang, D. Kim, H. Kang, C. Jeong, D. Kim, Y. Lee and B. Jun. Facile synthesis of monodispersed silica-coated magnetic nanoparticles Ind. Eng. Chem., **20**, 2646–2649 (2014).

14. C. Graf, D. L. J. Vossen, A. Imhof and A. van Blaaderen. A general method to coat colloidal particles with silica Langmuir, **19**, 6693–6700 (2003).

15. N. R. Jana, C. Earhart and J. Y. Ying. Synthesis of water-soluble and functionalized nanoparticles by silica coating. Chem. Mater., **19**, 5074–5082 (2007).

16. S. Stankovich, D. A. Dikin, R. D. Piner, K. A. Kohlhaas, A. Kleinhammes, Y. Jia, Y. Wu, S. T. Nguyen and R. S. Ruoff. Synthesis of graphene-based nanosheets via chemical reduction of exfoliated graphite oxide. Carbon, **7**, 1558–1565 (2007).

17. Y. J. Wong, L. Zhu, W. S. Teo, Y. W. Tan, Y. Yang, C. Wang and H. Chen, J. Revisiting the stober method: inhomogeneity in silica shells. Am. Chem. Soc., **133**, 11422–11425 (2011).

18. J. Shim and K. A. Striebel. Cycling performance of low-cost lithium ion batteries with natural graphite and $LiFePO_4$. J. Power Sources, **119–121**, 955–958 (2003).

19. L. Su, Z. Zhou and M. Ren. Core double-shell Si@ SiO 2@ C nanocomposites as anode materials for Li-ion batteries. Chem. Commun., **46**, 2590–2592 (2010).

20. D. Waroquiers, A. Lherbier, A. Miglio, M. Stankovski, S. Ponce, M. J. T. Oliveira, M. Giantomassi, G. Rignanese and X. Gonze. Band widths and gaps from the Tran-Blaha functional: Comparison with many-body perturbation theory. Phys. Rev. B: Condens. Matter, **87**, 075121 (2013).

21. Y. Yin, S. Xin, Y. Guo and L. Wan. Lithium–sulfur batteries: electrochemistry, materials, and prospects. Angew. Chem., Int. Ed., **52**, 13186–13200 (2013).

22. M. Song, E. J. Cairns and Y. Zhang. Lithium/sulfur batteries with high specific energy: old challenges and new opportunities. Nanoscale, **5**, 2186–2204 (2013).

23. M. Yu, W. Yuan, C. Li, J. Hong and G. Shi. Performance enhancement of a graphene–sulfur composite as a lithium–sulfur battery electrode by coating with an ultrathin Al_2O_3 film via atomic layer deposition. J. Mater. Chem. A, **2**, 7360–7366 (2014).

24. F. Sun, J. Wang, D. Long, W. Qiao, L. Ling, C. Lv and R. Cai. A high-rate lithium–sulfur battery assisted by nitrogen-enriched mesoporous carbons decorated with ultrafine La 2 O 3 nanoparticles J. Mater. Chem. A, **1**, 13283–13289 (2013).

Chapter 2

Structural and Compositional Characterization of Fungus-Derived Pyrolytic Carbon Architectures

2.1 Abstract

In this work, three distinctive pyrolytic carbon structures, derived from three specific tissues of *Agaricus bisporus* mushroom, were studied and characterized. The three structures discovered within the stalk, cap, and cap skin tissues were found to contain unique microarchitectures, which were preserved upon anoxic carbonization. Experiments also revealed the formation of salt pockets and deposits within each microarchitecture, leading to a potential natural hard-template method for porous carbon structures.

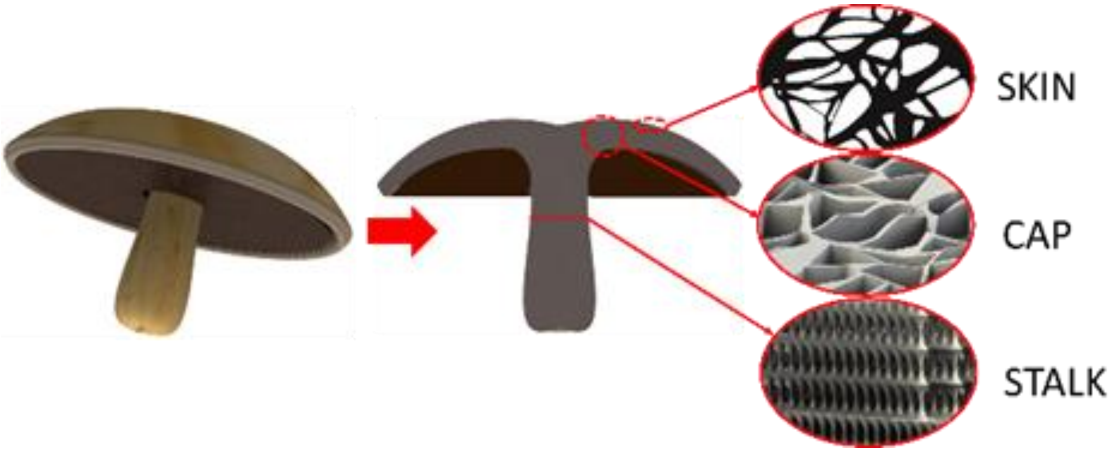

Figure 2.1: Schematic representation of the PM specimen, sectioning process and the modeled architecture of CST, CT, and ST, respectively.

2.2 Introduction

Functional carbonaceous materials are becoming increasingly attractive because of their light weight, low cost, versatility, mechanical properties and electronic conductivity.[1,2] Carbons of varying micro and nanostructures are potentially useful in a multitude of applications, from bulk and nanoscale materials, to structural and energy storage materials. The sources of carbon chosen for engineering purposes depends on the processing techniques necessary to produce such carbon, its scalability, and the specific properties desired. For example, carbon nanotubes (CNTs) have been the center of much interest to scientists and engineers for their wide body of applications.[3,4] Guo et al. used CVD-grown CNTs to confine sulfur in Li-S batteries with excellent efficiency and capacity over many charge-discharge cycles.[5] Amorphous carbons are also being studied for their diverse applications, and their ability to form pores of various sizes, acquiring microporosity (<2 nm pores), mesoporosity (2<x<50 nm pores) or macroporosity (>50 nm pores). Ouyang et al., for instance, have recently made progress in achieving amorphous, microporous carbon spheres with high polydispersity through polystyrene hypercrosslinking and hydrothermal decomposition.[6] The resultant nanospheres have great potential use in batteries, catalysis, medicine, etc.[7,8] Nowadays, carbonaceous foams are also of increasing interest, due to their free-standing nature, interconnectedness, and applications as bulk materials. Depardieu, et al. recently developed a carbonaceous foam as a lithium-sulfur battery electrode, with macroporosity as well as mesoporosity. Using both a silica hard template as well as triblock copolymer soft templates, a phenolic resin was introduced and pyrolyzed to form the porous carbon monolith.[9] Similar carbon foam-like structures have been obtained through the carbonization of biomass in the absence of oxygen. This method of bio-mediation yields diverse micro and nanostructured carbon materials, which can often be used as a free-standing monolith, or milled to form powders, depending on the application. A biomass-derived carbon foam was developed by Wang, et al. by liquefying birch sawdust into its resinous constituents, until it was able to become foamed and carbonized.[10] While a high surface area and bulk density were accomplished, the process required numerous steps, several toxic solvents, and strong acids and bases, ultimately making it an economically and environmentally costly material to scale up.

For the first time, we report on the pyrolysis-induced microarchitectures of three specific tissues of *Agaricus bisporus,* commonly known as the Portobello mushroom (PM). The elemental compositions and structural characteristics of Portobello sections were analyzed using various microscopic and spectroscopic techniques. The sections under study were the cap, stalk, and cap skin, each having distinct post-carbonization microarchitectures, which have profound potential to serve as functional and structural carbonaceous materials across various industries. Recently, we have demonstrated one of these pristine, free-standing carbon architectures as a high-performance carbon anode for lithium-ion batteries.[11] The resulting structures are obtained facilely, through a low-cost and scalable heat-treatment process that requires no expensive solvents, precursors, or work-ups. In this work, free-standing carbonaceous materials were synthesized via heat treatment of various tissues of the fungal fruiting body of *A. bisporus*. As summarized in Fig. 2.1, PMs were obtained, tissue samples were sectioned using razor blades and hole punches, and the samples were pyrolyzed. The carbonized PM tissues under study were:

cap tissue (CT), stalk tissue (ST) and cap skin tissue (CST). Initial SEM imaging of the carbonized PM tissue morphologies confirmed that the microstructures of the resulting carbonaceous materials were distinct from one another. What is more, the 3D configurations of each respective microstructure seem to have compelling functional patterns, which could be correlated to the biological utility of a living PM. While the CT displayed a random, cavernous foam-like microarchitecture, the ST exhibits a unidirectional sinter column-like arrangement, and the CST forms thin, high aspect ratio, interconnected carbon nanoribbons.

2.3 Materials and Methods

A typical experiment was carried out as follows: organic PMs were purchased from local markets and cleaned with DI H_2O. The stalks were removed from the caps, the skins were peeled from the caps, and the gills (located under the “hood” formed by the cap) were scraped out. Next, razor blades were used to slice the cap tissue into thin slices (~5 mm), as was the stalk tissue. The stalk tissue was sliced both vertically and horizontally to observe the anisotropic architecture. All samples were placed in a vacuum oven at 80^{o} C for 24 hours to remove as much moisture as possible. All samples were then transferred to a tube furnace. Under 700 Torr, Argon gas was flowed at 300 SCCM, and the temperature was ramped from 21-600^{o} C over 60 minutes. The temperature was held at 600^{o} C for 5 hours, and then allowed to cool slowly. The CTs, STs and CSTs were removed and analyzed. A number of the samples were studied as-synthesized, while others were washed in DI H_2O to further understand their composition. Additional experiments were carried out at higher temperatures, during which the escaping of molten KCl salts induced the formation of pores of various sizes, a phenomenon which was first reported in our previous lithium-ion battery work.[11]

2.4 Results and Discussion

Morphologies of the carbonized CTs, STs and CSTs were studied using scanning electron microscopy (SEM). Fig. 2.2a-c capture the microarchitecture of the CTs, which is a disordered carbon foam-like structure. The walls of the foam range between a few microns to several tens of microns. In general, the structure of the CT is very macroporous and random. The structure is also decorated with small, round pockets, which were found from later study to be biological salts (principally KCl) localized into pockets and surface deposits. A vertical ST section is shown in Fig. 2.2d-f, revealing a carbon microarchitecture resembling stacked, vertically-aligned and unidirectional sinter columns. At low magnification (Fig. 2.2d), the uniform, aligned ordering of the sinter columns is evident. The linear direction from the lower-left hand corner of the image to the upper-right hand corner is parallel to the line formed from the base of the PM stalk to the center of the cap. It is thus inferred that, in the live PM specimen, this arrangement contributes to the strength of the stalk and the ability of the stalk structure to support the large cap. The cap of a mature PM can make up anywhere between 70-80% of the weight of the entire fruiting body, according to our gravimetric measurements. Typically, the diameter of the middle of the sinter columns are anywhere between 5-10 μm, while the bases of the columns and connection points are several tens of microns thick. There is also evidence that the ordered

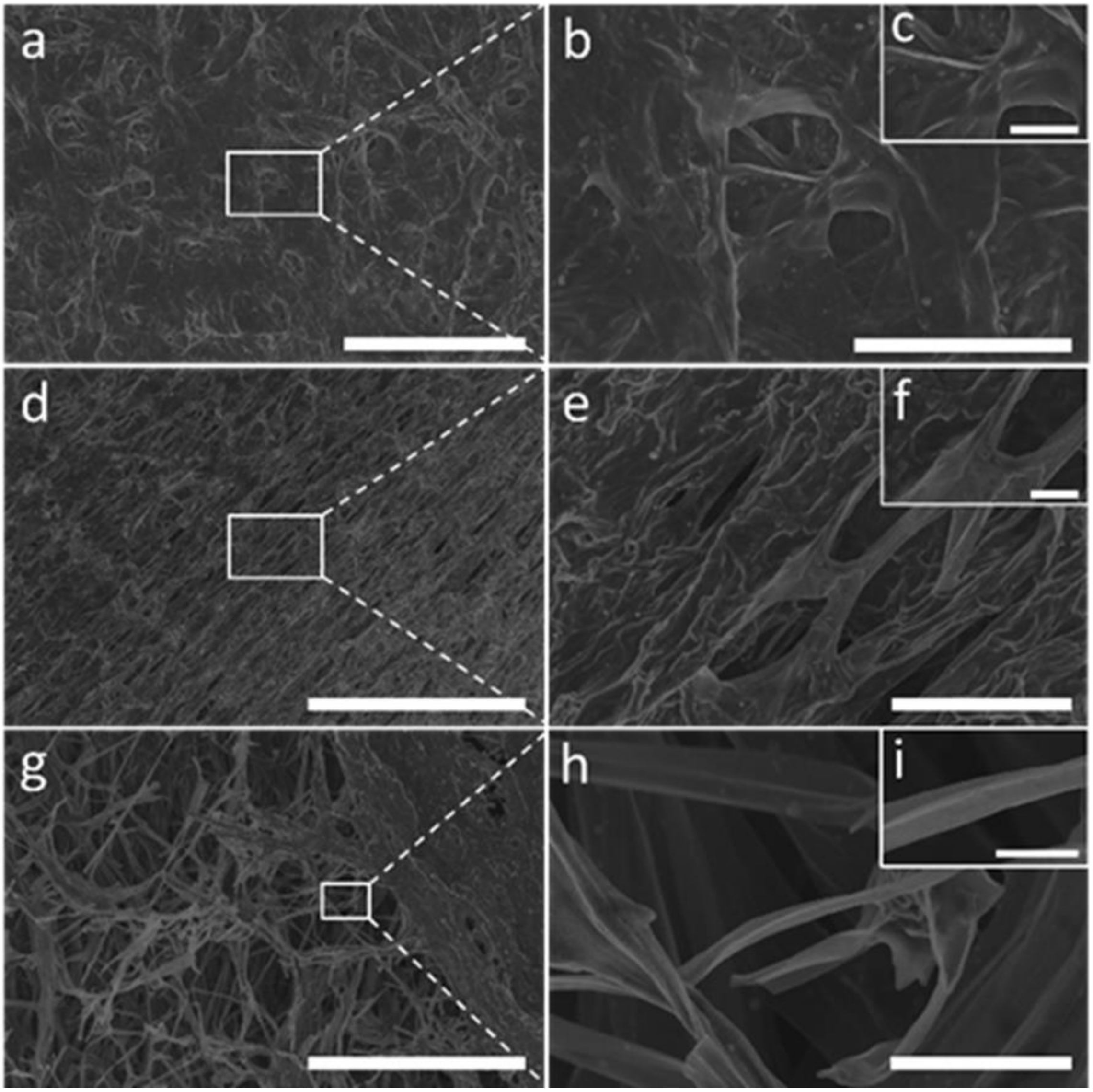

Figure 2.2: SEM micrographs, low to high magnification, of CT (a-c) (scale bars = 200 μm, 40 μm, 10 μm), ST (d-f) (scale bars = 400 μm, 50 μm, 10 μm), and CST (g-i) (scale bars = 300 μm, 20 μm, 4 μm).

columns are hierarchical in nature; optical microscopy of the stalk tissue before carbonization, shown in Figures S1(c)-S1(d) in Supplementary Material available online at http://dx.doi.org/10.1155/2016/9843875 (Fig. 2.6c-d in this dissertation), seems to indicate that larger columns are comprised of smaller fibers, which may contribute to the size variation of columns seen under SEM. Similar to the CTs, the STs appear to contain salt pockets, seen clearly in Fig. 2.2e. Finally, the CST micrographs display an interconnected carbon nanoribbon architecture, observed in Fig. 2.2g-i. This structure is distinct from the CT and ST, in that these ribbons are remarkably thin; they are approximately 23 nm in thickness, more clearly seen in Fig. S2 (Fig. 2.7 in this dissertation). The low thickness of the ribbons partially renders them transparent under SEM. The width of the nanoribbons varies from 5-6 μm to tens of microns. The CST samples also exhibit salt and pockets and deposits which predominantly form diameters on the order of nanometers to multiple microns (see Fig. 2.2i and Fig. S3 (Fig. 2.8 in this dissertation)). The generally high aspect ratio of the CST nanoribbons lends to the hypothesis that they, depending on the processing temperature, would exhibit good performance in devices which require high surface area, such as electric double-layer capacitors, which depend on the ability to store surface charge.[12]

In addition to observing morphology, compositional analysis was conducted on the PM samples. Using high-resolution energy-dispersive X-ray spectroscopy (EDS), great detail was achieved in terms of the elemental distribution in the CT, ST, and CST; elemental mapping of the pristine and unwashed CT, and the CT after washing in DI H_2O overnight, are shown in Fig. 2.3 and Fig. 2.4, respectively. The elemental maps of the ST and CST, before and after DI H_2O washing, are included in Fig. S4 and S5, respectively (Fig. 2.9 and 2.10 in this dissertation). A defining attribute of this analysis is the presence of biological salts that are present before the DI H_2O washing (Fig. 2.3a,b), and are dramatically reduced after the washing (Fig. 2.4a,b). Interestingly, the salts become located in pockets of various sizes, which are well-highlighted in the element composite image in Fig. 2.3b. These disappear in the post-wash composite image in Fig. 2.4b. While the weight percentage of oxygen is marginally changed from DI H_2O washing, carbon is significantly increased, and nearly every other major mineral present is decreased. Notably, the K and Cl peaks are diminished from 16 and 3.3 wt. %, respectively (Fig. 2.3d) to 5.1 and virtually 0 wt. %, respectively (Fig. 2.4d). Thus, the primary elements found in the salts of the PM are K and P, which is consistent with literature values for fresh Agaricus species.[13,14] The P content remains relatively constant after DI H_2O washing; this somewhat correlates with the unchanged O concentration, and may be attributed to the presence of phosphate species and phospholipids, which typically occur in A. bisporus.[15,16] The phenomenon of salt-pocketing upon carbonization in this particular fungal biomass has important implications when it comes to carbon microarchitecture engineering; depending on heat-treatment temperature, these pockets may serve as a natural hard template for generating pores.[11] Furthermore, this phenomenon should compel further comparative study into the roles of biological salts in carbonization of other various forms of biomass such as plant matter, due to the differences in organic polymer/oligomer compositions. The organics in the cell walls of A. bisporus, unlike plants, contain a relatively high concentration of the polysaccharide chitin, upwards of about 10% dry mass, with the stalk tissues containing slightly higher concentrations.[17] Chitin is as an important, nitrogen-containing structural

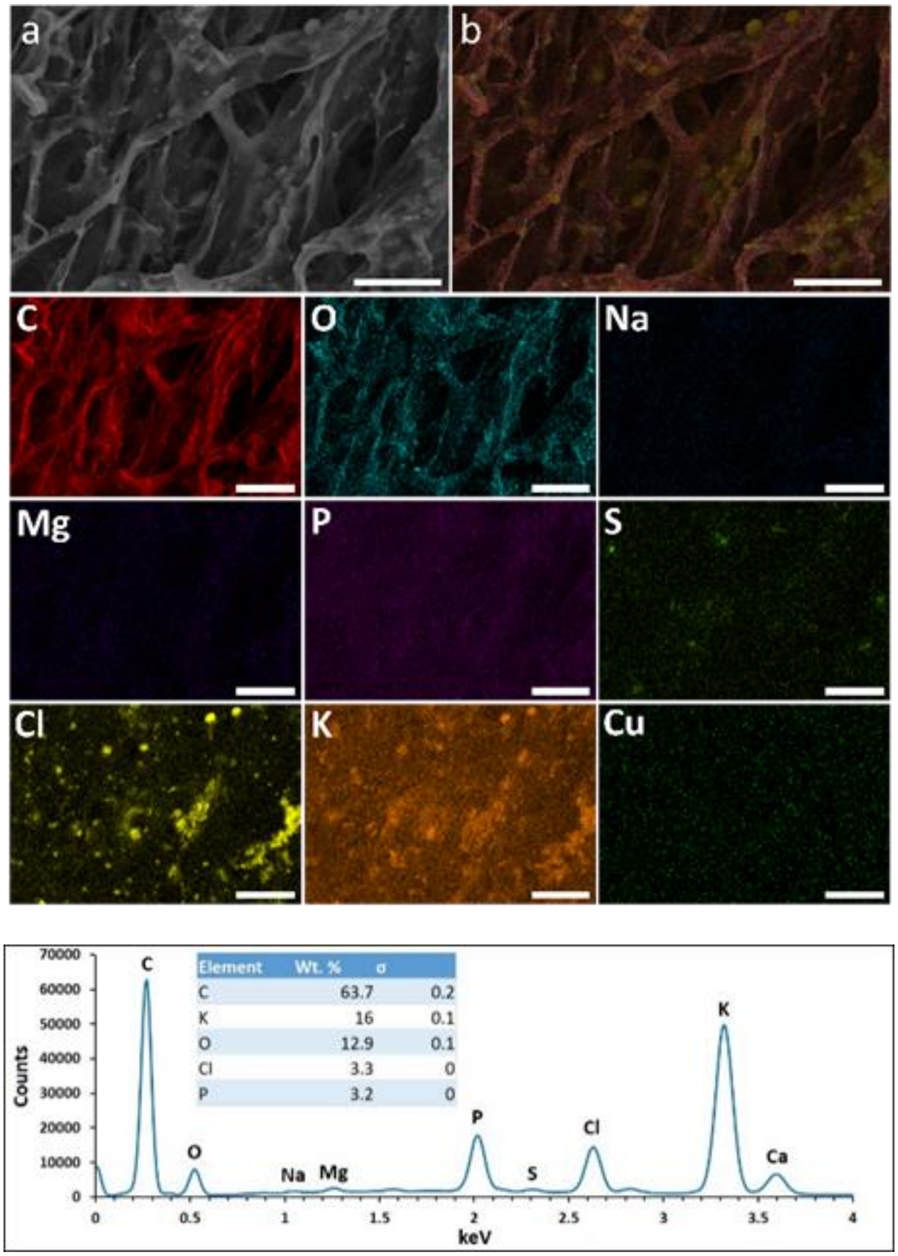

Element	Wt. %	σ
C	63.7	0.2
K	16	0.1
O	12.9	0.1
Cl	3.3	0
P	3.2	0

Figure 2.3: Elemental mapping of CT before DI H2O wash, including the raw electron image (a), composite image (b), and maps of most prominent elements in the specimen (all scale bars = 25 μm), with accompanying EDS spectrum (d).

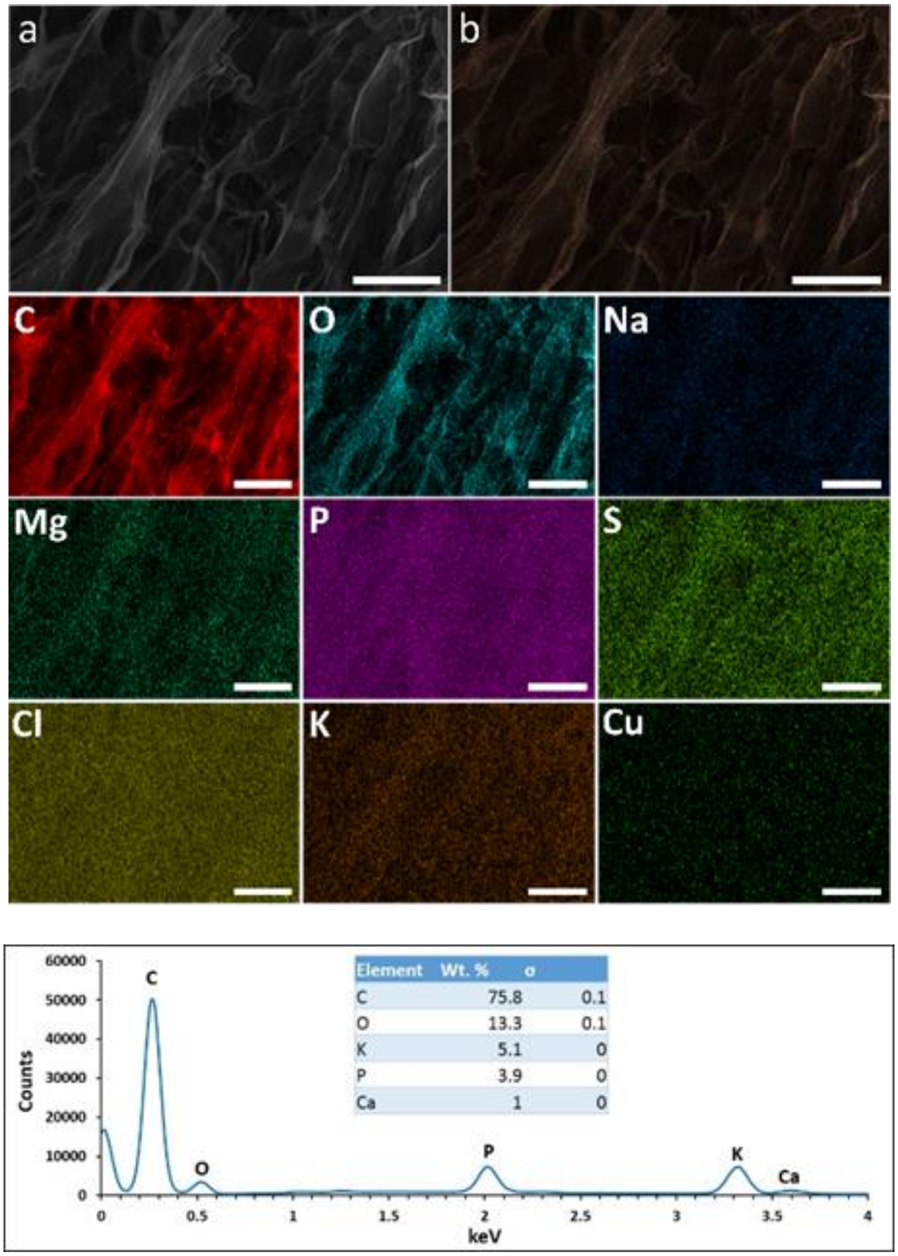

Element	Wt. %	σ
C	75.8	0.1
O	13.3	0.1
K	5.1	0
P	3.9	0
Ca	1	0

Figure 2.4: Elemental mapping of CT after DI H2O wash, including the raw electron image (a), composite image (b), and maps of most prominent elements in the specimen (all scale bars = 25 μm), with accompanying EDS spectrum (d).

polysaccharide for vertical growth of the fungal fruiting body, and is vital for the fungus' survival through spore dispersal. Scanning electron microscopy and energy-dispersive X-ray spectroscopy characterization was performed using an FEI Nova NanoSEM450.

Spectral data were obtained for the three carbonized tissues, including X-ray diffraction (XRD) and X-ray photoelectron spectroscopy (XPS), to analyze phases present in the as-prepared carbonized samples. Pristine samples of the CT, ST, and CST were prepared by carbonizing slices of each tissue with a thickness of 3-4 mm, which resulted in carbonized disk-shaped samples of about 1-3 mm in thickness. The strong peaks observed in Fig. 2.5a at 2θ: 28.5, 40.6, 51.0, 58.8, 66.5, and 74.0 correlate to the diffraction angles of cubic crystalline KCl.[18] The less intense, rounder peak at 2θ: 31.3, however, is characteristic of the primary peak of NaCl.[19] The XRD spectra for the pristine, unwashed samples indicate principally alkali metal halide salts. Finally, the slightly elevated downfield region (between 2θ: 20 and 35) correlate to amorphous carbon.[20] The XRD spectrum of post-DI H_2O washed samples is shown in Fig. 2.5b, where it is shown that the halide salt presence is significantly reduced. There is still a noticeable presence of KCl and NaCl in the samples, although the intensity diminished by a large factor, which agrees well with the post-wash EDS of the CT. The elevated downfield region associated with amorphous carbon is also more prominent in the post-wash XRD analysis. Overall, the order of strongest halide salt peaks from largest to smallest is the ST, CST, and CT, respectively. For the post-wash XRD CT sample, the salt peaks are almost entirely absent. XPS was also used to identify surface composition and bonding in the carbon

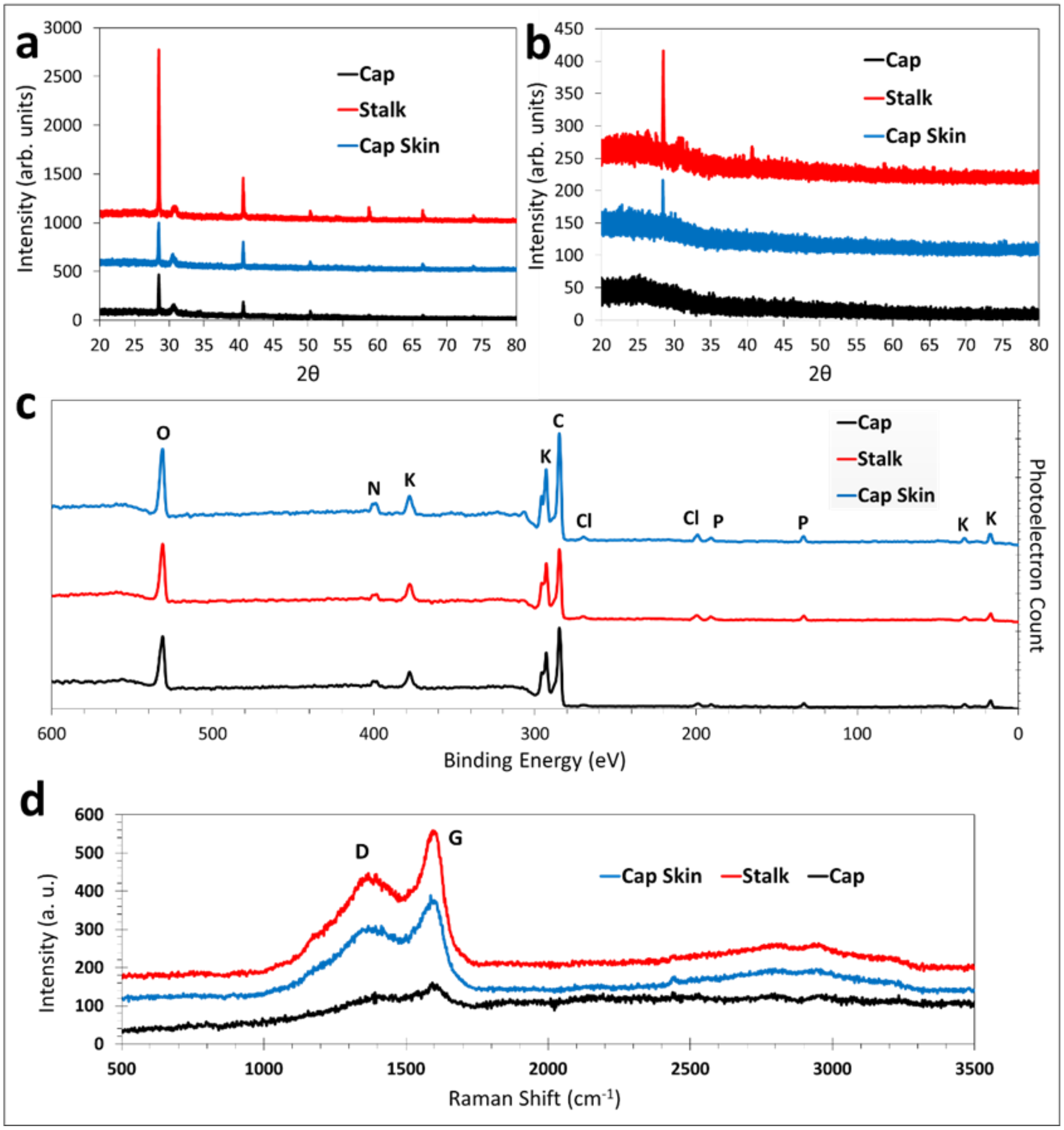

Figure 2.5: Spectral data from CT (Cap), ST (Stalk) and CST (Cap Skin), including XRD spectra from pre-DI H2O wash (a), and post-DI H2O wash (b), XPS of pristine, unwashed samples (c), and Raman spectra of washed CT, ST and CST samples (d).

architectures. The PM samples used for XPS were pristine, unwashed, and in their free-standing form to more accurately identify species other than typical organic bonds. For each sample type, the signature peaks for C, O, K, P, Cl, and N were prominent. The strength of each peak showed no significant change between tissue types. The strong presence of K observed in all forms of analysis in this study are expected, and is not attributed to contamination of the specimen before purchasing. Raman spectroscopy was carried out on the three freestanding mushroom tissues to analyze the type of carbon under study. After the annealing between 500-600^{o}C, Raman spectra were taken and the data is shown in Fig. 2.5d. The Raman data above gives good insight as to the crystalline nature of the fungus-derived carbons. It has been determined that the D and G peaks, ~1365 and 1594 cm^{-1} respectively, indicated the presence of graphitic carbon. Upfield, between 2500 and 3300 cm^{-1}, there is a large broad hump with a noticeable pair of peaks at 2804 and 2951 cm^{-1}, respectively. The exact nature of the pyrolytic carbon is a mixture of allotropes, but mostly resembles hard carbon-type, with strong graphitic nature. The graphite microdomains, however, are turbostratically arranged, meaning there is short-range order as well as significant 3D-rotation of the microdomains. It can be seen from this data, based on the peak intensities, that the CT has the lowest crystallinity and the ST has the highest crystallinity, with the CST lying in between.

2.5 Conclusions

The examination of Portobello mushroom (PM) sections from the cap tissue (CT), stalk tissue (ST) and cap skin tissue (CST) was carried out after carbonization at 600^{o}C for 5 hours. The resulting architectures at the micro-scale lead to new insights which are compelling for future biomimetic and/or bio-inspired materials engineering endeavours.

The carbonization of the chitin-containing PM biomass resulted in microstructures of the following types: CT forms a randomly-oriented, macroporous, thicker-walled carbon foam structure, ST forms a unidirectional, elongated sinter column-like structure, and CST assumes an interconnected carbon nanoribbon structure. The elemental compositions of each section were analyzed through EDS, XRD and XPS. Results indicate that the as-synthesized samples have, in addition to carbon and oxygen, a significantly high concentration of potassium, phosphorus, chlorides, among other trace minerals, located in pockets and surface deposits. Raman analysis suggests the carbon is a graphitic, yet highly disordered, carbon most closely resembling hard carbons.

The authors would like to thank UC Riverside and the National Science Foundation for their support, and Lauro Zavala for artistic contributions.

The authors declare that there are no conflicts of interest regarding the publication of this paper.

2.6 Supporting Information

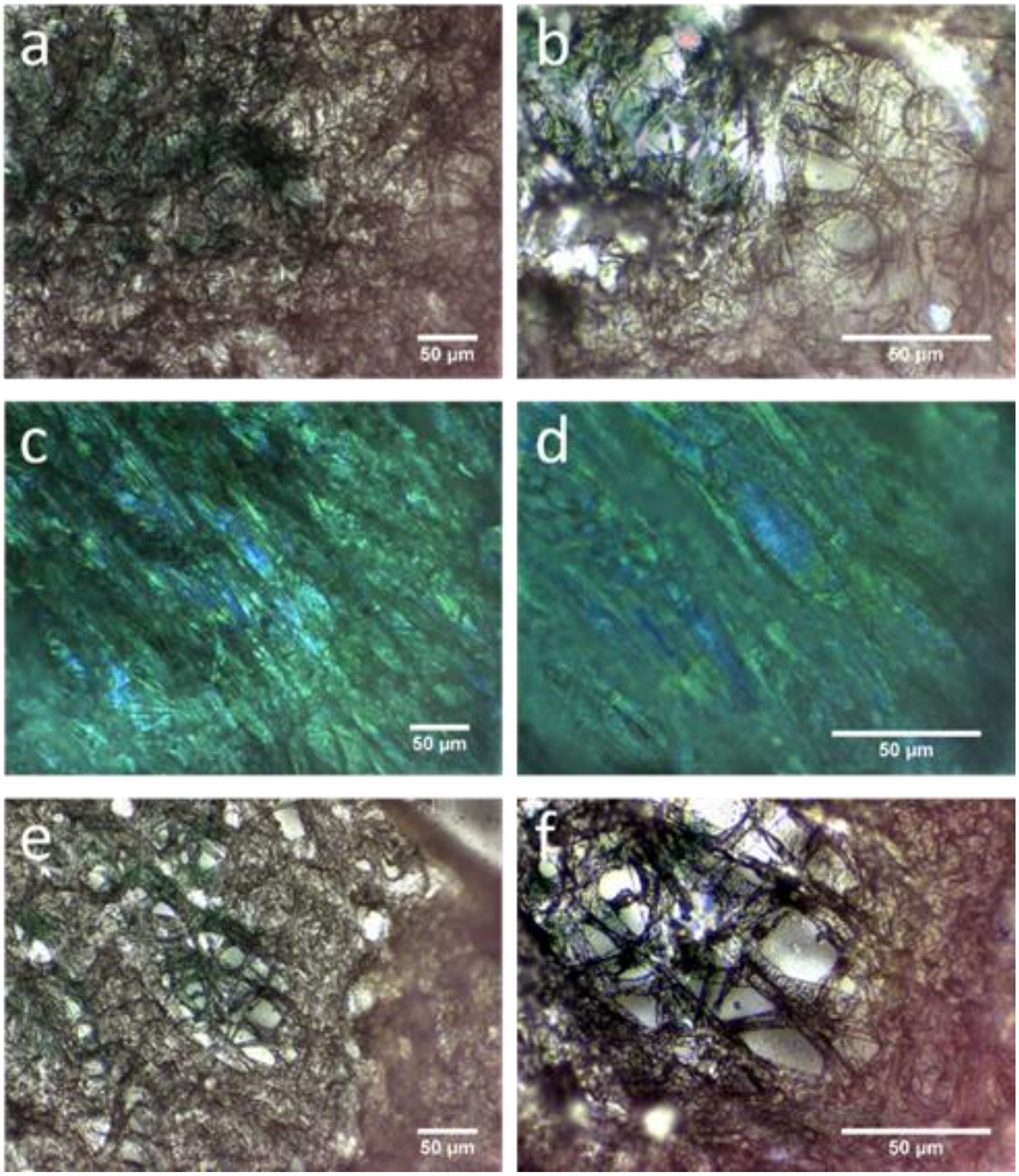

Figure 2.6: Optical micrographs of dehydrated, non-carbonized PM sections, including cap tissue (a,b), stalk tissue (c,d), and cap skin tissue (e,f) (all scale bars = 50 μm).

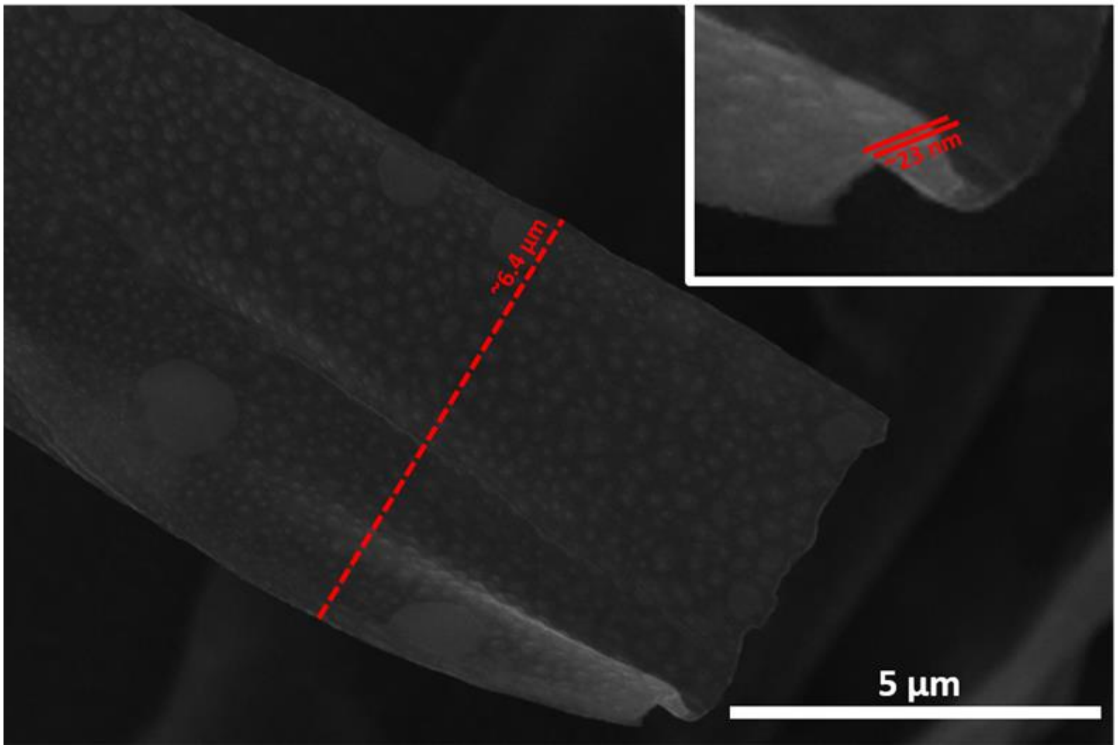

Figure 2.7: SEM micrograph of a carbon nanoribbon resulting from carbonization of CST, including dimensions of the width (a) and approximate thickness (b) of the ribbons.

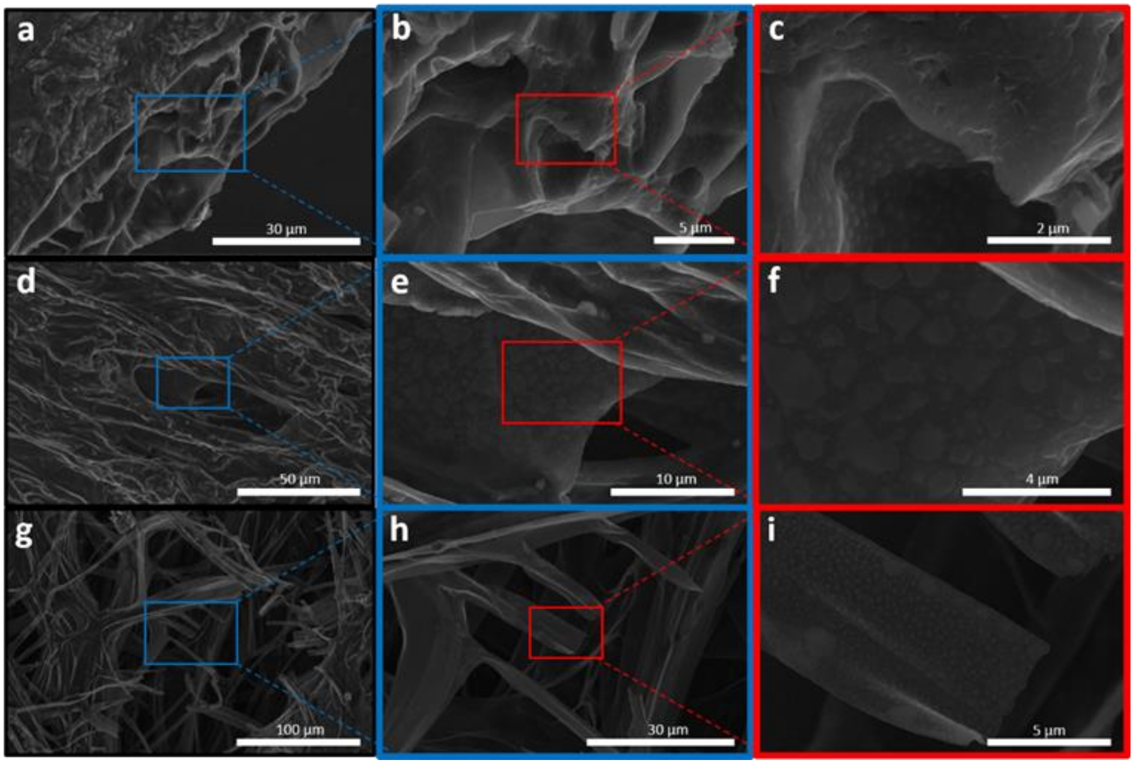

Figure 2.8: Low to high magnification SEM of carbonized PM tissues showing presence of surface salt deposits, including CT (a-c, respectively), ST (d-f, respectively), and CST (g-i, respectively). Patches/pockets are clearly seen in c, f and i. Scale bars included in images.

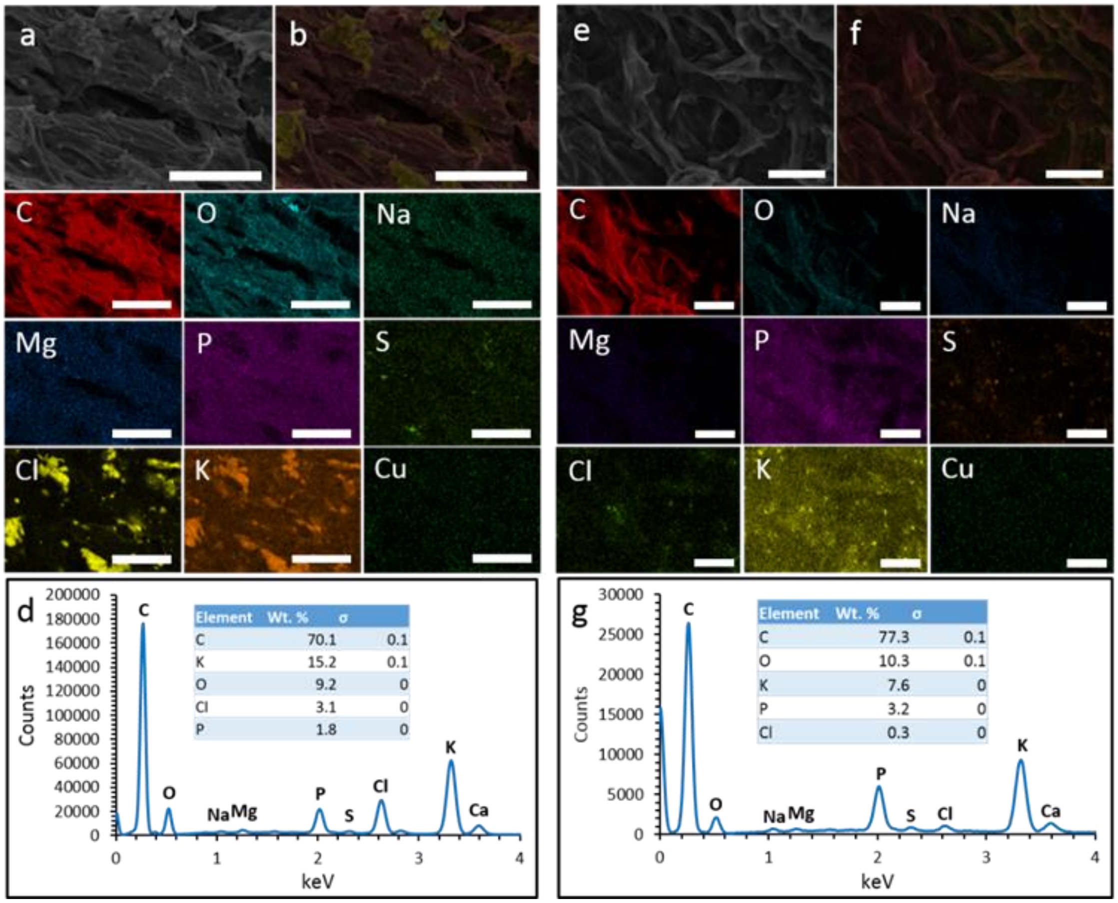

Element	Wt. %	σ
C	70.1	0.1
K	15.2	0.1
O	9.2	0
Cl	3.1	0
P	1.8	0

Element	Wt. %	σ
C	77.3	0.1
O	10.3	0.1
K	7.6	0
P	3.2	0
Cl	0.3	0

Figure 2.9: Elemental maps of most prominent elements found in carbonized ST. Including raw electron image (a), composite image (b), and EDS spectrum (d) of unwashed ST sample, and raw electron image (e), composite image (f), and EDS spectrum (g) of DI H_2O washed sample (Scale bars = 25 um).

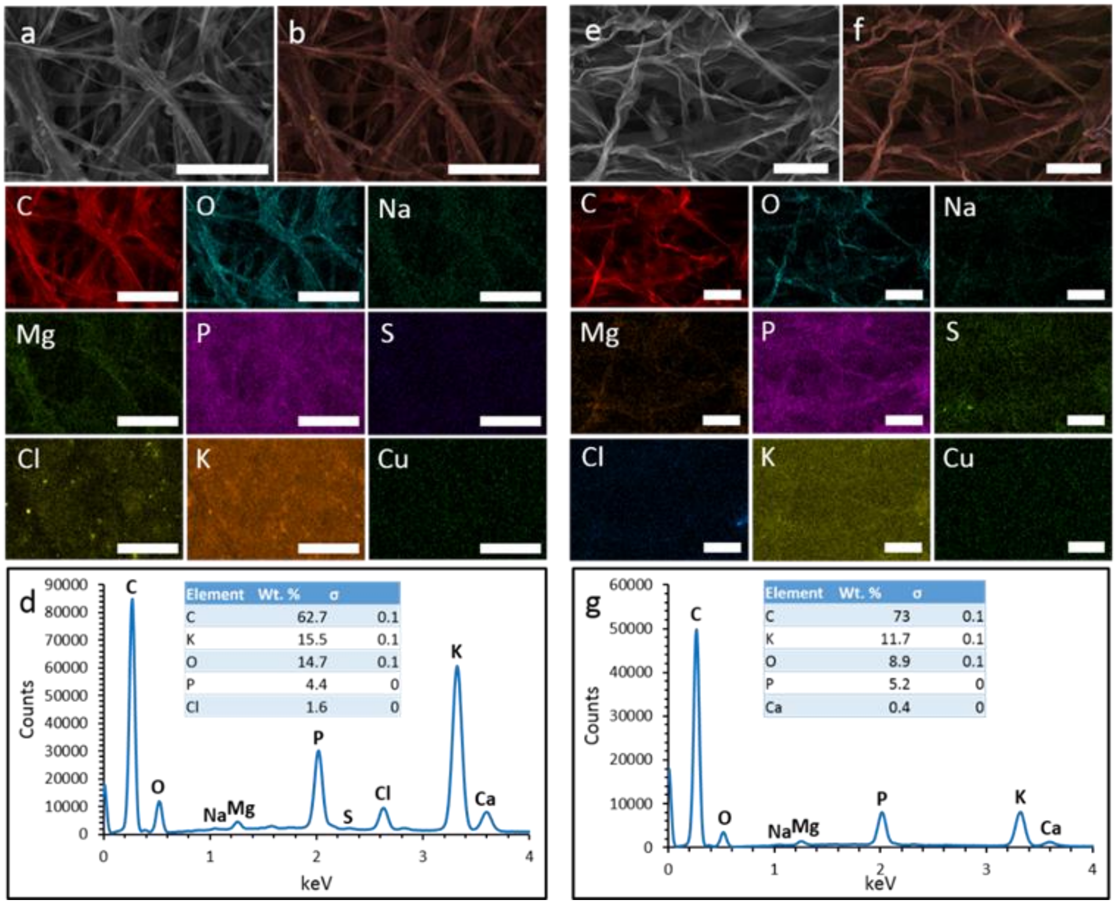

Figure 2.10: Elemental maps of most prominent elements found in carbonized CST. Including raw electron image (a), composite image (b), and EDS spectrum (d) of unwashed CST sample, and raw electron image (e), composite image (f), and EDS spectrum (g) of DI H2O washed sample (Scale bars = 50 μm).

References

1. H. Chen, M. B. Muller, K. J. Gilmore, G. G. Wallace, and D. Li. Mechanically strong, electrically conductive, and biocompatible graphene paper. Adv. Mater., **20**, 3557-3561 (2008).

2. A. Lu, G. Hao, Q. Sun, X. Zhang, and W. Li. Chemical synthesis of carbon materials with intriguing nanostructure and morphology. Macromol. Chem. Phys., **213**, 1107-1131 (2012).

3. C. Gao, Z. Guo, J. Liu, and X. Huang. The new age of carbon nanotubes: An updated review of functionalized carbon nanotubes in electrochemical sensors. Nanoscale, **4**, 1948-1963 (2012).

4. M. F. L. De Volder, S. H. Tawfick, R. H. Baughman, and A. J. Hart. Carbon nanotubes: present and future commercial applications. Science, **339**, 535-539 (2013).
5. J. Guo, Y. Xu, and C. Wang. Sulfur-impregnated disordered carbon nanotubes cathode for lithium–sulfur batteries. Nano Lett., **11**, 4288-4294 (2011).

6. Y. Ouyang, H. Shi, R. Fu, and D. Wu. Highly monodisperse microporous polymeric and carbonaceous nanospheres with multifunctional properties. Sci. Rep., **3**, 1430 (2013).

7. B. Zhang, X. Qin, G. R. Li, and X. P. Gao. Enhancement of long stability of sulfur cathode by encapsulating sulfur into micropores of carbon spheres. Energy Environ. Sci., **3**, 1531-1537 (2010).

8. W. K. Oh, H. Yoon, and J. Jang. Size control of magnetic carbon nanoparticles for drug delivery Biomaterials, **31**, 1342-1348 (2010).

9. M. Depardieu, R. Janot, C. Sanchez, A. Bentaleb, C. Gervais, M. Birot, R. Demir-Cakan, R. Backov, and M. Morcrette. Carbonaceous multiscale-cellular foams as novel electrodes for stable, efficient lithium–sulfur batteries. RSC Adv., **4**, 23971-23976 (2014).

10. R. Wang, W. Li, and S. Liu. A porous carbon foam prepared from liquefied birch sawdust. J. Mater. Sci., **47**, 1977-1984 (2012).

11. B. Campbell, R. Ionescu, Z. Favors, C. S. Ozkan, and M. Ozkan. Bio-Derived, Binderless, Hierarchically Porous Carbon Anodes for Li-ion Batteries. Sci. Rep., **5**, 14575 (2015).

12. C. Zhang, Z. Peng, J. Lin, Y. Zhu, G. Ruan, C. Hwang, W. Lu, R. H. Hauge, and J. M. Tour. Splitting of a vertical multiwalled carbon nanotube carpet to a graphene nanoribbon carpet and its use in supercapacitors. ACS Nano, **7**, 5151-5159 (2013).

13. J. Vetter. Chemical composition of fresh and conserved Agaricus bisporus mushroom. Eur. Food. Res. Technol., **217**, 10-12 (2003).

14. P. Mattila, K. Konko, M. Eurola, J. Pihlava, J. Astola, L. Vahteristo, V. Hietaniemi, J. Kumpulainen, M. Valtonen, and V. Piironen. Contents of vitamins, mineral elements, and some phenolic compounds in cultivated mushrooms. J. Agric. Food Chem., **49**, 2343-2348 (2001).

15. A. Braaksma, P. van der Meer, and D. J. Schaap. Polyphosphate accumulation in the senescing mushroom Agaricus bisporus. Postharvest Biol. Technol., **8**, 121-127 (1996).
16. P. F. S. Byrne and P. J. Brennan. The lipids of Agaricus bisporus. Microbiology, **89**, 245-255 (1975).

17. J. Vetter. Chitin content of cultivated mushrooms Agaricus bisporus, Pleurotus ostreatus and Lentinula edodes. Food Chemistry, **102**, 6-9 (2007).

18. K. Lin, Y. Mai, S. Li, C. Shu, and C. Wang. Characterization and Hydrogen Storage of Surface-Modified Multiwalled Carbon Nanotubes for Fuel Cell Application. Journal of Nanomaterials, **2012**, 1-12 (2012).

19. S. Kiel, O. Grinberg, N. Perkas, J. Charmet, H. Kepner, and A. Gedanken. Forming nanoparticles of water-soluble ionic molecules and embedding them into polymer and glass substrates. Beilstein J. Nanotechnol., **3**, 267-276 (2012).

20. X. Yang, C. Li, W. Wang, B. Yang, S. Zhang, and Y. Qian. A chemical route from PTFE to amorphous carbon nanospheres in supercritical water. Chem. Commun., 342-343 (2004).

Chapter 3

Bio-derived, Binderless, Hierarchically Porous Carbon Anodes for Li-ion Batteries

3.1 Abstract

Here we explore the electrochemical performance of pyrolyzed skins from the species *A. bisporus*, also known as the Portobello mushroom, as free-standing, binder-free, and current collector-free Li-ion battery anodes. At temperatures above 900 °C, the biomass-derived carbon nanoribbon-like architectures undergo unique processes to become hierarchically porous. During heat-treatment, the oxygen and heteroatom-rich organics and potassium compounds naturally present in the mushroom skins play a mutual role in creating inner void spaces throughout the resulting carbon nanoribbons, which is a process analogous to KOH-activation of carbon materials seen in literature. The pores formed in the pyrolytic carbon nanoribbons range in size from sub-nanometer to tens of nanometers, making the nanoribbons micro, meso, and macroporous. Detailed studies were conducted on the carbon nanoribbons using SEM and TEM to study morphology, as well as XRD and EDS to study composition. The self-supporting nanoribbon anodes demonstrate significant capacity increase as they undergo additional charge/discharge cycles. After a pyrolysis temperature of 1100 °C, the pristine anodes achieve over 260 mAh/g after 700 cycles and a Coulombic efficiency of 101.1%, without the use of harmful solvents or chemical activation agents.

3.2 Introduction

Carbon materials are of great importance to a range of battery chemistries. Carbon is the most versatile element on the periodic table, and its various allotropes make for highly diverse properties and applications. In Li-ion batteries, carbon has been studied for decades. The current industry standard for rechargeable Li-ion battery anodes is synthetic graphite. While graphite has commercially desirable attributes, such as a high cycling stability and low hysteresis, it comes with its own trade-offs. The disadvantages of graphite are that it is relatively expensive to make and has a relatively low lithium storage capacity per carbon weight (LiC_6)[1]. Alternatives to graphitic carbons for Li-ion anodes are hard carbons and soft carbons, which can be synthesized in a number of ways. A traditional form of hard carbon synthesis involves the pyrolysis of sucrose, a natural organic sugar. Studies conducted by Buiel and Dahn show that hard carbon anodes yield higher specific capacities than graphitic structures (over 500 mAh/g). However, they tend to have significant irreversible capacity, owing to lithium's reactivity with both the electrolyte and the surface functional groups of the carbon structure which form after pyrolysis[2]. In terms of commercializing new forms of carbon for Li-ion batteries, naturally-derived carbon precursors must be explored. Activated carbons are also showing incredible promise for implementation as scalable, commercially-viable Li-ion anodes. Activated carbons are most commonly produced from exposure to a concentrated KOH solution, or other chemical activating agents. KOH treatment generates additional mesopores and/or micropores after thermal activation; the resulting defects encourage higher capacities by allowing additional lithium insertion into the carbon[3]. A traditional method for activating carbon involves submersion in a KOH bath, followed by a high-temperature heat-treatment. For KOH activation, two modes of action are thought to be at play for pore generation, such as reaction of carbon with metallic K, as well as CO and CO_2 formation[3,4]. Hwang, *et al.* explored the efficacy of coffee shell-derived activated carbon as a Li-ion anode, which they activated using KOH and an array of other activating agents. This process produced an anode with a nearly 300 mAh/g reversible capacity over 15 cycles, with an impressive initial capacity of over 1100 mAh/g[5]. There are several nuances to characterizing high-performance biomass-derived carbon anodes for Li-ion batteries, due to their complex organic compositions. Biomass-derived electrode materials are of great interest because of their high carbon content, low cost, and environmental benignity[6].

In this work, we study the electrochemical performance of pyrolytic carbons derived from the cap skin tissue (CST) of the mature fruiting body of the fungus, A. bisporus, otherwise known as the Portobello mushroom (PM). Our studies of the PM CSTs have revealed compelling microstructural features after anoxic carbonization. Specifically, we discovered that the pyrolyzed PM CST formed high aspect-ratio carbon nanoribbons. Additionally, we confirmed remarkably high concentrations of salts after carbonization, primarily KCl. Further, PM CSTs were examined after various pyrolysis temperatures (PTs) to compare microstructural and compositional changes with corresponding electrochemical behaviour. The purpose of this method is to observe the true performance of bio-derived structures as battery electrodes (i.e., without binder, conductive additive, etc.), and to examine the characteristics of the resulting pristine carbon. To this end, the PM CST anodes were placed in a Li-ion battery half-cell configuration, completely as-

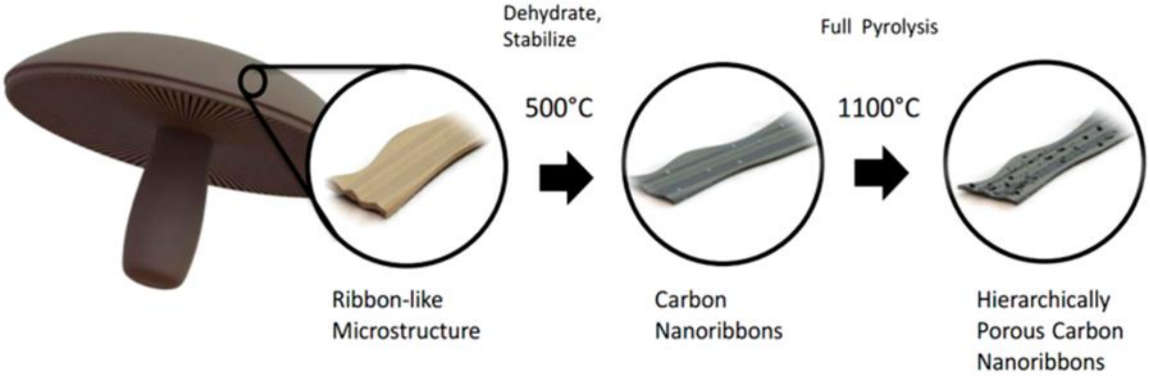

Figure 3.1: Schematic illustration of the process of obtaining Portobello mushroom skin-derived, hierarchically porous carbon nanoribbons used as free-standing, binder-free, current collector-free carbon anodes.

synthesized. In further SEM studies, the PM CSTs manifested hierarchical porosity after PT above 900 °C, showing macro, meso, and micropores, as illustrated in the schematic in Fig. 3.1. This raised an interesting possibility with this unique material; PM CSTs may, due to their unusually high K concentration, be self-activating. However, synthetic processes need to be optimized to expose the microchannels or worm-like micropores formed during pyrolysis, and thereby increase the measurable surface area. These novel PM CST anodes are binder-free, requiring zero polymers or conductive additives, to attain capacities that are comparable to practical graphite-based electrodes. Binder-free Li-ion electrodes are far superior to graphite-based electrodes, due to their higher utilization of total electrode weight as active material, and minimal processing. In turn, this translates to batteries with higher energy density, lower cost, and lower environmental impact.

3.3 Results

Structural characterization was conducted on the PM CSTs using SEM, observing pyrolysis-induced morphological transformations at the micro- and nanoscale. From the micrographs in Fig. 3.2, it can be seen that the common microstructural feature is nanoribbons, with a sometimes wrinkled appearance. They make up an extremely thin, secondary electron-transparent array of interconnected, branching ribbons with widths of about 10 μm, lengths of several tens of microns or longer, and a thickness of about 20–100 nm. A key structural difference making 700CSTs (Fig. 3.2a,b) distinct from 900CSTs (Fig. 3.2c,d) and 1100CSTs (Fig. 3.2e,f) is the presence of round salt pockets. These salt pockets are thought to form during heating, as water escapes and naturally-present biological salts aggregate, both within the chitin-based organics, and on the surface. At temperatures above 900 °C, these salt pockets disappear, having exceeded the melting points of most salts present. It should also be noted that, especially in Fig. 3.2a,e, the nanoribbons form a network. There is also layering and/or pseudo-layering, as evidenced in Fig. 3.2c, which shows a lateral view of the layered ribbon networks.

Observations were also made on higher-magnification SEM micrographs of the various PM CSTs. As mentioned, biological salts (primarily KCl) organize in pockets of varying sizes, and begin to create additional void space at 700 °C. However, the melting point of KCl is 770 °C, and above this temperature the salts escape the carbon structure more completely. As captured in Fig. 3.3a,b, salt deposits are still present at the surface of the nanoribbons, having a wide

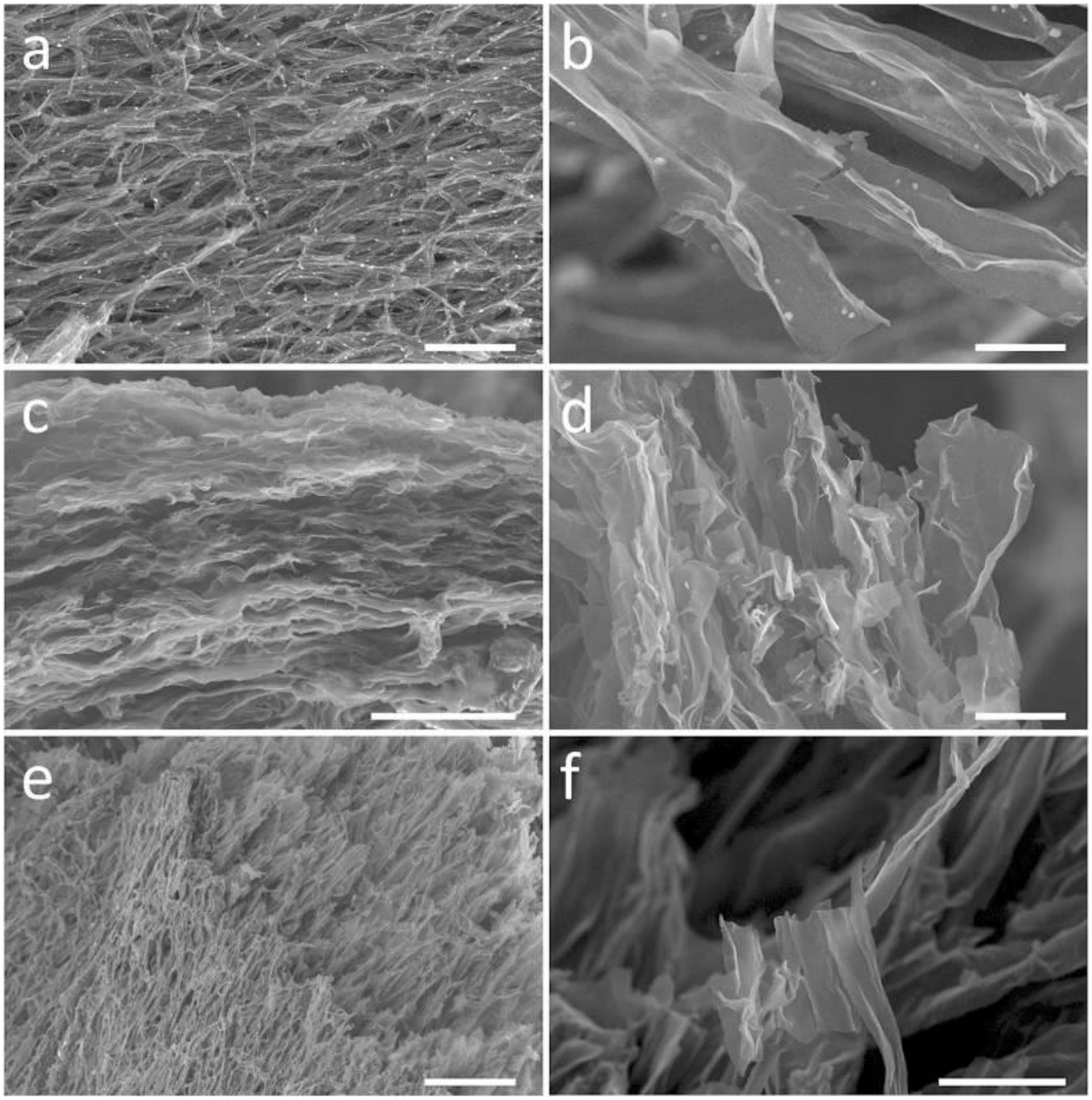

Figure 3.2: Low to high magnification SEM of PM CST anodes heat-treated at 700 °C (a,b), 900 °C (c,d), and 1100 °C (e,f) (scale bars for (a–f), respectively: 100 μm, 10 μm, 50 μm, 10 μm, 100 μm, and 10 μm).

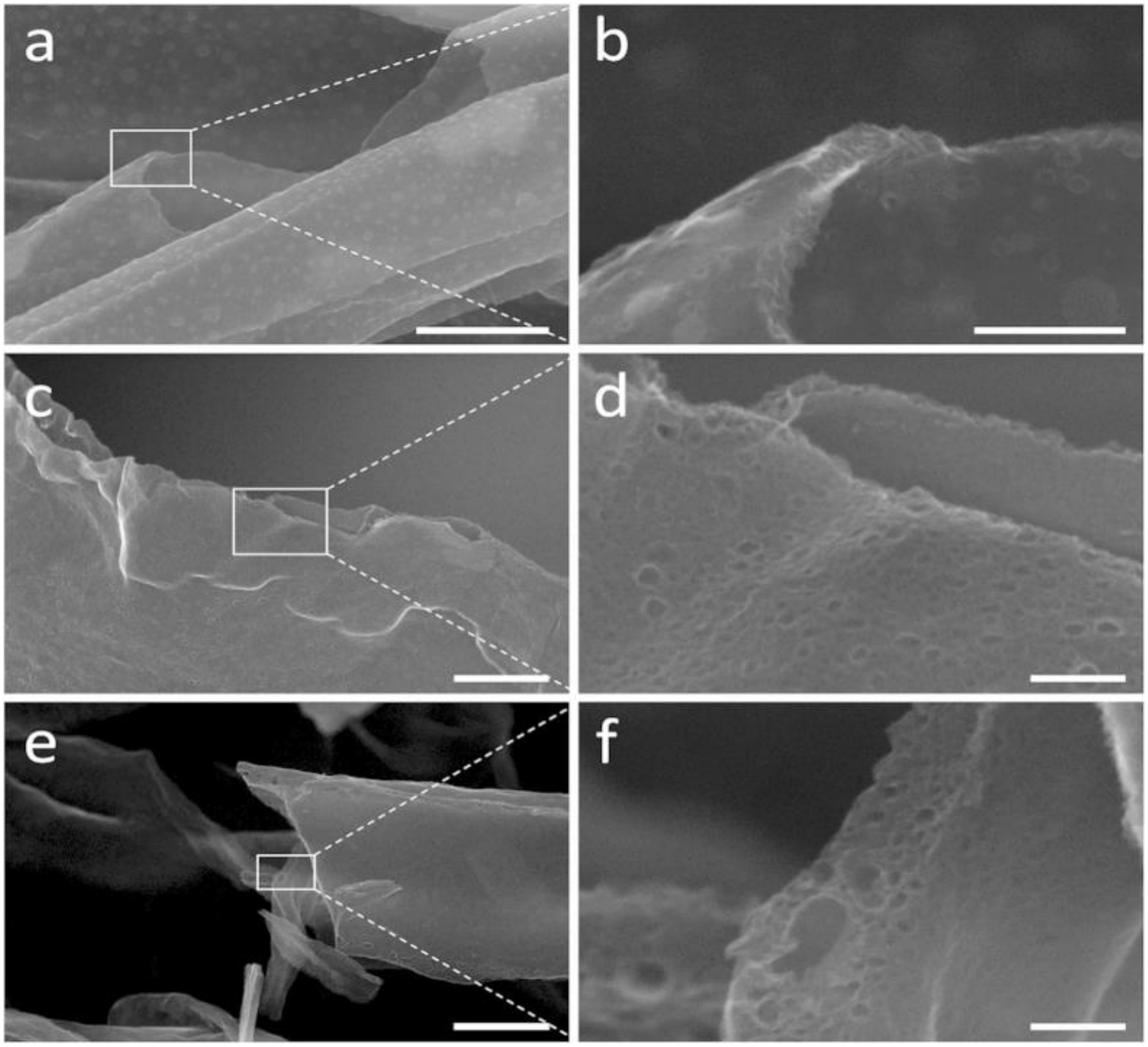

Figure 3.3: Low to high magnification SEM showing the increasing degree of porosity of PM CST nanoribbons as temperature increases, including sample heat-treated at 700 °C (a,b), 900 °C (c,d), and 1100 °C (e,f) (Scale bars for (a–f), respectively: 1 μm, 200 nm, 500 nm, 100 nm, 1 μm, and 100 nm).

diameter distribution (although some pores are still formed). Beginning in Fig. 3.3c,d, no surface salts or salt pockets are present, and instead there is a hierarchically porous texture. Pores observable from SEM have diameters between 26 nm or higher, down to an observable 6 nm, which is the lowest feature size observable from the SEM images. From this data, it is confirmed that this material becomes mesoporous upon pyrolysis, with pore sizes of 6–26 nm observable by SEM. Images in Fig. 3.3e,f, representing the 1100CSTs, display an even wider range of porosity than the 900CSTs, with macropores of up to 100 nm in diameter. To confirm that porosity exists throughout the bulk of the nanoribbons, rather than solely on the surface, cross-sections of the nanoribbons were captured under SEM, shown in Fig. 3.3d,f. In these images, the presence of pores is evident throughout the entire thickness of the nanoribbons.

Detailed transmission electron microscopy (TEM) analysis was also conducted on the 1100CSTs, since they were both the highest performing anode material, and displayed the highest apparent porosity from SEM. The microstructure seen in the lower-magnification images (Fig. 3.4a,b) is consistent with what is seen in SEM, which is a thin, highly mesoporous nanoribbon architecture. The range of pore size is confirmed from Fig. 3.4b,d,f identifying macropores and mesopores. Remarkably, TEM analysis also confirms the presence of worm or channel-shaped micropores, as observed in Fig. 3.4f. The low thickness of the ribbon is observed from the transparency of the structure in Fig. 3.4a, wherein the lacey carbon from the TEM grid is visible from beneath the sample. The general shape of the meso- and macropores of the nanoribbons is circular, information which supports the idea that salt pocket formation, and subsequent melting induces this type of void space generation. On the other

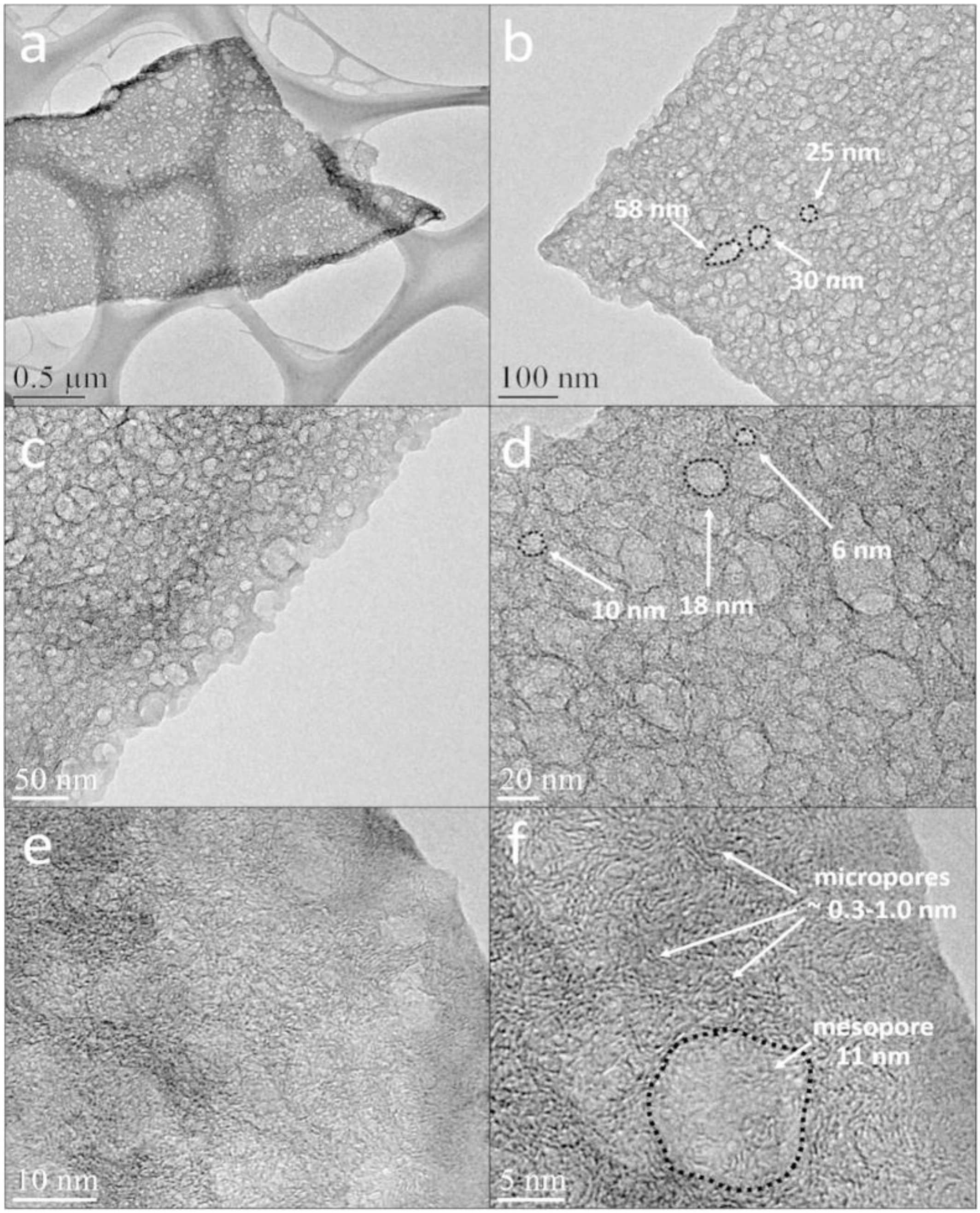

Figure 3.4: TEM of pristine PM 1100CST hierarchically porous nanoribbons, showing macroporosity (a,b), mesoporosity (c,d) and worm-like microporosity (e,f).

hand, it is hypothesized that the worm-like micropores captured in Fig. 3.4f are generated through an activation-like process. N_2adsorption/desorption isotherms show a long, flat plateau for adsorption and desorption, and a significant hysteresis (a characteristic of mesoporous and/or microporous carbons). The BET surface area was measured at 19.6 m^2/g, which is a discrepancy in relation to the isotherm and TEM data; this points the prevalence of "blind," or inaccessible pores formed in the 1100CSTs, which then become accessed after deep cycling. Moreover, our leading hypothesis is that oxygenated organics (polysaccharides, oligosaccharides, amino acids, DNA), combined with the unusually high K concentration, may lead to carbonate formation, and subsequent CO_2 generation; this is that basis of chemical activation, or a similar mechanism.

The phenomenon of small, biological salt pockets causing void spaces of various sizes, from the macroporous to microporous domains, leads us to propose that high PT-pyrolyzed PM CSTs are inherently a self-activating material, by a complex set of mechanisms. It is highly advantageous to have a material that can be naturally primed for optimal performance by simply applying heat-treatment. At PT of 1100 °C, macropores form, facilitating electrolyte infiltration and hence electrolyte interaction with high surface-area hard carbon (shown to be higher capacity than graphite, gravimetrically)[7]. Mesoporous carbons have been shown to perform with excellent stability over long-cycling in literature[8], however, harsh chemical methods are required to achieve such performance. Hierarchically porous carbons, also achieved by many activation methods, tend to improve ion diffusion rates, and expose additional active material for reversible capacity enhancement[9,10].

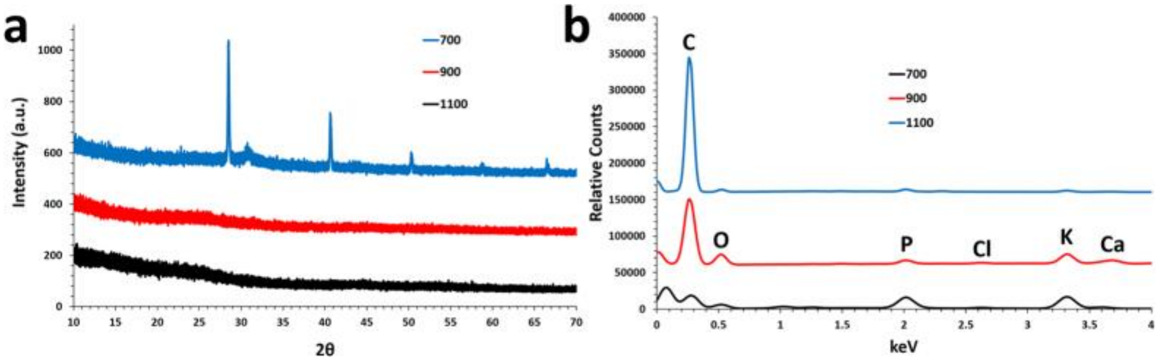

Figure 3.5: Spectral data of the pristine, free-standing PM CSTs at various PTs, including XRD (a) and point-ID EDS (b).

Spectral data was obtained from the PM CSTs after PTs of 700–1100 °C to analyze elemental composition by point-ID energy dispersive x-ray spectroscopy (EDS), and phase information using x-ray diffractometry (XRD) of the free-standing anodes. From Fig. 3.5a, XRD patterns show the transition from large KCl peaks for the 700CSTs (blue), to the 1100CSTs (black) with no visible peaks of crystalline inorganics. The prevailing model for KOH-activation is shown in Eqn. (1) and (2). At temperatures above 400 °C Eqn. (1) occurs, and above 700 °C Eqn. (2) occurs (gasification of CO_2 occurs throughout this process)[10]. Further, K_2O from Eqn. (2) continues to be reduced by carbon to metallic K at above 700 °C. A physical means of activation then occurs, when metallic K diffuses into carbon, expanding the lattice[10]. Considering the classical chemical

$$6KOH + 2C \rightarrow 2K + 3H_2 + 2K_2CO_3 \qquad (1)$$

$$K_2CO_3 \rightarrow K_2O + CO_2 \qquad (2)$$

and physical models for KOH-activation, it is likely that the biological salts present in the PM provide suitable precursors for similar activation mechanisms. With salt deposits of various sizes composed of KCl, and likely a host of carbonates and phosphates, the PM is an ideal self-activating carbon precursor for PTs above 900 °C.

The EDS spectrum is included in Fig. 3.5b, which clearly shows the diminishing metal salts as the PT increases from 700–1100 °C. The free-standing electrodes which result from pyrolysis are used as-synthesized for electrochemical characterization. Naturally, as the wt.% of heteroatoms and inorganic material is reduced in the electrodes, the specific cycling capacity increases. Although EDS results vary slightly from sample to sample (since no two biological specimens are compositionally precisely the same), an average of ~50 wt.% carbon was found in 700CSTs, ~70 wt.% carbon in 900CSTs, and ~90 wt.% carbon in 1100CSTs. While a main mode of oxygen reduction is through gasification and formation of CO_2, an additional mode is thought to be the melting of inorganics and salts. To observe any differences in battery performance on the carbon anodes due to surface functionalization, some 1100CSTs were submerged in a KOH bath for several hours at 80 °C before electrochemical characterization, and denoted as "KOH1100CST."

3.4 Discussion

The specific capacity increase from 700CSTs to 1100CSTs is both due to carbon purification from high PT, and from the proposed natural self-activation, allowing for increased electrolyte infiltration and utilization of active mass. The specific capacities of each sample increases over time, suggesting that the initially unexposed meso- and micropores become more accessible after repeated cycling. It should be specifically noted that the capacity of the 1100CSTs and KOH1100CSTs begin to converge near the 270th cycle. The large difference in discharge capacity between 1100CSTs and KOH1100CSTs from cycle number 1 and 60 may be attributed to initial improved wetting from surface functionalization with hydroxyl and/or carboxyl functional groups. In the long-term, the full capacity may not be significantly affected by these surface groups; in fact, after 500 cycles the non-KOH-wetted 1100CSTs achieve significantly higher capacity at a higher rate. While all four PM CSTs exhibit a very gradual increase in capacity over time, the 1100CSTs maintain the steepest incline.

As previously explained, there are likely[11] multiple modes of action by which this hard carbon-like material becomes activated. A complex mixture of salts, including KCl, NaCl, and likely phosphates[12], coupled with organics their respective heteroatoms, is undergoing reactions above 700 °C that induce CO2 gasification, as well as metallic K diffusion and carbon lattice expansion. Most interestingly, the more pronounced capacity incline of the 1100CSTs and KOH1100CSTs strongly indicates that the micropores are becoming more accessible to the electrolyte with each subsequent oxidation/reduction reaction of the anode (reactions which initially are taking place at the electrode surface). As the micropores become more accessible to the electrolyte, the effective specific active mass increases, therefore increasing the specific capacity over time. Figure 3.6a shows that by the 700th cycle, 700CSTs, 900CSTs, respective heteroatoms, is undergoing reactions above 700 °C that induce CO2 gasification, as well as metallic K diffusion and carbon

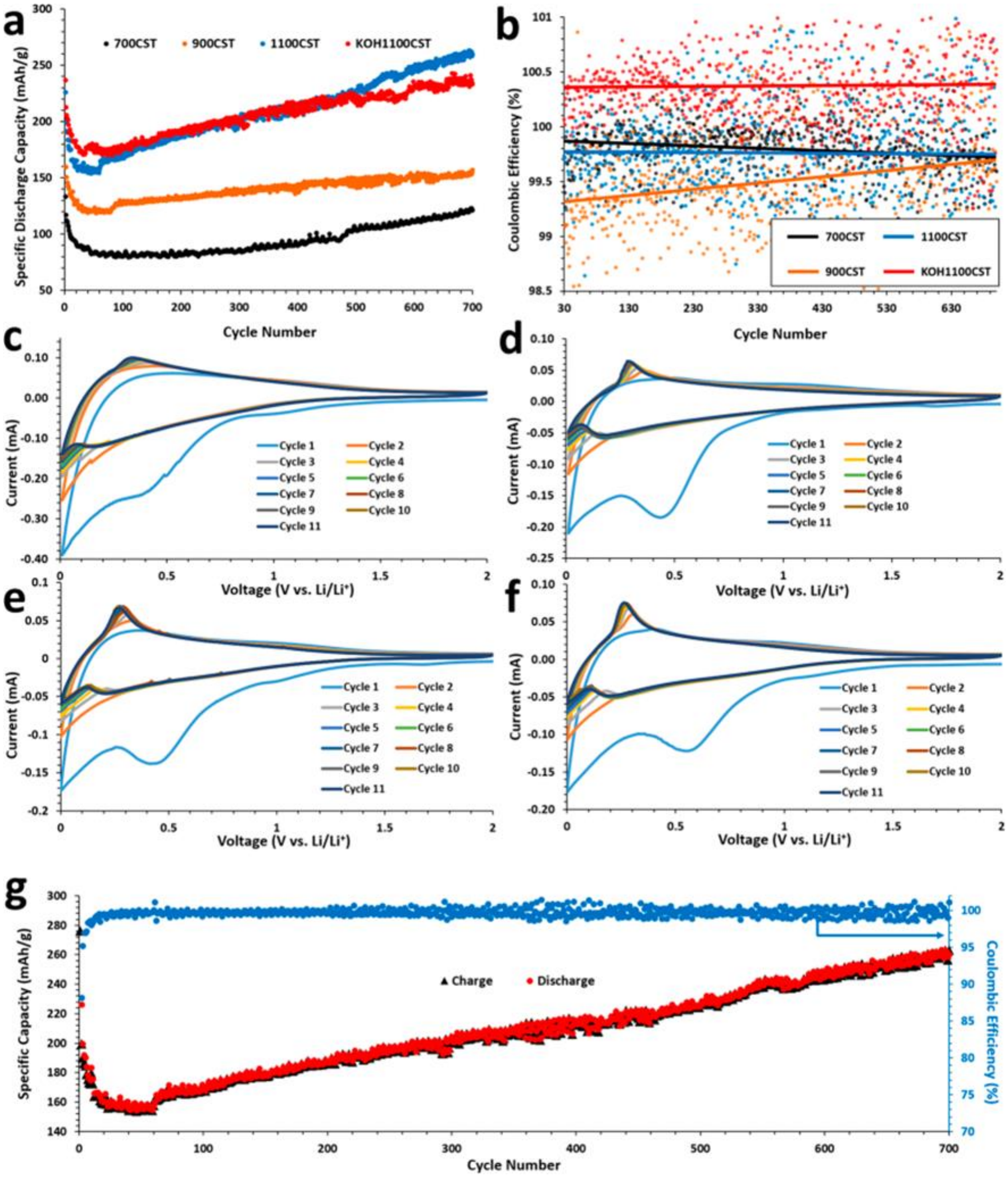

Figure 3.6: Electrochemical performance data of PM CSTs, including discharge plots (a), Coulombic efficiency plots (b), CV curves from cycles 1–11 for 700CST (c), 900CST (d), 1100CST (e), and KOH1100CST (f), and finally the charge/discharge plot with corresponding Coulombic efficiency for 1100CST (g).

lattice expansion. Most interestingly, the more pronounced capacity incline of the 1100CSTs and KOH1100CSTs strongly indicates that the micropores are becoming more accessible to the electrolyte with each subsequent oxidation/reduction reaction of the anode (reactions which initially are taking place at the electrode surface). As the micropores become more accessible to the electrolyte, the effective specific active mass increases, therefore increasing the specific capacity over time. Figure 3.6a_shows that by the 700th cycle, 700CSTs, 900CSTs, 1100CSTs, and KOH1100CSTs exhibit 121.6 mAh/g, 157.5 mAh/g, 233.8 mAh/g, and 260.1 mAh/g, respectively. Therefore, a capacity increase of over 138 mAh/g from PT 700–1100 °C is achieved for the free-standing carbon anodes, with the 1100CSTs outperforming the KOH1100CSTs for more than half the current life of the battery. If calculated based on the approximate wt.% of carbon in the 1100CST cathode, the specific discharge capacity is 289 mAh/g, which is expected to increase to beyond 300 mAh/g at its current rate of capacity increase. The first discharge/charge cycle for this experiment was run at a rate of C/10, while all subsequent cycles were run at C/5, based on a theoretical limit of 500 mAh/g. The initial discharge capacity (out of range for Fig. 3.6a,g) for 700CSTs, 900CSTs, 1100CSTs, and KOH1100CSTs are 429.6 mAh/g, 617.8 mAh/g, 771.3 mAh/g, and 630.9 mAh/g, respectively. A relatively large irreversible initial capacity loss is exhibited for each of the PM CSTs, which is highly characteristic of hard carbon structures.

The Coulombic efficiency (CE) plots of all PM CSTs are shown in Fig. 3.6b, including the KOH1100CSTs (linear trend lines shown in their respective colors for distinction). Contrary to what was expected, the 700CSTs actually demonstrated the

2nd highest overall CE, achieving higher than both the 1100CSTs and 900CSTs. The higher CE in 700CSTs may explained in two parts: a) the samples, with the exception of the KOH1100CSTs, were unwashed before placing in coin cells, and b) the electrolyte has relatively low access to the carbon-protected salts that are, below 900 °C, still trapped in pockets. Since the 900CSTs and 1100CSTs have exposed the majority of the salts, and were also unwashed, the CE may be adversely affected by the electrolyte interaction with any residual salts. Overall, the average CE between cycles 30 and 700 for 700CSTs, 900CSTs, 1100CSTs, and KOH1100CSTs are 99.79, 99.51, 99.75 and 100.37%, respectively.

Cyclic voltammetry (CV) was performed on the PM CSTs at PTs from 700–1100 °C, including the KOH1100CSTs, for 11 cycles. The scanning rate used for all CV measurements was 0.1 mV/s. For each of the curves in Fig. 3.6c–f, the peak in the initial cycle at ~0.5 V is indicative of the solid-electrolyte interphase (SEI) layer formation. This reaction stabilizes relatively quickly with the 2nd cycle and subsequent cycles at around 0.2 V. The 700CST shows a less pronounced SEI formation peak compared to the higher PT samples, which corresponds well with the smaller irreversible capacity loss from the 1st cycle. During charging, each PM CST exhibits a delithiation peak for cycles 2–11 at about 0.3 V. This peak is much more pronounced after PTs above 900 °C; the current increases with each subsequent cycle.

Voltage profiles were obtained from charge/discharge cycling data for cycles 1, 10 and 50, for all PM CST anodes. Voltage profiles are shown for 700CST, 900CST, 1100CST, and KOH1100CST in Fig. 3.7a–d, respectively. As the PT of the PM CSTs

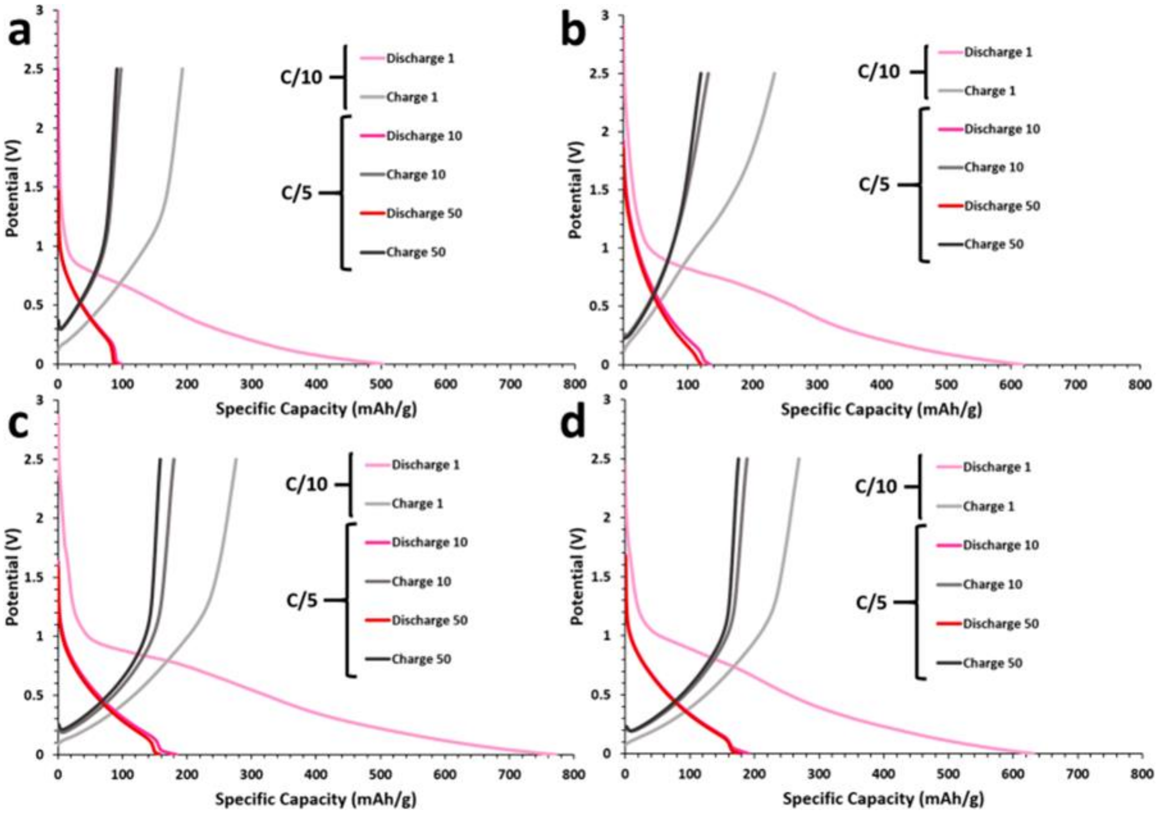

Figure 3.7: Voltage profiles of cycles 1, 10 and 50, for PM CSTs, including 700CST (a), 900CST (b), 1100CST (c), and KOH1100CST (d).

increases, the voltage plateau extends upon each step, as in between 700–900 °C and 900–1100 °C. The exception is the initial cycle, shown to actually decrease after KOH-wetting (Fig. 3.7c,d). The voltage plateaus of PM CSTs agree well with their respective CV measurements, with the operating voltage up to about 1.5 V.

3.5 Conclusion

In conclusion, a novel free-standing, binder-free, additive-free carbon anode was synthesized via pyrolysis at various temperatures, with cap skin tissue (CST) from mature *A. bisporus* (Portobello mushroom (PM)) as the precursor. The resulting morphology of the PM CST anodes, above PT of 900 °C, is an interconnected network of hierarchically porous carbon nanoribbons. The electrochemical behaviour of PM CSTs vs. lithium was studied, exhibiting advanced performance as a free-standing anode for 700 cycles. Structural characterization by SEM indicates the PM CSTs treated at or above 900 °C become hierarchically porous, with a continuous increase in specific capacity, thus leading to the proposal that the material is self-activating due to its unusually high concentration of natural K. The performance of the PM CSTs heated to 1100 °C was also analyzed after wetting with a high-concentration KOH bath. While wetting improved the capacity for the first 50 or so cycles, it became fairly negligible in later cycles compared to the non-wetted 1100CSTs. This work will lead to new explorations into free-standing biomass-derived hierarchically porous materials for energy storage that are high-performance, extremely cheap, and environmentally benign.

3.6 Methods

Typical experiments entailed the following: organic PMs were purchased from local markets and cleaned with DI H_2O. The CSTs were peeled from the caps of the PMs and set aside. Razor blades were then used to slice the CSTs into quartered sections. Using a 15 mm hole punch, disk-shaped samples were obtained from CSTs. All samples were placed on silicon wafer substrates, and dried overnight at 80 °C in a vacuum oven. Before transferring the dried samples to a high-temperature tube furnace, an additional silicon wafer was placed on top of the samples to keep them relatively flat during heat-treatment.

At 700 Torr, Ar gas was flowed at 300 sccm while the temperature was ramped from room temperature to 500 °C over 60 minutes, and held for 5 hours. After slowly cooling to room temperature, the samples were exposed to an additional pyrolysis at either 700 (700CST), 900 (900CST), or 1100 °C (1100CST) (ramping at approximately 10 °C/min.). Once again, the temperature was then held constant for 2 hours. After cooling, the samples were placed directly into coin cell batteries for testing. Since the 1100CSTs performed the best out of the pristine samples, some of these samples were soaked in a 6M KOH solution for 10 hours at 70 °C (KOH1100CST) which were tested in batteries as well.

CR2032-type coin cells were fabricated with the as-synthesized PM CSTs as the working electrodes, microporous polypropylene as the separator (Celgard 2300), and lithium metal foil as the counter electrode. The electrolyte used was 1M $LiPF_6$ in a 1:1 v/v EC/DMC solvent system, with 2 wt.% VC as an additive. All batteries were prepared in an Ar-filled VAC Omni-lab glovebox, and were tested vs. lithium from 0.01 to 3 V on an Arbin BT2000. CV data was collected using a Bio-logic VMP3 with a scan rate of 0.1 mV/s. The masses of the free-standing electrodes used for cycling performance characterization of 700CSTs, 900CSTs, 1100CSTs and KOH1100CSTs were 1.7 mg, 1.2 mg, 1.0 mg, and 0.5 mg, respectively. Scanning electron microscopy, and energy-dispersive X-ray spectroscopy characterization was performed using an FEI Nova Nano450SEM.

References

1. Endo M., Kim C., Nishimura K., Fujino T. & Miyashita K. Recent development of carbon materials for Li ion batteries. Carbon **38**, 183–197 (2000).

2. Buiel E. & Dahn J. R. Li-insertion in hard carbon anode materials for Li-ion batteries.Electrochim. Acta **45** 121–130 (1999).

3. Romanos J. et al. Nanospace engineering of KOH activated carbon. Nanotechnology **23**, 015401 (2012). [PubMed]

4. Lv Y. et al. A comprehensive study on KOH activation of ordered mesoporous carbons and their supercapacitor application. J. Mater. Chem. **22**, 93–99 (2012).

5. Hwang Y. J., Jeong S. K., Nahm K. S., Shin J. S. & Stephan A. M. Pyrolytic carbon derived from coffee shells as anode materials for lithium batteries. J. Phys. Chem. Solids **68**, 182–188 (2007).

6. Han S., Jung D., Jeong J. & Oh E. Effect of pyrolysis temperature on carbon obtained from green tea biomass for superior lithium ion battery anodes. Chem. Eng. J. **254**, 597–604 (2014).

7. Zheng H., Qu Q., Zhang L., Liu G. & Battaglia V. S. Hard carbon: a promising lithium-ion battery anode for high temperature applications with ionic electrolyte. R. Soc. Chem. Adv.**2**, 4904–4912 (2012).

8. Zhang F., Wang K., Li G. & Chen J. Hierarchical porous carbon derived from rice straw for lithium ion batteries with high-rate performance. Electrochem. Commun. **11**, 130–133 (2009).

9. Yi J. et al. Preparation of hierarchical porous carbon and its rate performance as anode of lithium ion battery. J. Power Sources **196**, 6670–6675 (2011).

10. Wang J. & Kaskel S. KOH activation of carbon-based materials for energy storage. J. Mater. Chem. **22**, 23710 (2012).

11. Guo B. et al. Soft-Templated Mesoporous Carbon-Carbon Nanotube Composites for High Performance Lithium-ion Batteries. Adv. Mater. **23**, 4661–4666 (2011). [PubMed]

12. Dobele G. et al. Formation of nanoporous carbon materials in conditions of thermocatalytic synthesis. J. Anal. Appl. Pyrolysis **103**, 173–180 (2013).

Chapter 4

Carbon-Coated, Diatomite-Derived Nanosilicon as a High Rate Capable Li-ion Battery Anode

4.1 Abstract

Silicon is produced in a variety of ways as an ultra-high capacity lithium-ion battery (LIB) anode material. The traditional carbothermic reduction process required is expensive and energy-intensive; in this work, we use an efficient magnesiothermic reduction to convert the silica-based frustules within diatomaceous earth (diatomite, DE) to nanosilicon (nanoSi) for use as LIB anodes. Polyacrylic acid (PAA) was used as a binder for the DE-based nanoSi anodes for the first time, being attributed for the high silicon utilization under high current densities (up to 4C). The resulting nanoSi exhibited a high BET specific surface area of 162.6 $cm^2\ g^{-1}$, compared to a value of 7.3 $cm^2\ g^{-1}$ for the original DE. DE contains SiO_2 architectures that make ideal bio-derived templates for nanoscaled silicon. The DE-based nanoSi anodes exhibit good cyclability, with a specific discharge capacity of 1102.1 mAh g^{-1} after 50 cycles at a C-rate of C/5 (0.7 A g_{Si}^{-1}) and high areal loading (2 mg cm^{-2}). This work also demonstrates the fist rate capability testing for a DE-based Si anode; C-rates of C/30 - 4C were tested. At 4C (14.3 A g_{Si}^{-1}), the anode maintained a specific capacity of 654.3 mAh g^{-1} – nearly 2x higher than graphite's theoretical value (372 mAh g^{-1}).

4.2 Introduction

Magnesiothermic reduction can be used in conjunction with a low-cost and abundant SiO_2 source to produce nanoSi-based Li-ion battery anodes significantly more efficiently. Diatomaceous earth is a friable sedimentary rock (diatomite, DE) which has been deposited over millions of years in aquatic environments, leaving massive deposits of thousands of square acres and thousands of feet deep[1]. It is composed of the deceased, fossilized frustules of diatoms. Diatoms are a diverse group of photosynthetic, single-celled microorganisms that exist as an algae that are responsible for a significant contribution of oxygen (O_2) production in Earth's atmosphere. Their frustules are principally biomineralized as SiO_2, containing amorphous quartz and opaline phases with small amounts of Fe_2O_3 and Al_2O_3 impurities[1-3]. The SiO_2 purity can range in diatomaceous earth, depending on the source, from 75.68 – 96.02 wt.%[1].There are massive diatomite deposits around the world; the United States is the world's greatest producer of natural diatomite, having produced 770 metric tons of diatomite in 2013[4]. Diatomite, therefore, represents an abundant source of high purity SiO_2, and serves as an important potential precursor to silicon (Si).

In order to convert SiO_2 structures and phases into nanoSi made up of extremely small particles (down to nearly 5 nm), a heat scavenging agent may be used in conjunction with magnesiothermic reduction. An excellent heat scavenger is common table salt (NaCl), as seen in the work of Favors, et al[5-7], which has a positive enthalpy of fusion and absorbs a significant amount of the heat produced from the highly exothermic Mg reduction (ΔH =

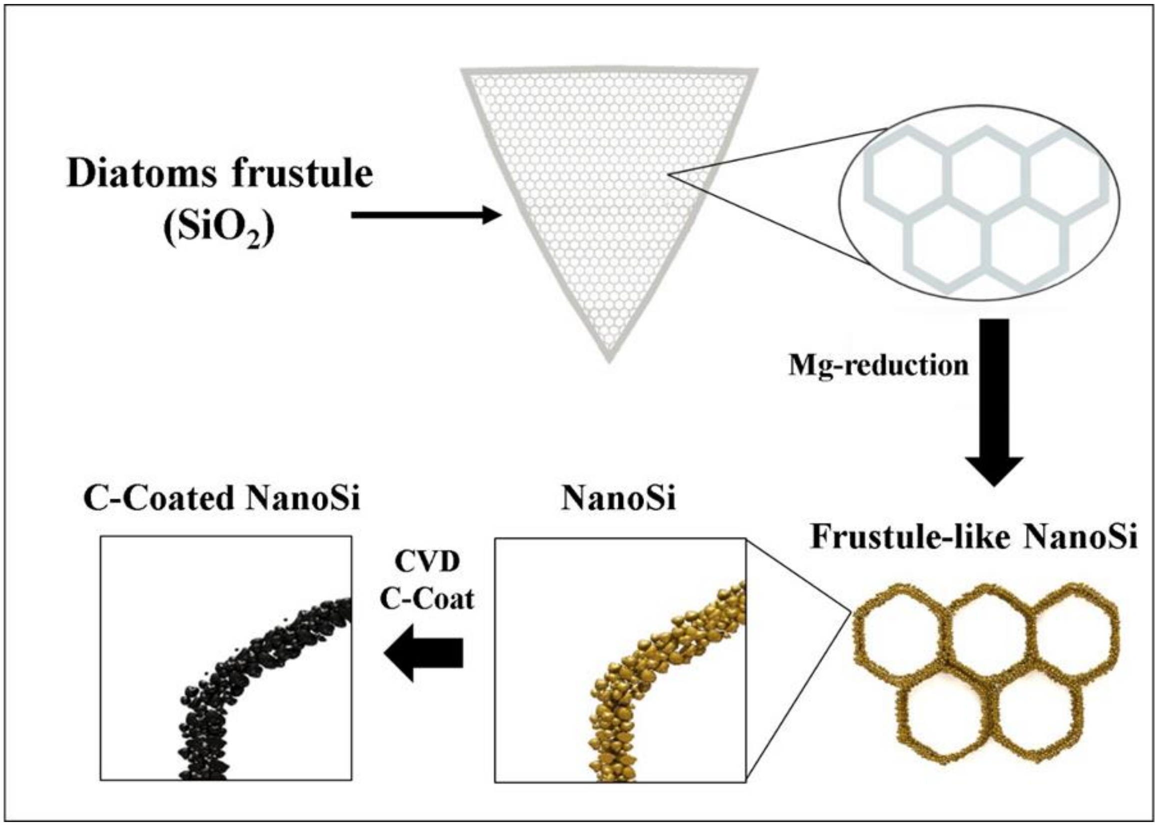

Figure 4.1: Schematic illustration of the process of obtaining C-coated, DE-derived, frustule-like nanoSi structures for use as Li-ion anode active material. Lauro Zavala is credited for the contribution of this artwork.

-586.7 kJ mol_{SiO2}^{-1})[7]. Ultimately, the thermodynamic offset from the endothermic NaCl phase change to liquid prevents local melting of the Si during the reaction. In this work, nanoSi particles were observed after converting purified diatoms frustules to nanoSi using magnesiothermic reduction. In addition, the morphologies of the diatoms frustules were conserved after being converted into elemental Si from the reduction reaction, resulting in nanoSi particle-composed diatom frustule structures. These naturally occurring structures are advantageous for use in Si anodes for lithium-ion (Li-ion) batteries because of the macroporous nature of the frustule structures, which allows easy access for the electrolyte, and the nanoscaled particle size of the nanoSi, which resists pulverization during expansion/contraction upon lithiation/delithiation[8-10]. The straightforward synthesis of C-coated frustule-like nanoSi from DE is depicted in the schematic in Fig. 4.1. Other naturally occurring structures benefit electrode performance, such as in pyrolytic biomass-based electrodes[11]. It is also possible to couple a Si-based electrode with other high-capacity next-generation cathode materials, such as sulfur, which has a theoretical capacity of 1675 mAh g^{-1}, nearly 10x that of lithium cobalt oxide[12]. The highly mesoporous nature of the resulting frustule-like nanoSi, coupled with its macroporous frustule-like architectures, provide an ideal bimodality that can help the structure cope with a massive theoretical volume expansion of 280% upon Li alloying (it should also be noted that experimental evidence shows the expansion could be much greater, upwards of 490%)[13].

4.3 Results

Scanning electron microscopy (SEM) was used to study the structure of the DE as-obtained, as well as after the magnesiothermic reduction. In Fig. 4.2a-c, the morphology and scale of the DE microstructures can be observed. Since DE is composed of an array of diatoms frustules with diverse morphologies, individual frustules with typical structures are noticed in Fig. 4.2a and Fig. 4.2b, with a hexagonal honeycomb architecture and an elongated fence-like architecture, respectively. A lower magnification SEM micrograph captures the true diversity of the frustule structures in Fig. 4.2c. The features in the frustules

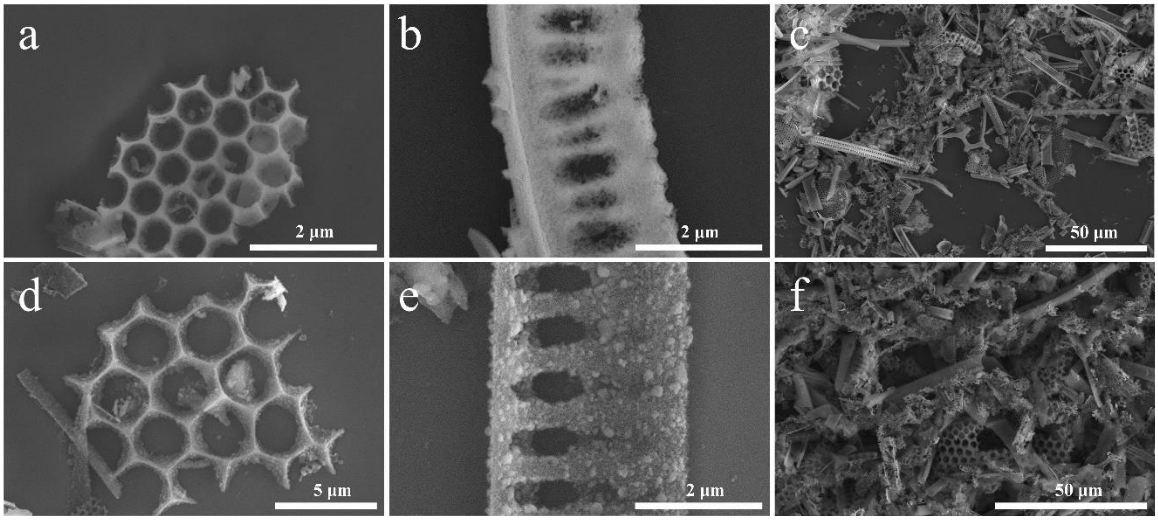

Figure 4.2: SEM characterization of 2 distinct types of DE frustule fragments with unique geometries (a-b), lower-magnification SEM of the powder made up of DE (c), the corresponding geometries of nanoSi structures derived from DE frustules (d-e), and lower magnification SEM of the powder made up of DE-derived nanoSi (f).

vary in shape, size and dimension, and exist in both the nano and microscale. For example, the hexagons of the frustule in Fig. 4.2a average ca. 530 nm, the spacing between the pillars of the frustule in Fig. 4.2b vary from ca. 180 nm to >400 nm, and the pillars themselves are approximately 200 nm in diameter. The overall size of the frustule fragments, however, tend to be on the order of several microns. In addition to the as-obtained DE, the DE-derived post-reduction nanoSi structures were studied using SEM (Fig. 4.2d-f). The structures in Fig. 4.2d-f have also been C-coated via CVD. Post-reduction, the morphologies of the DE frustule fragments are well maintained. Fig. 4.2d shows a hexagonal honeycomb architecture similar to the DE frustule from Fig. 4.2a. The macroporosity (exhibiting voids >50 nm) of the hexagons is preserved along with the structure and morphology of the overall frustule fragment. The same phenomenon is also observed with the elongated fence-like architecture of the DE frustule in Fig. 4.2b, being largely preserved after the reduction as shown in Fig. 4.2e. The diverse array of DE frustule fragments are nearly indistinguishable from the post-reduction frustule-templated nanoSi structures on the microstructure level, as can be seen from Fig. 4.2f. However, the surface morphology of the frustule-shaped nanoSi structures is noticeably different. It is apparent from Fig. 4.2d-e that upon reduction of SiO_2 to Si, the resulting microstructures are ultimately composed of smaller Si particles, giving a rough, spongy appearance.

Analysis of the nanostructure of the DE-derived nanoSi was carried out using high-resolution transmission electron microscopy (HRTEM). Fig. 4.3 gives details of the bare nanoSi, before the CVD C-coating step. Multiple crystals are observed in Fig. 4.3a, for which a selected area electron diffraction pattern (shown as inset in Fig. 4.3a) was also obtained. The ring SAED pattern is consistent with cubic Si structure with rings corresponding to the 111, 220, and 311 reflections, respectively. The higher-magnification HRTEM micrograph in Fig. 4.3b captures the size of smaller Si particles. Additionally, it can be seen that the crystalline Si (identified by lattice fringes) are encapsulated by a native amorphous oxide layer on the surface (no lattice fringes). In this image, the d-spacing was also measured to be 3.12 Å, the characteristic spacing for Si. Fig. 4.3c very clearly shows a larger Si particle with a well-defined amorphous oxide surface layer (FFT shows crystal orientation = [011] for the underlying Si substrate within the particle). This structure is confirmed with a similar particle in Fig. 4.3d, showing elemental mapping by combined

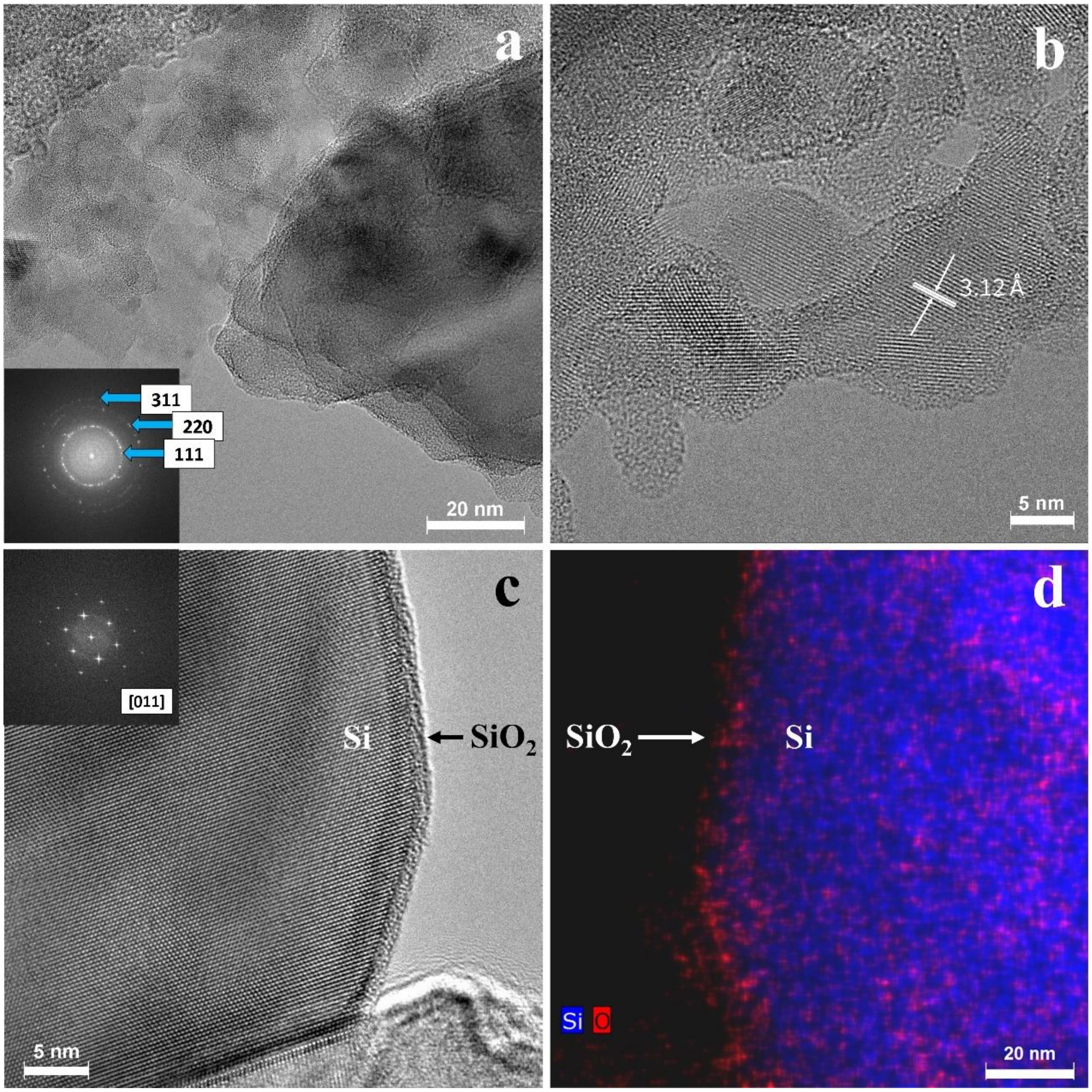

Figure 4.3: HRTEM analysis of bare DE-derived nanoSi, including Si crystals of various orientations and the indexed selected area electron diffraction pattern as an inset (a), select nanoSi particles showing the d-spacing of crystalline Si (b), a select larger Si particle with well-distinguished Si core and amorphous surface layer with FFT inset (c) and a similar larger particle analyzed by dark-field EDX mapping showing the Si core and oxide surface layer (d).

energy-dispersive X-ray spectroscopy (EDX) and high angle annular dark field (HAADF) STEM imaging. With Si highlighted in blue and O in red, a strong elemental distinction can be made between the bulk particle's Si and the SiO_2 making up the surface layer. For the structural stabilization of the Si anode over the first several cycles, and establishing an optimal SEI layer, this oxide layer is critical[14].

Additional TEM characterization was conducted to observe the final nanostructure preservation of the nanoSi after C-coating. Preservation of the overall frustule-like architecture of the nanoSi structures is further confirmed in Fig. 4.4a, where a hexagonal honeycomb arrangement is observed. At this magnification, various pore sizes can also be observed. Macropores (>50 nm) are provided by the inherent honeycomb architecture of the nanoSi structures, and visible mesopores are generated as a result of the magnesiothermic reduction. Fig. 4.4b shows a higher magnification micrograph capturing the inner diameter of a hexagon present in the frustule-like nanoSi structure. In this image, the size of the post-reduction silicon nanoparticles (SiNPs) can be observed, ca. 10s of nanometers. The SiNPs that make up the frustule-like nanoSi structures are well below the critical dimension D_c of ~150 nm, below which Si nanoparticles have a high enough fracture toughness to be able to endure lithiation repeatedly without fracturing[15]. From Fig. 4.4c, the carbon nano-coating can be clearly distinguished from the SiNP, with a thickness ca. 5 nm. The C-coating of the nanoSi is clearly amorphous from the lack of lattice fringes in HRTEM, as also from the low-intensity, broad peak in the powder X-ray diffractometry (XRD) spectrum (Fig. 4.4d).

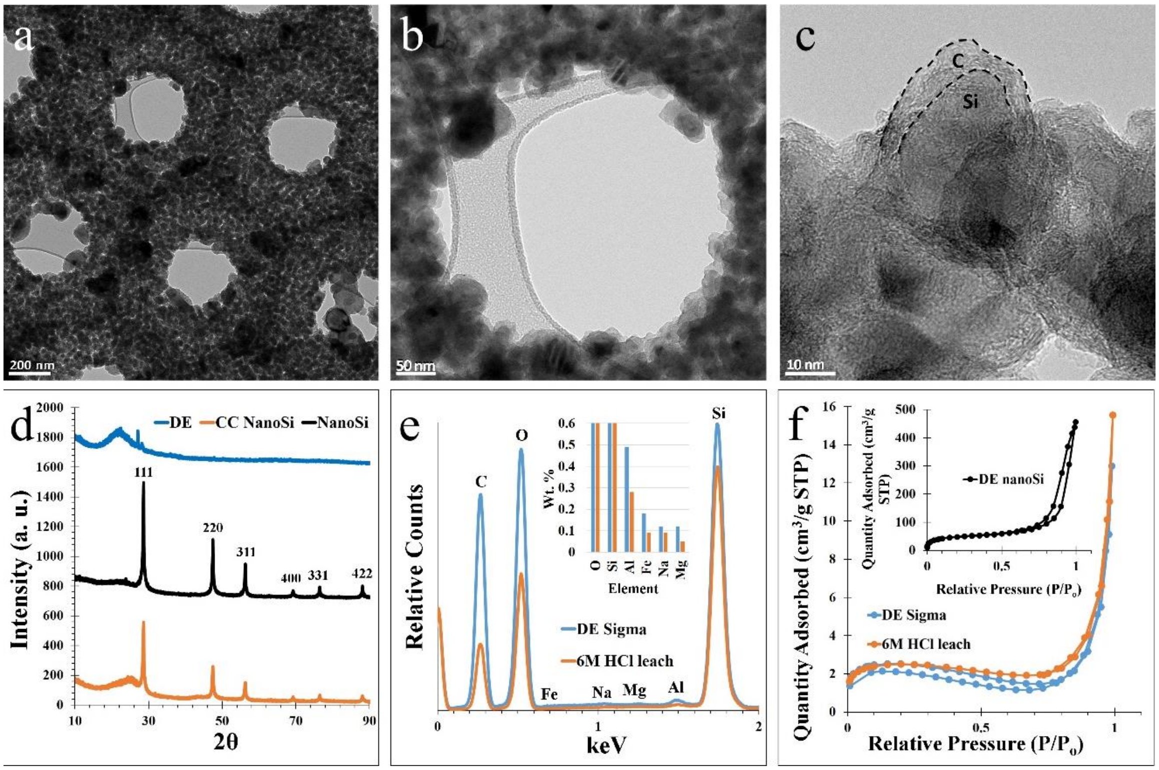

Figure 4.4*:* Low to high magnification TEM characterization of a hexagonal honeycomb-shaped frustule-like nanoSi structure showing the SiNPs (a-c), XRD spectra of DE, nanoSi, and C-coated nanoSi (d), the EDX spectrum and elemental composition of DE before and after HCl leaching (e), and BET N_2 adsorption isotherms of DE before and after purification, and nanoSi (f).

XRD analysis also shows the transformation from the impure biosilica of the DE into nanoSi, and ultimately the C-coated nanoSi structures (shown in blue, black and orange, respectively, in Fig. 4.4d). Here, the (101) plane of DE's quartz phase is identified, as well as a few smaller impurity peaks. After magnesiothermic treatment, the characteristic peaks of nanoSi (corresponding to reflections 111, 220, 311, 400, and 331) are present in both the bare and C-coated nanoSi spectra in Fig. 4.4d. Along with the characteristic nanoSi peaks, there is a relatively small amorphous peak present around 2θ ~24°, indicating a stabilizing native oxide surface layer on the nanoSi particles[16,17]. The C-coated nanoSi spectrum shows the amorphous carbon peak at 2θ ~25, indicating a successful CVD carbon coating. Energy-dispersive X-ray spectroscopy (EDX) allows Fig. 4.4e to show the elemental distribution within the DE powder, as well as the relative wt. % of elements before and after leaching the powder with 6M HCl at 75°C for 12 hours (inset). A significant reduction in unwanted impurities can be seen after the HCl leaching; for example, Al was reduced by roughly 1/3 and Fe was reduced by nearly 1/2 in terms of overall weight. The HCl-leached DE was subsequently used to produce the magnesiothermic reduction product (frustule-like nanoSi) used in the Li-ion battery performance testing. The Brunauer-Emmett-Teller (BET) method was used to obtain pore structure and surface area data on the DE, HCl-leached (purified) DE, and the frustule-like nanoSi (Fig. 4.4f). The nitrogen (N_2) adsorption isotherms reveal that the only material to show mesoporous characteristics is the nanoSi (inset). The hysteresis of the DE indicates a more macroporous structure, and the inset N_2 isotherm demonstrates hysteresis in the mesoporous region upfield of 0.8 P/P_o, which is attributed to capillary condensation in pores between 2 and 50 nm[18,19]. The specific surface area of the as-purchased DE vs. the nanoSi proved to be drastically different; the DE BET surface area was measured at 7.3 $cm^2\ g^{-1}$, while the frustule-like nanoSi powder had a measured BET surface area of 162.6 $cm^2\ g^{-1}$.

4.4 Discussion

Metallurgical Si production is typically an energy-intensive process. The standard process of carbothermic Si production is highly endothermic; it is described by the following reaction:

$$SiO_2 + 2C \rightarrow Si + 2CO \qquad (1)$$

The carbothermic reduction of SiO_2 shown in Eq. 1 requires 12.5 MWh per ton of Si, and temperatures in excess of 1800°C[20,21]. As an alternative method of Si production that requires far less energy input, magnesiothermic reduction has been employed. The overall reaction is described in Eq. 2.

$$SiO_2 + 2Mg \rightarrow Si + 2MgO \qquad (2)$$

This reaction, in contrast to carbothermic reduction, can be carried out at 650-700°C[22-24]. Furthermore, use of Mg as the reducing agent in this reaction tends to lead to the production of interconnected SiNPs rather than bulk Si, making it ideal for producing electrode active material on the nanoscale. The combination of the use of magnesiothermic reduction and the use of diatomite as an abundant, nanostructured SiO_2 feedstock leads to the ability to produce a greener, high-performance Si anode active material for Li-ion batteries. Shen, et al. were apparently the first to demonstrate the fabrication of magnesiothermically-reduced DE into an electroactive anode for Li-ion batteries. They report on the cycling of DE-based

Si anodes for up to 30 charge-discharge cycles, although the capacity fading is drastic (achieving only 633 mAh g^{-1} after 30 cycles) with a current density of 0.2 mA cm^{-2} [8]. Furthermore, Li, et al. conducted more thorough characterization of magnesiothermically-reduced DE, showing 10-20 nm Si crystallites with a native oxide layer for cycling stability. They were able to achieve slightly above 750 mAh g^{-1} after 150 cycles, demonstrating good cycle stability. In their synthesis, they introduced NaCl as a heat scavenger which has also been done in other Mg-reduction nanoSi synthesis strategies[25,5-7]. The use of such a heat scavenger prevents the highly exothermic reaction from approaching the melting point of Si (1414^{o}C). In both examples of DE-based nanoSi as Li-ion battery anode materials, C-coating was employed to enhance the conductivity of the nanoSi structures. Regarding polymer binders, previous works have utilized sodium alginate (NaA) and sodium carboxymethyl cellulose (NaCMC). The mechanical properties of organic polymer binders vary widely; in this work, polyacrylic acid (PAA) was used for the first time for DE-based nanoSi in Li-ion batteries. PAA has been shown to increase the efficiency of Si-based anodes, and due to its high concentration of carboxylic groups may function as a superior binder for Si anodes (this is evidenced by lower swellability in the presence of carbonates compared to CMC, greater contact between PAA and SiO_x/functional groups on the C-coating during lithiation, and Li^+ hopping through the nanoscaled PAA binder)[26,27,5]. The enhanced mechanical properties, such as elasticity, are largely derived from an H-bond network formed between H-bond donors and acceptors between the PAA COOH groups and the surface functional groups of the active material (i.e. SiO_x)[28]. Therefore, in this case, PAA is hypothesized to enhance the rate capability of the DE nanoSi anodes.

50 cycles of charge-discharge cyclability testing at a rate of C/5 based on Si (1C = 3.579 Ah g_{Si}^{-1}), as well as rate capability testing up to rate of 4C over 75 cycles was performed on the anodes. C/5 was chosen as a benchmark cycling rate for the DE-based nanoSi anodes for 50 cycles, because it is theoretically a 5-hour charge and discharge. The initial cycle was run at a rate of C/50 to establish a stable solid-electrolyte interphase (SEI) on the surface of the Si particles. The cycling results can be seen in Fig. 4.5a, where the 2nd cycle (1st at C/5) yielded a specific discharge capacity of 1364.8 mAh g^{-1}, while the 50th cycle maintained a reversible capacity of 1102.1 mAh g^{-1}. A calculation based on these results show that after 50 cycles, >80% capacity retention is preserved. After 50 charge-discharge cycles, the Coulombic efficiency was consistently above 99.9%. The active material areal loading for the C/5 cycling was 2 mg_{Si} cm^{-2}. Fig. 4.5b depicts the rate performance of the DE-based nanoSi anodes, which was again cycled once at C/50 to establish the SEI layer, followed by 10 cycles each at C/30, C/10, C/5, C/2, 1C, 2C, 4C, then back to C/30. The capacity retention of each 10-cycle series for the various C-rates (C/30 – 4C) were 67.4%, 90.4%, 98.3%, 95.0%, 88.4%, 87.1% and 88.7%, respectively. The discharge and charge capacities are shown for each cycle, and directly compared to the theoretical specific capacity of graphite (372 mAh g^{-1}). After 10 cycles of each rate (C/30 – 4C) cycling, the reversible discharge capacity is 1322.3, 1095.5, 1034.1, 971.5, 892.3, 787.3, and 654.3 mAh g^{-1}, respectively. This is extremely good performance

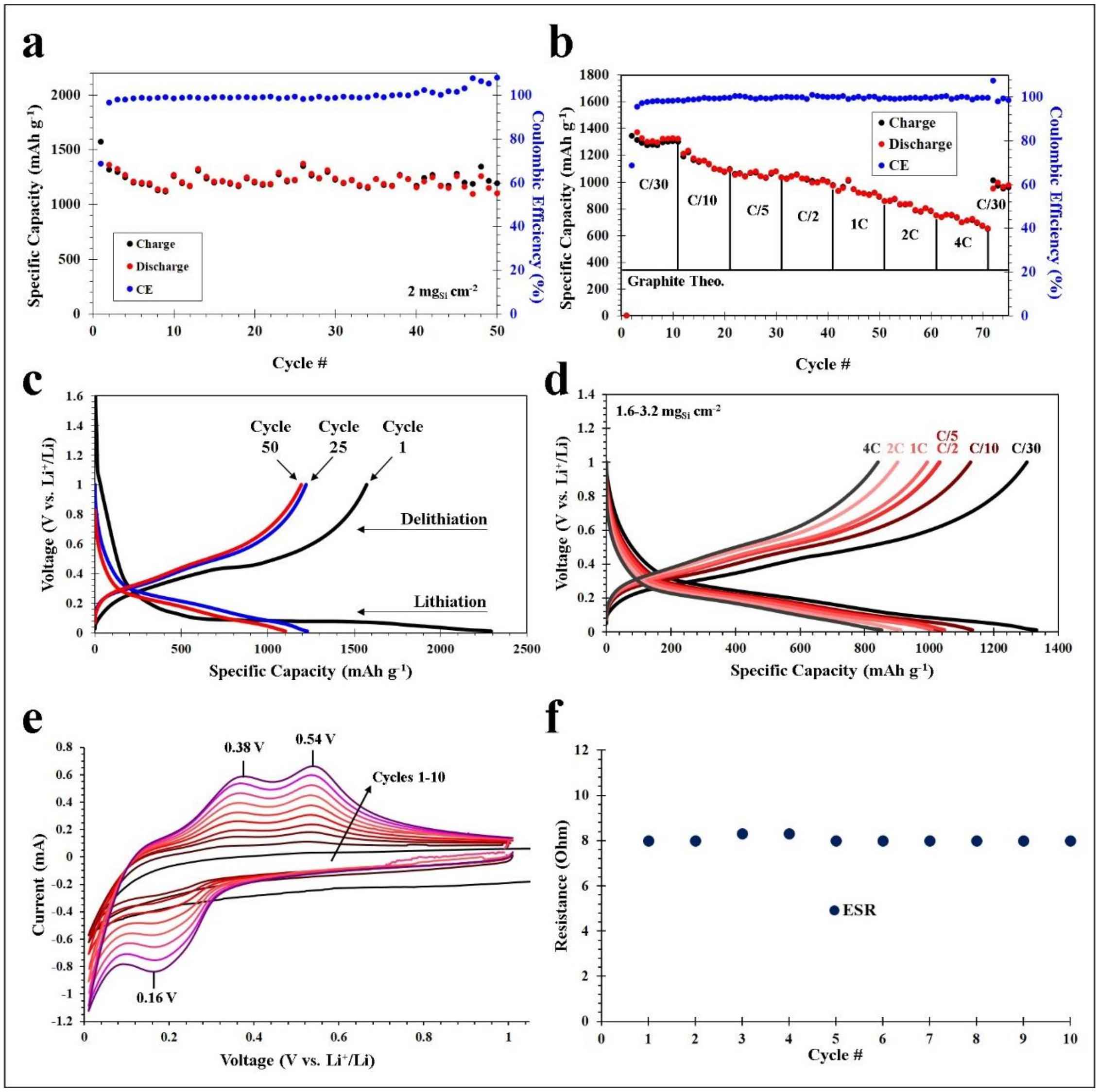

Figure 4.5: Electrochemical characterization of DE-derived nanoSi-based electrodes, including charge-discharge cycling performance for 50 cycles at C/5 based on Si (a), C-rate testing for 75 cycles at C-rates from C/30 – 4C (b), voltage profiling of the charge-discharge data at C/5 for cycles 1, 25 and 50 (c), voltage profiling of various C-rates (d), CV for cycles 1-10 (e) and the ESR values for cycles 1-10 based on EIS analysis (f).

for a Si active material, especially considering the relatively high Si areal loading of 1.6 – 3.2 mg_{Si} cm^{-2} (performance and Si loading was averaged). Other works on Si anodes demonstrate very good rate performance, but with relatively low areal loading (0.3 mg_{Si} cm^{-2}, for example)[29]. The capacity fading is further illustrated through the voltage profiling in Fig. 4.5c-d, where the 1st, 25th and 50th cycles are compared (Fig. 4.5c), and the widening of the voltage plateaus as a function of cycling rate (current density) is apparent (Fig. 4.5d). The plateaus present in the voltage profiles agree well with the CV measurements in Fig. 4.5e, with the highly evident peaks associated with alloying (0.16 V) and dealloying (0.38 V, 0.54 V) in the half-cell.

Extensive EIS analysis was conducted on the DE-derived nanoSi anodes. Fig. 4.6a shows an electrical equivalent circuit (EEC) used for modeling the test electrode by using its electrochemical impedance data. Such data is obtained from electrochemical impedance spectroscopy (EIS), where a small sinusoidal input is overlaid on a DC signal in order to measure linear system response over some frequency range. For the present investigation, we utilized PEIS (potentiostatic EIS) whereby we held the test cell under a fixed voltage while applying a 10 mV sinusoidal input. The resultant impedance data contain critical information about the electrode's internal electrochemistry. The EEC shown in Fig. 4.6 consists of individual lumped circuit elements that serve to isolate some of the electrochemical steps that take place during charging or discharging in the Li-ion battery. This is possible because time constants for these steps are usually

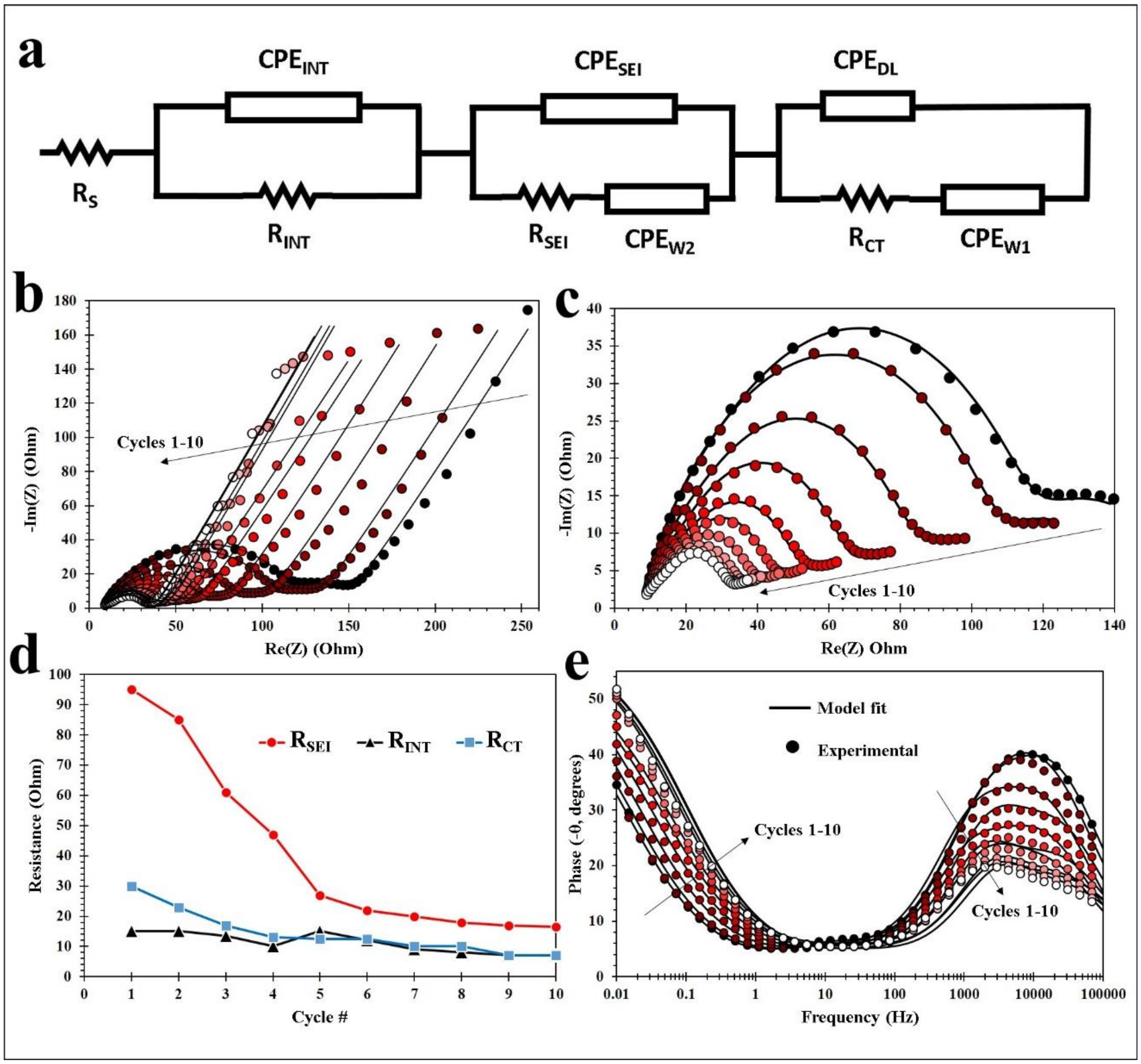

Figure 4.6: EIS analysis of the DE-derived nanoSi electrodes assembled in a Li-ion half cell, including the EEC based on modeled EIS data (a), standard Nyquist plots for 10 cycles including fitted data (b), enlarged semi-circle/high-frequency region of the Nyquist plots (c), SEI resistance, internal impedance and charge transfer resistance data for 10 cycles (d), and Bode plots for 10 cycles including fitted data (e).

distinguishable. R_S is often expressed as equivalent series resistance (ESR), which largely quantifies electrolyte resistance. Fig. 4.5f shows that this value remains relatively constant throughout the first 10 cycles. Conductivity of carbon additives and metallic extensions within the electrode material can also contribute to this resistance. This step is usually the fastest, and therefore information pertaining to it is found at the highest frequency end of impedance spectrum. Z_{INT}, composed of CPE_{INT} and R_{INT}, is the impedance due to imperfect contact within the nanostructured Si electrode. This impedance determines the rate at which electrons travel through the active material, specifically. Constant phase elements, or CPEs, are imperfect capacitances arising from non-ideal spatial distribution of chemical and tactile nature of the interfaces involved. These capacitors are charged and discharged according to governing principles, but their effects are not registered in the DC regime. However, quantizing them improves any EEC-based model of a LIB for the purpose of battery management. The second parallel impedance branch characterizes the SEI. A second constant phase element titled CPE_{W2} is also located in this branch. This latter element quantizes the capacitance due to chemical gradient arising from limited diffusion rates of Li ions in the electrolyte near the electrode surface. CPE_{W1}, a third constant phase element in the third parallel branch, is used to characterize diffusion of Li^+ in the solid state (i.e. electrode material, nanoSi). The third parallel branch also quantizes the capacitive nature of the double layer formed at the electrode-electrolyte interface, denoted as CPE_{DL}. R_{CT} is the rate-limiting element associated with redox reactions taking place during lithiation and delithiation.

EIS analysis demonstrates self-stabilization of the anode during the first 10 cycles. Evolution of resistive behavior of 3 electrochemical steps within our test cell were characterized via R_{INT}, R_{SEI}, and R_{CT} (Fig. 4.6d). R_{CT} decreases as expected during the first 10 cycles. This is due to improving electrochemical conditions for redox reactions over the first few cycles. This stabilizing behavior in R_{CT} gives evidence for good cyclability of the test cell. Evolution of R_{INT} can be characterized into 3 phases by 3 series of cycles: #1-4, 5, then 6-10. The resistance that characterizes the integrity of internal electronic conduction within electrode active material decreases during the first phase (1-4), spikes in the second, then begins to decrease again throughout the third phase. This trend can be explained by a large change in the Si nanostructure at the 5th cycle. This phenomenon at the electrode nanostructure is evidence of the electrode's tendency to self-stabilize. One explanation for the sudden spike in R_{INT} in the 5th cycle is that majority of electrode wetting by electrolyte was completed by this time, and the resultant increase in "total current" through electrode caused the change in its nanostructure we observe on the 5th cycle. One evidence for this hypothesis is that Q_{INT}, which assigns an overall capacitance value to the totality of imperfect contacts within active material nanostructure, decreases comparatively sharply before the 5th cycle. This can be because of increased available surface area for lithiation to occur led to a decreased charge time in the measured capacitance. A drop followed by stabilization in R_{SEI} is essential for any LIB cell with satisfactory lifetime. Trend observed for R_{SEI} over the first 5 cycles also support our theory regarding the completion of our electrode wetting with electrolyte at the 5th cycle. R_{SEI} decreases sharply until the 5th cycle, thereafter decreasing a much slower rate and stabilizing. This agrees with the idea that the

SEI formation process (involving irreversible reactions with Li ions and other reactive species present with impedance significantly larger than that of reversible lithiation) over electrode surface stops at the 5th cycle, when electrolyte wetting also finishes. Fig. 4.6e shows a Bode (phase vs. log-frequency) plot from the impedance data obtained. An important point of note here is the remarkable increase in the phase angle (shown as negative of its actual value) with cycles #1-10. This increase suggests that overall impedance of the cell evolved from that of a Warburg element toward a more non-ideal end (similar to a CPE with an n value increasing from 0.5). The electrochemical nature of the cell's impedance became more distributed spatially at the nanoscale, but its overall impedance (not shown in these figures) decreased by half over the first ten cycles. Fig. 4.6b-c demonstrate the accuracy of the fitting algorithms used. Fig. 4.6c shows the three semicircles corresponding to the three impedance branches highlighted in this analysis. The two higher frequency semicircles are largely overlapping, and the semicircle for double layer impedance is smaller and upfield, predominantly noticeable in cycles 1-2.

4.5 Methods

The experiments were carried out as follows: DE was purchased from Sigma Aldrich (Celpure, 98% SiO_2), and manually milled for 1 hour. DE was then loaded into high-density polyethylene centrifuge tubes, and mixed with 12M HCl, and held at 75°C in a thermostated water bath. After approximately 2 days of HCl leaching, the DE was washed thoroughly with ultrapure H_2O, followed by absolute ethanol (EtOH). The DE was then dried under vacuum at 100^oC, milled, and mixed with NaCl in a weight ratio of 1:10 (DE:NaCl). Ultrapure H_2O and EtOH was added to this mixture, which was then stirred and slowly evaporated on a hot plate at 80^oC. Once the H_2O and EtOH was evaporated, the DE-NaCl mixture was milled and mixed into a vial with Mg metal such that the resulting weight ratio was 1:10:0.9 (DE:NaCl:Mg). This mixture was thoroughly vortexed, and then loaded into a stainless steel Swagelok reactor inside an Ar-filled glovebox. The reactor was sealed, then removed and placed into a tube furnace. The quartz tube was purged with Ar gas, and the temperature was ramped at 5^oC per minute to 700^oC and held for 2 hours. The furnace was then cooled back to r.t., and the crude product was removed from the reactor. To remove impurities, the crude product was mixed with 6M HCl and allowed to react for 24 hours, with occasional stirring. During this time, the purification of nanoSi was apparent from the color change from blackish-brown to light golden brown. Afterwards, the nanoSi was neutralized to pH 7 with several washes with ultrapure H_2O and EtOH. Once it is neutralized, the nanoSi product was dried under vacuum at 80^oC overnight. The nanoSi powder was C-coated in a separate tube furnace under slight vacuum (600 Torr). First, a mixture of Ar and H_2 gas was flowed (100 SCCM each). The temperature was ramped at approximately 35^oC per minute to 950^oC and held for 20 minutes. During this 20 minutes, ethylene gas (C_2H_2) was flowed at 50 SCCM. After the 20 minutes, the C_2H_2 was shut off, and the furnace cooled to r.t. The C-coated nanoSi was mixted with acetylene black (AB) and polyacrylic acid (PAA), using EtOH as the carrier fluid/solvent for slurry-casting the electrodes on copper foil and subsequent electrochemical characterization.

Battery performance testing was conducted in the CR2032 coin cell form factor for all batteries. The cells were fabricated using working electrodes comprised of frustule-like nanoSi active material mixed with AB and PAA, cast onto Cu foil current collectors with EtOH as the carrier fluid. For CV and EIS measurements, the nanoSi:C:PAA mass ratio of the electrodes was 7:2:1, and for the cycling data and C-rate testing, the ratio was 5.5:3.5:1. Microporous polypropylene (PP) was used as the separator (Celgard 2300), and Li metal foil was used as the counter electrode. The electrolyte used was 1M $LiPF_6$ in a 1:1 v/v FEC/DMC solvent system for all batteries. All cells were fabricated inside an Ar-filled glovebox (VAC Omni-lab). For charge-discharge cycling data and C-rate testing, the cells were cycled from 0.01 to 1 V on an Arbin BT2000. The CV and EIS data was collected on a Bio-logic VMP3 tester. For CV, a scan rate of 0.1 mV/s was used, and EIS was performed initially from open circuit voltage (E_{OC}) and subsequently scanned from 0.1 Hz to 1 MHz after each CV cycle. SEM and point-ID EDX characterization was done using an FEI NovaNanoSEM 450 with an accelerating voltage of 5 kV for the DE powders, and 15 kV for the C-coated nanoSi structures. All TEM/STEM analysis (and corresponding EDX mapping) in Fig. 4.3 was conducted at 300 kV accelerating voltage using an FEI Titan Themis system, equipped with an FEI SuperX energy dispersive spectrometer. TEM in Fig. 4.4 was conducted using an FEI Tecnai12 system. Powder XRD analysis was carried out using a PANalytical Empyrean with Cu -Kα standard radiation.

References

1. Calvert, R. Diatomaceous Earth. J. Chem. Educ. **7**, 2829-2849 (1930).

2. Tsai, W., Lai, C. & Hsien, K. Characterization and adsorption properties of diatomaceous earth modified by hydrofluoric acid etching. J. Colloid Interface Sci. **297**, 749-754 (2006).

3. San, O., Goren, R. & Ozgur, C. Purification of diatomite powder by acid leaching for use in fabrication of porous ceramics. Int. J. Miner. Process. **93**, 6-10 (2009).

4. Crangle, Jr., R. D. Diatomite –U. S. Geological Survey, Mineral Commodities Summaries, February 2014. (2014) Avaliable at: http://minerals.usgs.gov/minerals/pubs/commodity/diatomite/mcs-2014-diato.pdf. (Accessed: 27th February 2016)

5. Favors, Z. et al. Scalable synthesis of nano-silicon from beach sand for long cycle life li-ion batteries. Sci. Rep. **4**, 5623 (2014).

6. Wu, L. et al. Three-dimensional graphene nanosheets loaded with Si nanoparticles by in situ reduction of SiO_2 for lithium ion batteries. Electrochim. Acta **190**, 628-635 (2016).

7. Luo, W. et al. Efficient fabrication of nanoporous Si and Si/Ge enabled by a heat scavenger in magnesiothermic reactions. Sci. Rep. **3**, 2222 (2013).

8. Shen, L., Guo, X., Fang, X., Wang, Z. & Chen, L. Magnesiothermically reduced diatomaceous earth as a porous silicon anode material for lithium ion batteries. J. Power Sources **213**, 229-232 (2012).

9. Liu, J., Kopold, P., van Aken, P. A., Maier, J. & Yu, Y. Energy storage materials from nature through nanotechnology: a sustainable route from reed plants to a silicon anode for lithium-ion batteries. Angew. Chem. **127**, 9768-9772 (2015).

10. Liu, N., Huo, K., McDowell, M. T., Zhao, J. & Cui, Y. Rice husks as a sustainable source of nanostructured silicon for high performance li-ion battery anodes. Sci. Rep. **3**, 1919 (2013).

11. Campbell, B., Ionescu, R., Favors, Z., Ozkan, C. S. & Ozkan, M. Bio-derived, binderless, hierarchically porous carbon anodes for Li-ion batteries. Sci. Rep. **5**, 14575 (2015).

12. Campbell, B. et al. SiO_2-coated sulfur particles with mildly reduced graphene oxide as a cathode material for lithium-sulfur batteries. Nanoscale **7**, 7051-7055 (2015).

13. Nishikawa, K., Moon, J. & Kanamura, K. In-situ observation of volume expansion behavior of a silicon particle in various electrolytes. J. Power Sources **302**, 46-52 (2016).

14. Zhao, H. et al. Conductive Polymer Binder for High-Tap-Density Nanosilicon Material for Lithium-Ion Battery Negative Electrode Application. Nano Lett. **15**, 7927-7932 (2015).

15. Liu, X. H. et al. Size-Dependent Fracture of Silicon Nanoparticles During Lithiation. ACS Nano **6**, 1522-1531 (2012).

16. Favors, Z. et al. Towards scalable binderless electrodes: carbon coated silicon nanofiber paper via Mg reduction of electrospun SiO_2 nanofibers. Sci. Rep. **5**, 8246 (2015).

17. Hassan, F. M., Chabot, V., Elsayed, A. R., Xiao, X. & Chen, Z. Engineered Si electrode nanoarchitecture: a scalable postfabrication treatment for the production of next-generation li-ion batteries. Nano Lett. **14**, 277-283 (2014).

18. Machado, A. E. H. et al. Applications of mesoporous ordered semiconductor materials – case study of TiO_2. Solar Radiation Applications, In-Tech **5**, 87-118 (2015).

19. Gor, G. Y. et al. Elastic response of mesoporous silicon to capillary pressures in the pores. Appl. Phys. Lett. **106**, 261901 (2015).

20. Loutzenhiser, P. G., Tuerk, O. & Steinfeld, A. Production of Si by vacuum carbothermic reduction of SiO_2 using concentrated solar energy. JOM **62**, 49-54 (2010).

21. Nagamori, M., Malinsky, I. & Claveau, A. Thermodynamics of the Si-C-O system for the production of silicon carbide and metallic silicon. Metall. Trans. *B* **17**, 503-514 (1986).

22. Ma, B. et al. Investigation on a magnesiothermic reduction process for preparation of nanocrystalline silicon thin film. Surface Eng. DOI: 10.1080/02670844.2016.1146443 (2016).

23. Liu, X. et al. Scalable synthesis of Si nanostructures by low-temperature magnesiothermic reduction of silica for application in lithium ion batteries. Nano Energy **4**, 31-38 (2014).

24. Zhu, S. et al. Controlled fabrication of Si nanoparticles on graphene sheets for Li-ion batteries. RSC Adv. **3**, 6141 (2013).

25. Li, X. et al. A stable nanoporous silicon anode prepared by modified magnesiothermic reactions. Nano Energy **20**, 68-75 (2016).

26. Magasinski, A. et al. Toward efficient binders for Li-ion battery Si-based anodes: polyacrylic acid. ACS Appl. Mater. Interfaces **2**, 3004-3010 (2010).

27. Erk, C., Brezesinski, T., Sommer, H., Schneider, R. & Janek, J. Toward silicon anodes for next-generation lithium ion batteries: a comparative performance study of various polymer binders and silicon nanopowders. ACS Appl. Mater. Interfaces **5**, 7299-7307 (2013).

28. Delpeuch, N. et al. Critical Role of Silicon Nanoparticles Surface on Lithium Cell Electrochemical Performance Analyzed by FTIR, Raman, EELS, XPS, NMR, and BDS Spectroscopies. J. Phys. Chem. C **118**, 17318-17331 (2014).

29. Jeong, Y. K. et al. Millipede-inspired structural design principle for high performance polysaccharide binders in silicon anodes. Energy Environ. Sci. **8**, 1224 (2015).

Chapter 5

Towards Organosulfur Copolymers for Li-S Cathodes

5.1 Introduction

Here, we have developed a randomized, organosulfur polymeric product through reacting molten sulfur with aromatic alkynes (specifically 1,3-diethynylbenzene (1,3-DEB). The focus of this work was to optimize the synthesis of this material, and ascertain its effectiveness as an active material in lithium-sulfur (Li-S) battery cathodes. While the battery testing stage has yet to be reached, the following describes findings in the way of material synthesis and characterization. Inverse vulcanization, the process of coupling organic reagents with molten sulfur, has been used for more than a century to produce rubber-like materials such as automobile tires[1]. This particular synthesis entails heating elemental sulfur to between 120-160^{o}C (here, optimized at 130^{o}C), then injecting the liquid 1,3-DEB precursor; this is a very new, but similar sulfur-organic material combination compared to literature materials and methods[2-4]. The reaction is exothermic, and is dangerous to carry out in open air, and thus 1,3-DEB is added dropwise while stirring molten sulfur (the synthesis, in the work, was intended to be done in open air in lieu of inert atmosphere in the interest of green processing). A typical reaction takes ~10 minutes, and the resulting product is a dark orange, slightly transparent vitreous solid (introducing anywhere from 5-30 wt.% 1,3-DEB). As more DEB is added, the resulting product becomes darker and less opaque, as seen in Fig. 5.1.

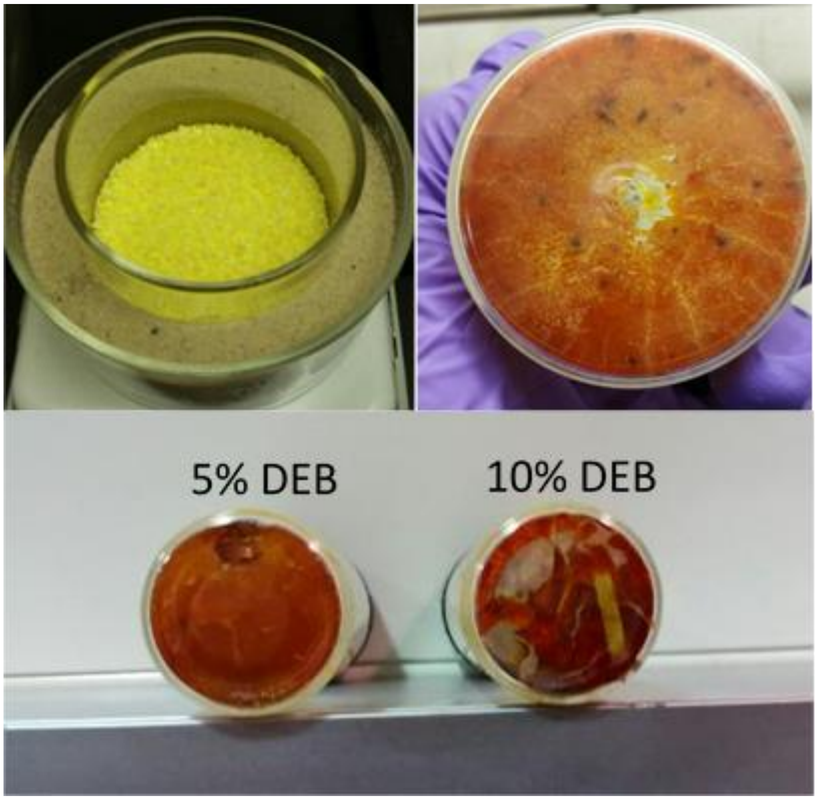

Figure 5.1: Pure sulfur (upper left), poly(S-r-DEB) (upper right), and copolymer with different wt.% DEB added.

The motivation behind organosulfuric-polymeric Li-S cathode materials is the physical advantages they may provide over the traditional elemental sulfur. For example, the resulting copolymer (poly(S-*r*-DEB)) has a much higher melting point than sulfur (>180°C compared to 115°C). As typical Li-S configurations have difficulty operating at higher temperatures for this reason, this new material may serve as a significant improvement in the overall system. Moreover, alkynes increase the melting point whereas alkenes do not seem to[5]. Other hypothesized advantages of organosulfur copolymers as Li-S cathodes include: suppression of the polysulfide shuttling phenomenon through anchoring (through cross-linking) of the sulfur chains with the organic backbone, and improved processability, in a sense that organosulfur copolymers have mechanical properties that may lend them to be printed or electrospun, among other processing methods. The proposed structure of poly(S-*r*-DEB) includes the linkage of divinylbenzene units with sulfur chains of varying length, represented in Fig. 5.2. It should be noted that this figure depicts sulfur to have reacted at both carbons in the ethynyl groups, also under certain conditions this may not be the case. At this point, the poly(S-*r*-DEB) is ready to be incorporated into a half-cell for characterization as a sulfurous cathode material.

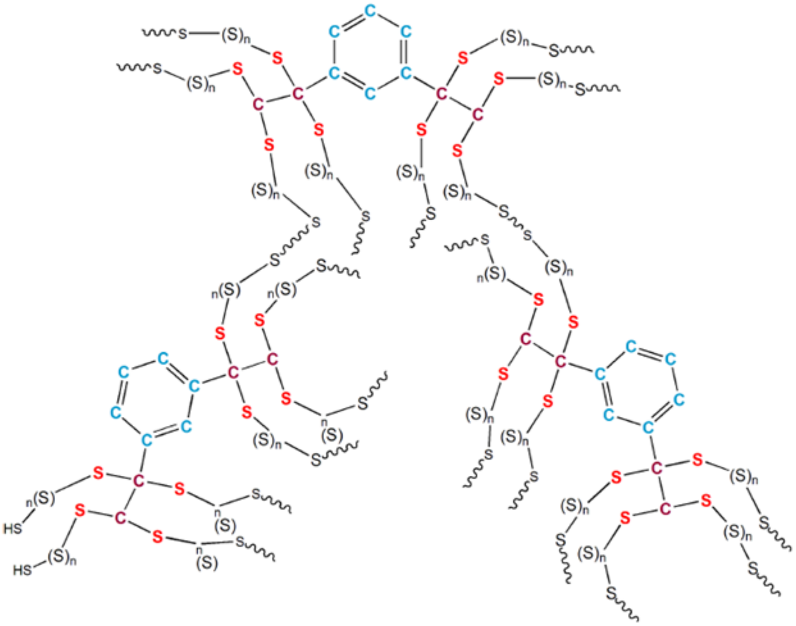

Figure 5.2: Proposed structure of poly(S-r-DEB).

A stable, high sulfur loading, nanostructured Li-S cathode can be synthesized using the recently exploited inverse vulcanization method of S_8 and 1,3-DEB in open atmosphere. The advances of these methods over literature methods include: synthesis at lower temperatures, an annealing step (to reduce unreacted sulfur), and ability to do without inert gas for synthesis. We propose that after printing or electrospinning the copolymer product onto an aluminum current collector, the nanostructured active material could be sputter-coated with a conductive additive (i.e. plasma carbon-coating, for example).

A more traditional electrode fabrication pathway could be: using a mortar and pestle to grind poly(S-*r*-DEB) into a powder. Next, carbon black and binder (polystyrene powder) can be mixed in, and made into a slurry using NMP solvent (n-methyl-2-pyrrolidone) or chloroform. The slurry can then be cast onto an aluminum foil current collector, and eventually used as the cathode in an Li-S battery. The dried electrode, in either case, will be used as the positive electrode in the CR2032 coin cell-type batteries and tested for performance at the beginning laboratory research stage.

5.2 Preliminary Results and Conclusion

Preliminary characterization was carried out on poly(S-*r*-DEB) after synthesis at 130^{o}C, and ~10 wt. % while stirring. Powder X-ray diffraction (XRD) was obtained of poly(S-*r*-DEB) and compared to a sulfur control, seen in Fig. 5.3. There is clearly a shift of peaks, upfield, by ~1^{o}. This is characteristic of crosslinking, as the C-S bonds formed expands the lattice parameters of sulfur as the material cools after the polymerization[6]; we hypothesize that the benzene rings, in particular, have increase the lattice parameter, slightly shifting all of the reflections. In addition, the aligned XRD spectra (inset) helps to identify, clearly, 2 new additional peaks which were generated as a result of the synthesis (θ = 24.1, 24.7), again indicating a new material has been formed. Raman spectroscopy

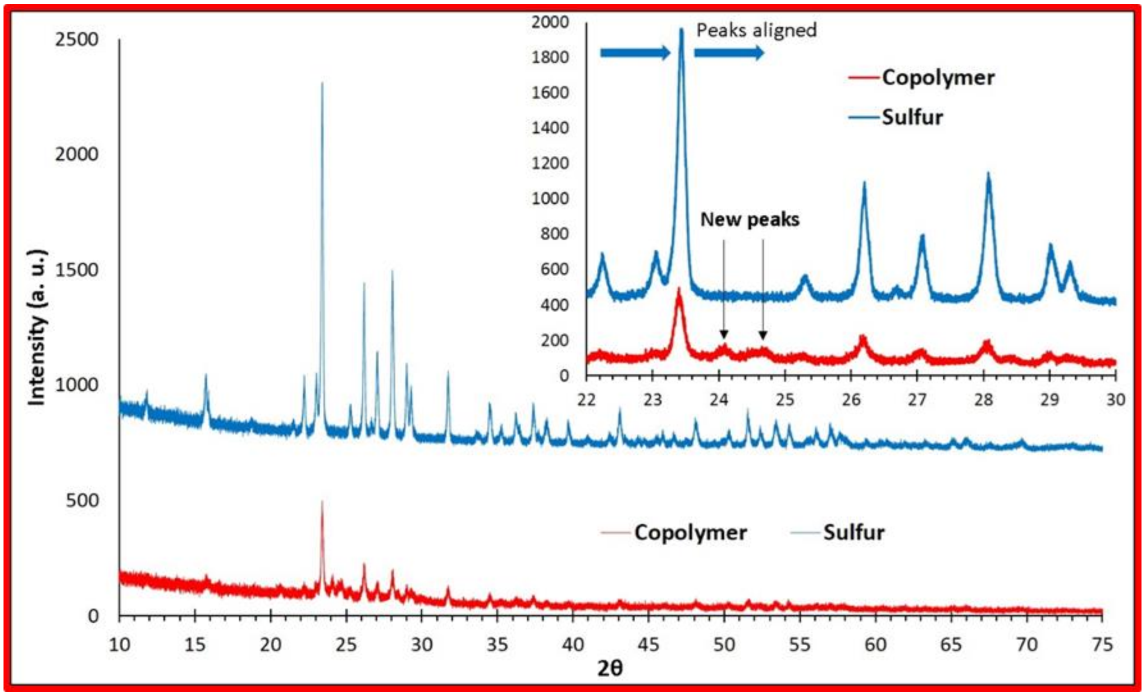

Figure 5.3: XRD spectrum of S-DEB copolymer vs. sulfur control (inset aligns the peaks for corrected comparison).

was also used to study the poly(S-*r*-DEB) vs. a sulfur control. Again, there is a peak shift with the generation of 2 new peaks (184, 195 cm^{-1}), and the disappearance of 1 peak (188 cm^{-1}). The peak at 188 cm^{-1} is a characteristic peak of elemental sulfur at room temperature (corresponding to the fundamental "inactive" B1 vibration of the S_8 ring)[7]. SEM characterization shows the poly(S-*r*-DEB) electrode structure after being cast onto aluminum, and after fracture inducing (seen in Fig. 5.5). The obviously larger particles are poly(S-*r*-DEB) particles, which are contributing to the cracking effect in the electrode. Further electrode optimization needs to take place to ensure less cracking prior to serious battery characterization on poly(S-*r*-DEB) electrodes.

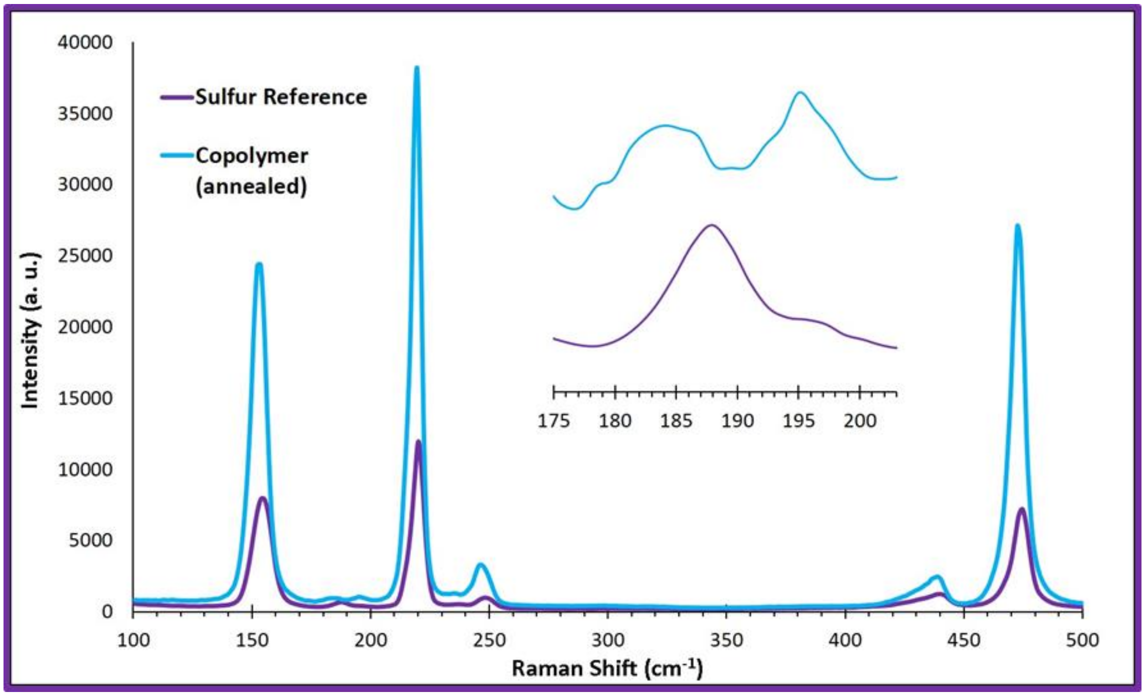

Figure 5.4: Raman spectra of sulfur and S-DEB copolymer vs. sulfur control.

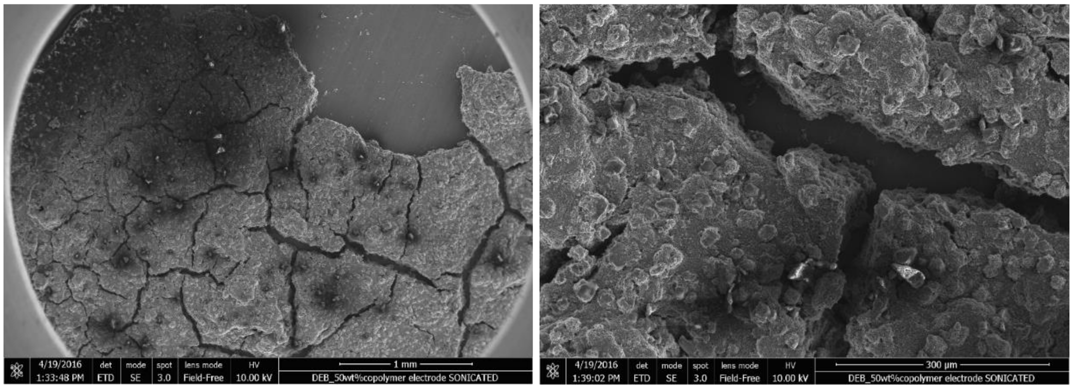

Figure 5.5: SEM of the electrode fabricated using S-DEB as the active material, with low magnification (above) and high magnification (low).

References

1. Chung, W. J. et al. The use of elemental sulfur as an alternative feedstock for polymeric materials. Nat. Chem.**5**, 518-524 (2013).

2. Simmonds, A. G. et al. Inverse Vulcanization of Elemental Sulfur to Prepare Polymeric Electrode Materials for Li-S Batteries. ACS Macro Lett. **3**, 229-232 (2014).

3. Dirlam, P. T. et al. Improving the Charge Conductance of Elemental Sulfur via Tandem Inverse Vulcanization and Electropolymerization. ACS Macro Lett. **4**, 111-114 (2015).

4. Dirlam, P. T. et al. Inverse vulcanization of elemental sulfur with 1,4-diphenylbutadiyne for cathode materials in Li-S batteries. RSC Adv. **5**, 24718 (2015).

5. Griebel, J. J. et al. Kilogram Scale Inverse Vulcanization of Elemental Sulfur to Prepare High Capacity Polymer Electrodes for Li-S Batteries. J. Polym. Sci. A Polym. Chem. **53**, 173-177 (2016).

6. Moon, J., Kalb, P. D., Milian, L. and Northrup, P. A. Characterization of a sustainable sulfur polymer concrete using activated fillers. Cement and Concrete Composites **67**, 20-29 (2016).

7. Ward, A. T. Raman Spectroscopy of Sulfur, Sulfur-Selenium, and Sulfur-Arsenic Mixtures. J. Phys. Chem. **72**, 4133-4139 (1968).